DEVELOPMENT OF A STARCH ASSISTED FACILE METHOD FOR THE PREPARATION OF NANO IRON-MANGANESE BASED BINARY OXIDES

A THESIS SUBMITTED IN PARTIAL FULFILLMENT OF THE REQUREMENT FOR THE DEGREE OF MASTER OF SCIENCE (M. Sc.) IN CHEMISTRY

SUBMITTED BY

ANWARUL AZIM

STUDENT ID: F1014032707

SESSION: OCTOBER 2014

Nanochemistry Research Laboratory

Department of Chemistry

Bangladesh University of Engineering and Technology (BUET)

Dhaka-1000, Bangladesh

September 2016

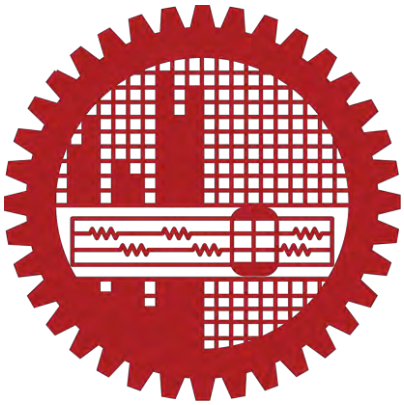

CANDIDATE'S DECLARATION

It is hereby declared that this thesis or any part of it has not been submitted elsewhere for the award of any degree or diploma.

Anwarul Azim

.....

(ANWARUL AZIM)

Signature of the Candidate

Bangladesh University of Engineering and Technology, Dhaka
Department of Chemistry

Certification of Thesis
A thesis on
"DEVELOPMENT OF A STARCH ASSISTED FACILE METHOD FOR THE PREPARATION OF NANO IRON-MANGANESE BASED BINARY OXIDES"

BY
Anwarul Azim

has been accepted as satisfactory in partial fulfillment of the requirements for the degree of Master of Science (M. Sc.) in Chemistry and certify that the student has demonstrated a satisfactory knowledge of the field covered by this thesis in an oral examination held on September 7, 2016.

Board of Examiners

1. Dr. Md. Shakhawat Hossain Firoz
Associate Professor
Department of Chemistry
BUET, Dhaka

Supervisor & Chairman

2. Dr. Md. Rafique Ullah
Professor & Head
Department of Chemistry
BUET, Dhaka

Member (Ex-officio) 07.09.2016

3. Dr. Md. Nazrul Islam
Professor
Department of Chemistry
BUET, Dhaka

07/09/16
Member

4. Dr. Mohammed Abdul Basith
Associate Professor
Department of physics
BUET, Dhaka

Member (External)

Dedicated to

My beloved parents

&

Honorable supervisor

Acknowledgement

At the very beginning, I humbly acknowledge my heartfelt gratitude to the almighty, the most gracious, benevolent and merciful Allah for his infinite mercy bestowed on me in carrying out the research work presented in the dissertation.

It‟s a great pleasure for me to acknowledge my deepest sense of gratitude, sincere appreciation, heartfelt indebtedness and solemn regards to my reverend teacher and supervisor Dr. Md. Shakhawat Hossain Firoz, Associate Professor, Department of Chemistry, Bangladesh University of Engineering and Technology (BUET), for his kind supervision, indispensable guidance, valuable and constructive suggestions, generous help and continuous encouragement during the whole period. It is obvious that his attributive contribution and efforts have greatly shaped me into what I am today. In fact, I am quite lucky to be a part of his ambitious research team.

It‟s my great honor to convey my sincere gratitude to my respected teacher Professor Dr. Md. Rafique Ullah, honorable Head of the Department of Chemistry, BUET for giving me his wonderful support to move through the academic processes during this degree program.

I would like to convey my deepest gratitude to the board of examiners for their valuable corrective suggestion.

I would like to thank Professor Dr. Md. Nazrul Islam, Assistant Professor Dr. Abu Bin Imran, Assistant Professor Dr. Md. Shafiul Azam and Assistant Professor Md. Abu Hasan Howlader Department of Chemistry, BUET, for their valuable suggestions and guidance during the research period. I am thankful to all other respected teachers of the Department of Chemistry for their time to time support. I would also like to thank all of the officers and staffs of the Department of Chemistry, BUET for their continuous help during my study period.

I am highly grateful to Associate professor Dr. Mohammed Abdul Basith (Department of physics, BUET), Dr. Mohammed Nazrul Islam Khan, Principle Scientific Officer and A. K. M. Atique Ullah, Scientific Officer, Bangladesh Atomic Energy Center, Dhaka, for their significant suggestions, intellectual help, solutions of abstruse matters and continuous inspiration throughout my research work.

I am grateful to CASR, BUET for providing financial support for this research work. I am also grateful to the authority of Bangladesh Atomic Energy Commission for providing me the logistic supports for this M. Sc. degree program.

Finally, I would like to express my heartfelt indebtedness and profound gratitude to my beloved father, mother, all of my family members and relatives for their continuous inspiration and immeasurable sacrifices throughout the period of my study.

ANWARUL AZIM September 2016

Abstract

In the present study, attempt was taken to develop a facile method for the preparation of binary oxide of Fe–Mn in nanodimension using starch and metal salts for the removal of total arsenic of ground water. Arsenic contaminated groundwater is a serious health issue worldwide especially in Bangladesh. Arsenic is naturally present in groundwater in the forms of arsenite (AsO_3^{3-}) and arsenate (AsO_4^{3-}). As (III) is more toxic and more difficult to remove from groundwater than As (V). Oxidation of As(III) to As(V) always benefits to attain higher removal of arsenic from arsenic contaminant water in sorption process. However, this leads to a complicated operation and is not cost-effective. To overcome these disadvantages, a novel Fe–Mn binary oxide material which combined the oxidation property of manganese dioxide (oxidation of As(III) to As(V))and the high sorption features of iron oxides to As(V), were developed from low cost materials *viz.* starch and metal salt via a gel formation route.

The samples of different Fe:Mn ratio were prepared using $Fe(NO_3)_3$, $KMnO_4$ and starch at 80^oC in aqueous media. The mixed oxide-starch gel was heat treated at 650^oC in air. The phase identification, chemical composition, crystal structure, crystallinity and surface morphology were analyzed using powder X-ray Diffraction (XRD), Energy Dispersive X-ray (EDX), Fourier Transform Infra-Red (FTIR) and Field Emission Scanning Electron Microscopy (FESEM) techniques. The FESEM shows that the dimensions of the synthesized particles of the mixed oxide matrix were around 5-50 nm which was agreement with XRD data. The mixing ratio of $Fe(NO_3)_3$ and $KMnO_4$ had profound effect on the size and shape of the nanoparticles. When $Fe(NO_3)_3$ treated with starch in absence of $KMnO_4$ the prepared iron oxide nanoparticles was $\alpha-Fe_2O_3$ (Lattice structure: Rhombohedral) but in the presence of $KMnO_4$ it form Fe_3O_4 (Lattice structure : Face-centered cubic). The surface morphology of the particles also vary with the mixing ratio of Fe:Mn. Small spherical (around 5 nm) Fe–Mn binary oxide nanoparticles were obtained, when the mixing ratio was 1:2.55 (Fe:Mn). Also, the material was arranged in high order looks as like

as a wall made of rock on the surface of Fe–Mn binary oxide found at mixing ratio 1:0.64 (Fe:Mn).

The simultaneous oxidation and sorption capacity of the sorbents were carried out at neutral media (pH 7.0). Batch experimental results shows that the sorbents could oxidize As(III) to As(V) and was effective for the simultaneous removal of both As(V) and As(III). The maximal sorption capacity was 79.675 mg/g for solution containing equimolar As(III) and As(V) species at pH 7.0 which was moderately high. MnO_2 nanoparticles has high oxidation ability to As(III) but cannot be absorbed As(III) and As(V) from arsenic contaminant water. Thus in As sorption process MnO_2 works as oxidizing agent. The Fe–Mn binary oxides could be a promising sorbent for both As(V) and As(III) removal because of its excellent performance, facile and low-cost synthesis process.

Contents

List of Tables

List of Figures

Chapter 1
Introduction

1.1 Introduction

Transition metal oxide nanoparticles show interesting size-dependent properties due to a wide diversity in their crystal structures and the oxidation states of the metals. The oxides of transition metals like Zn, Cu, Ni, Ti, Sn, Fe, Mn, Co and W etc., have received an excellent properties in different areas like material science, chemistry and physics, which in turn have produced current exploitation and vast applications in magnetic devices, water purification process, biomedicals, electro-catalysis, photo-catalysis, anticorrosive coatings and powder metallurgy [1-3]. The properties of the materials depend not only on the oxidation state or crystal structure, but are also influenced by finite size effects. For example, such nanoparticles show enhanced catalytic properties compared to bulk material [4], sorption properties and size-dependent magnetic effects like super-paramagnetism [5–7]. Therefore, they show a high potential for applications in a variety of fields like catalysis [2] and sorption process for heavy metals removals from water [8]. The tunable particle size covering uniform distribution can be obtained by utilizing chemical methods such as sol-gel, micro-emulsion and precipitation from metal-organic complex [7]. The mentioned methods are expensive and need multistep purification. The alternative method of template formation using starch via a gel formation route might promising in formation of single and binary oxides especially, effective sorbent for heavy metal of water like Iron oxide, Manganese oxide and their binary composite in nano-dimension. This green process requires starch- a eco-friendly, abundant, low-cost, non-toxic materials - in aqueous solution along with the metal salts in controlled heating condition for the formation of a metal oxide-starch gel.

Arsenic is omnipresent in nature and well-known for its high toxicity and carcinogenicity. It is introduced into the water and ground water through a combination of natural processes such as weathering reactions, dissolution of minerals and biological activity as well as through anthropogenic activities such as mining, agriculture and manufacturing [9]. Elevated arsenic levels in groundwater have been reported in many countries and regions throughout the world, which poses a

significant threat to human health [10]. Arsenic contamination of drinking water leads to chronic poisoning and affects more than 140 million people across 70 countries worldwide and is considered as the most challenging water pollution on a global scale [11]. Arsenic in groundwater is a widespread contaminant in South East Asia affecting the quality of drinking water in Bangladesh [11], India [12] and Cambodia [13]; it is also present to a lesser degree in the USA [14] and in parts of the UK. In Bangladesh, the groundwater has high levels of arsenic in shallow tube wells; over 45 % of these wells exceed the World Health Organization (WHO) recommendation of 10 μg/L and 27 % exceed the 50 μg/L limit set by the Bangladeshi authorities [11]. The high concentrations of arsenic in the main drinking water source for over 50 million people in Bangladesh has been posing a serious threat that signified the largest mass poisoning of a population in history [11,15]. Detrimental effects arising from chronic exposure to low doses of arsenic have been demonstrated in epidemiological studies, and include an array of health problems such as skin lesions, skin cancer, bladder cancer, kidney cancer and lung cancer, neurological disorders and cardiovascular disease [11]. Furthermore, such health problems generate many issues both at an individual level (e.g. social stigma, loss of income, lowered educational attendance) and at a national level (e.g. reduced labour supply, decreased productivity, rising healthcare costs) [16–17]. As a result it is required to develop an economical, effective and reliable treatment technique for arsenic removal from ground water for poverty alleviation and sustainable growth.

Arsenic is primarily present in two predominant species in groundwater, arsenite, As(III) and arsenate, As(V) [18]. Arsenic is naturally present in groundwater in the forms of arsenite (AsO_3^{3-}) and arsenate (AsO_4^{3-}). These anions are similar to phosphite (HPO_3^{2-}) and phosphate (PO_4^{3-}) ions and it is main reason of their toxicity, arsenite and arsenate block ATP→ADP conversions by permanently replacing phosphate groups [19]. There are many treatment techniques e.g. coagulation/precipitation [20], ion-exchange [21], sorption [22–23] and membrane processes [21, 24] have been developed and employed for arsenic removal. Due to its

simplicity, high efficiency and cost-effectiveness, sorption processes are regarded as the most promising methods and largely employed for arsenic removal from water and wastewater [22, 25].

Many sorbents such as natural and synthetic materials have been extensively investigated to remove arsenic from water [26]. In the present days metal oxide sorbents like iron [27–28], aluminum [29–30], Titanium [31–32], manganese [33–34], and zirconium [35–36] have been used. However, iron-oxides mostly studied because of their high affinity to arsenic species, low cost and environmental friendliness [37–39]. Incorporation of other metal oxides into the iron oxide matrix has shown favorable changes in the physical properties such as surface area, surface charge, porosity and crystallinity [23, 40]. Bimetallic composite or mixed oxide sorbents like Fe–Ce [41], Fe–Ti [40] and Fe–Zr [42] have drawn considerable interests.

The adsorption of As(III) by iron oxides is less significant than that of As(V) [43]. Therefore, oxidation of As(III) to As(V) is proposed as an effective option to increase the adsorption capacity and to decrease the environmental risk [23]. Manning *et. al.* [44] studied As(III) oxidation and As(V) adsorption reactions on synthetic birnessite. Moreover, a Fe–Mn binary oxide preparation was synthesized by Zhang *et. al.* 2007 [23] and Kong *et.al.* [45]. The adsorption mechanism has also been investigated by a number of researchers using EXAFS and IR spectroscopic techniques and they show that arsenic forms bi-nuclear bidentate as well as monodentae complexes on the iron oxide surface [46–48]. Manganese oxides have been extensively investigated as oxidizing agents for arsenite [49–52], and some researchers observed the overall oxidation reaction (shown in reaction 1). Recent works by Moore *et. al.* [53] and Nesbitt *et.al.* [51] demonstrated that the oxidation of As(III) by the synthetic birnessite surface proceeds by a two-step pathway (given in reactions 2 and 3), involving the reduction of Mn(IV) to Mn(III) and then Mn(III) to Mn(II).

$$MnO_2 + H_3AsO_3 + 2H^+ = Mn^{2+} + H_3AsO_4 + H_2O \quad (1)$$

$$2MnO_2 + H_3AsO_3 = 2MnOOH^* + H_3AsO_4 \quad (2)$$

$$2MnOOH^* + H_3AsO_3 + 4H^+ = 2Mn^{2+} + H_3AsO_4 + 3H_2O \quad (3)$$

where MnOOH* represents Mn(III) intermediate reaction product.

Recently, a few reports have been published for the preparation of Fe–Mn–oxides nanoparticles through chemical co-precipitation method. Zhang *et al.* [23] synthesized Fe–Mn–oxides nanoparticles through the co-precipitation reaction between $KMnO_4$ and $FeSO_4.7H_2O$ in presence of NaOH which requires a post treatment at 105 °C [23]. The so prepared nano Fe–Mn–oxides were not in uniform size. Moreover the authors reported that for the preparation of Fe–Mn oxide nanoparticles needs higher reaction temperatures. Parsons *et. al.* [54] also synthesized Fe_3O_4, Mn_3O_4 and $MnFe_2O_4$ nanoparticles by the reaction of $FeCl_2$ and $MnSO_4$ in an aqueous solution of NaOH at 125 °C for 4 hours. Hence, it seems to be apparent that the co-precipitation method requires high reaction temperature that leads to inconsistency in product quality. Furthermore, co-precipitation method requires highly pure NaOH and the prepared Fe–Mn oxides are large in particles, having long adsorption equilibrium time and limited adsorption capacity, not cost effective moreover all these chemicals are highly reactive and pose potential environmental and biological risks. Therefore, the conventional co-precipitation method has been found to be expensive, time consuming and polluting. As a consequence it is emergent to establish a low temperature process to synthesize size and shape controlled Fe–Mn–oxides precursors without using expensive equipment and hazardous chemicals.

Without using alkoxides, metal oxides can be synthesized by using gel formation route. Starch is a potential candidate for Fe-Mn nanoparticles synthesis since it is eco-friendly attributes, namely very abundant, low-cost, non-toxic and renewable raw material. Starch is a polysaccharide that contains amylose and amylopectin which essentially consists of polymeric chains made-up from glucose units. This polymeric structure of starch provides a helical-shaped carbonaceous matrix, carrying multiple polyol groups, which may create a protective and functionalized surrounding shield

for nanoparticles. As a result the nanoparticels remain in uniform size they cannot aggregate into larger size.

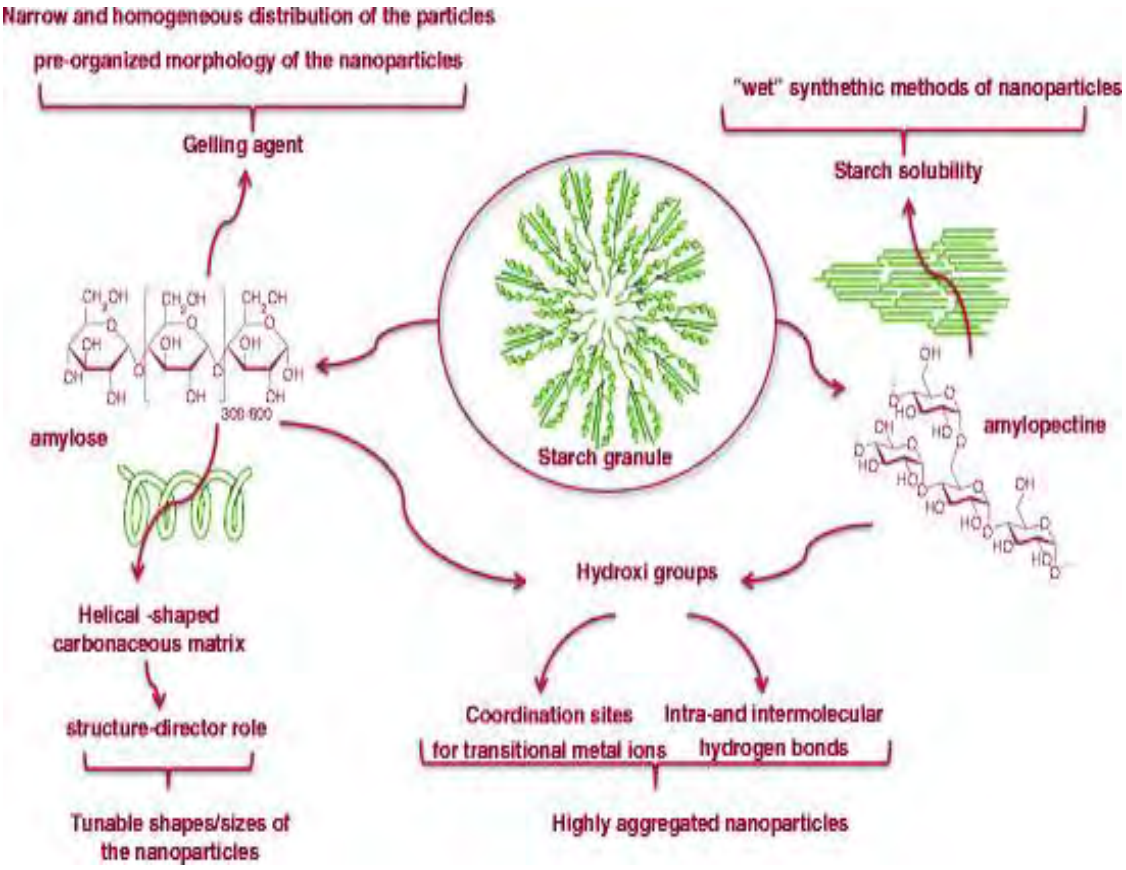

Fig.1.1: The multiple roles of starch in the synthesis of nanomaterials.

In the present study, attempt was taken to synthesize Fe–Mn oxides nanoparticles via a facile gel formation route using starch. Then optimize reaction condition for the starch assisted gel formation route for the preparation of single oxide of iron and Manganese as well as their binary composites in nanodimension.

Thus, in this investigation, a starch assisted facile method was developed to synthesize Fe–Mn binary oxides elevated temperature. The main objectives of the present work were to

(i) develop a low cost facile gel formation method for the preparation of Iron oxide, Manganese oxide and Iron-Manganese binary oxides in nanodimension.

(ii) characterize the structure and surface of the prepared materials.

(iii) study the oxidation of As (III) to As (IV) and thus removal of total arsenic from the ground water.

References

1) Saiyed, Z. M., Telang, S. D., and Ramchand, C. N., "Application of magnetic techniques in the field of drug discovery and biomedicine," *Biomagn Res. Technol.,* Vol. 1, (2003).

2) Tadi, M., Markovi, D., Spasojevi, V., Kusigerski, V., Remskar, M., Pirnat, J., and Jaglicic, Z., "Synthesis and magnetic properties of concentrated α-Fe_2O_3 nanoparticles in a silica matrix," *J. Alloys Compd.,* Vol. 441, pp. 291–296, (2007).

3) Zaitsev, Filimonov, Presnyakov and Gambino; "Physical and Chemical Properties of Magnetite and Magnetite-Polymer Nanoparticles and Their Colloidal Dispersions," *J Colloid Interface Sci.,* Vol. 212, pp. 49-57, (1999).

4) Li, L., Hu, J., Yang, W., and Alivisatos, A. P., "Band gap variation of size-and shape-controlled colloidal CdSe quantum rods," *Nano Letters,* Vol. 1 (2001), 349-351

5) Wu, W., He, Q., and Jiang, C., "Magnetic Iron Oxide Nanoparticles: Synthesis and Surface Functionalization Strategies," *Nanoscale Res. Lett.,* Vol. 3 397–415, (2008).

6) Shao, H., Yoon, T., Liong, M., Weissleder, R., and Leecorresponding, H., "Magnetic nanoparticles for biomedical NMR-based diagnostics," *Beilstein J Nanotechnol,* Vol. 1, pp. 142–154, (2010).

7) Stevens, P. D., Fan, J., Gardimalla, H. M. R., Yen, M., and Gao, Y., "Superparamagnetic Nanoparticle-Supported Catalysis of Suzuki Cross Coupling Reactions," *Org. Lett.,* Vol. 7, pp. 2085-2088, (2005).

8) Praveen, K., Tandon, Shukla, R. C., and Singh, S. B., "Removal of Arsenic(III) from Water with Clay-Supported Zerovalent Iron Nanoparticles

Synthesized with the Help of Tea Liquor," *Ind. Eng. Chem. Res.,* Vol. 52, pp. 10052–10058, (2013).

9) Cullen, W.R., Reimer, K.J., "Arsenic speciation in the environment," *Chem Reviews.,* Vol. 89, pp. 713-764, (1989).

10) Smedley, P.L., Kinniburgh, D.G., "A review of the source, behavior and distribution of arsenic in natural waters," *Appl. Geochem.,* Vol. 17, pp. 517–568, (2002).

11) Smith, A.H., Lingas, E.O., and Rahman, M., "Contamination of Drinking-Water by Arsenic in Bangladesh: A Public Health Emergency," *Bull World Health Organ.,* Vol. 78, pp. 1093-1103, (2000).

12) Hossain, M.A., Sengupta, M.K., Ahamed, S., Rahman, M. M., Mondal, D., Das, B., Nayak, B., Roy, B. K., Mukherjee, A., and Chakraborti, D., "Poor Ineffectiveness Reliability of Arsenic Removal Plants in West Bengal, India," *Environ. Sci. Technol.,* Vol. 39, pp. 4300–4306, (2005).

13) Rowland, H. A. L., Gault, A.G., Lythgoe, P.R., and Polya, D.A.; "Geochemistry of aquifer sediments and arsenic-rich groundwaters in Cambodia," *Appl. Geochem.,* Vol. 23, pp. 3029-3046, (2008).

14) Root, T. L., Gotkowitz, M. B., Bahr, J. M., and Attig, J. W., "Arsenic Geochemistry and Hydrostratigraphy in Midwestern US Glacial Deposits," *Groundwater,* Vol. 48, 903–912, (2010).

15) Argos, M., Kalra, T., Rathouz, P.J., Chen, Y., Pierce, B., Parvez, F., Islam, T., Ahmed, A., Rakibuz-Zaman, M., Hasan, R., Sarwar, G., Slavkovich, V., Geen, A., Graziano, J., and Ahsan, M. H., "Arsenic Exposure from Drinking Water, and All Cause and Chronic Disease Mortalities in Bangladesh (HEALS): A Prospective Cohor Study," *Lancet.,* Vol. 376, pp. 252-258, (2010).

16) Carson, R. T., Koundouri, P., and Nauges, C. L., "Arsenic Mitigation in Bangladesh: A Household Labor Market Approach," *AJAE.,* Vol. 93, pp. 407–414, (2011).

17) Rahman, "Towards an Arsenic Safe Environment in Bangladesh." *BCAS*, 2010.

18) Smedley, P.L., and Kinniburgh, D.G., "A review of the source, behavior and distribution of arsenic in natural waters," *Appl. Geochem.,* Vol. 17, pp. 517–568, (2002).

19) Jain, C. K., & Ali, "Arsenic: Occurrence, toxicity and speciation techniques," *Water Res.,* Vol. 34, pp. 4304–4312, (2000).

20) Scott, K. N., Green, J. F., Do, H. D., and Mclean, S. J., "Arsenic removal by coagulation," *J Am Water Works Assoc.,* Vol. 87, pp. 114–126, (1995).

21) Kartinen, E. O., Martin, C. J., "An overview of arsenic removal processes." *Desalination,* 103 (1995) 79–88.

22) Jang, M., Min, S. H., Kim, T. H., and Park, J. K., "Removal of arsenite and arsenate using hydrous ferric oxide incorporated into naturally occurring porous diatomite," *Environ. Sci. Technol.,* Vol. 40, pp.1636–1643, (2006).

23) Zhang, G. S., Qu, J. H., Liu, H. J., Liu, R. P., and Wu, R. C., "Preparation and evaluation of a novel Fe–Mn binary oxide adsorbent for effective arsenite removal," *Water Res.,* Vol. 41a, pp. 1921–1928, (2007).

24) Waypa, J. J., Elimelech, M., and Hering, J.G., "Arsenic removal by RO and NF membranes," *J Am Water Works Assoc.,* Vol. 89, pp. 102–116, (1997).

25) Sharma, V. K., and Sohn, M., "Aquatic arsenic: toxicity, speciation, transformations, and remediation," *Environ. International.,* Vol. 35, pp. 743–759, (2009).

26) Mohan, D., and Pittman, C. U., "Arsenic removal from water/ wastewater using adsorbentse–A critical review," *J. of Hazardous Materials,* Vol. 142, pp. 1–53, (2007).

27) Raven, K. P., Jain, A., and Loeppert, R. H., "Arsenite and arsenate adsorption on ferrihydrite: kinetics, equilibrium, and adsorption envelopes," *Environ. Sci. Technol.* Vol. 32, pp. 344–349, (1998).

28) Dixit, S., and Hering, J. G., "Comparison of arsenic(V) and arsenic(III) sorption onto iron oxide minerals: implications for arsenic mobility." *Environ. Sci. Technol.* Vol. 37, pp. 4182–4189, (2003).

29) Lin, T. F., and Wu, J. K., "Adsorption of arsenite and arsenate with activated alumina grains: equilibrium and kinetics," *Water Res.* Vol. 35, pp. 2049–2057, (2001).

30) Patra, A. K., Dutta, A., and Bhaumik, A. "Self-assembled mesoporous γ-Al_2O_3 spherical nanoparticles and their efficiency for the removal of arsenic from water," *J. of Hazardous Materials.,* Vol. 201–202, pp. 170–177, (2012).

31) Pena, M. F., Korfiatis, G. P., Patel, M., Lippincott, L., and Meng, X. G., "Adsorption of As(V) and As(III) by nanocrystalline titanium dioxide," *Water Res.* Vol. 39, pp. 2327–2337, (2005).

32) Jegadeesan, G., Al-Abed, S. R., Sundaram, V., Choi, H., Scheckel, K. G., and Dionysiou, D.D., "Arsenic sorption on TiO_2 nanoparticles: size and crystallinity effects," *Water Res.,* Vol. 44, pp. 965–973, (2010).

33) Lenoble, V., Laclautre, C., Serpaud, B., Deluchat, V., and Bollinger, J. C., "As(V) retention and As(III) simultaneous oxidation and removal on a MnO_2-loaded polystyrene resin," *Sci. Total Environ.,* Vol. 326, pp. 197–207, (2004).

34) Lafferty, B. J., Ginder-Vogel, M., and Sparks, D. L., "Arsenite oxidation by a poorly crystalline manganese oxide. Stirred–flow experiments," *Environ. Sci. Technol.,* Vol. 44, pp. 8460–8466, (2010).

35) Hristovski, K. D., Westerhoff, P. K., Crittenden, J. D., and Olson, L. W., "Arsenate removal by nanostructured ZrO_2 spheres," *Environ. Sci. Technol.,* Vol. 42, pp. 3786–3790, (2008).

36) Hang, C., Li, Q., Gao, S., and Shang, J. K., "As(III) and As(V) adsorption by hydrous zirconium oxide nanoparticles synthesized by a hydrothermal process followed with heat treatment," *Ind. Eng. Chem. Res.,* Vol. 51, pp. 353–361, (2012).

37) Chang, Q. G., Lin, W., and Ying, W. C., "Impacts of Amount of Impregnated Iron in Granular Activated Carbon on Arsenate Adsorption Capacities and Kinetics," *Water Environ. Res.,* Vol. 84, pp. 514–520, (2012).

38) Jovanovic, B. M., Vukasinovic-Pesic, V. L., and Rajakovic, L. V., "Enhanced Arsenic Sorption by Hydrated Iron(III) Oxide-Coated Materials Mechanism and Performances," *Water Environ. Res.,* Vol. 83, pp. 498–506, (2011).

39) Kanel, S. R., Manning, B., Charlet, L., and Choi, H., "Removal of Arsenic(III) from Groundwater by Nanoscale Zero-Valent Iron," *Environ. Sci. Technol.,* Vol. 39, pp. 1291–1298, (2005).

40) Gupta, K., and Ghosh, U. C., "Arsenic removal using hydrous nanostructure iron(III) etitanium(IV) binary mixed oxide from aqueous solution," *J. Hazard. Mater.,* Vol. 161, pp. 884–892, (2009).

41) Zhang, Y., Yang, M., Dou, X. M., He, H., and Wang, D. S., "Arsenate adsorption on an FeCe bimetal oxide adsorbent: role of surface properties," *Environ. Sci. Technol.,* Vol. 39, pp. 7246–7253, (2005).

42) Ren, Z. M., Zhang, G. S., and Chen J. P., "Adsorptive removal of arsenic from water by an ironezirconium binary oxide adsorbent," *J. Colloid Interface Sci.,* Vol. 358, pp. 230–237, (2011).

43) Simeonidis, K., Gkinis, T., Tresintsi, S., Martinez-Boubeta, C., Vourlias, G., Tsiaoussis, I., Stavropoulos, G., Mitrakas, M., and Angelakeris, M., "Magnetic Separation of Hematite-Coated Fe_3O_4 Particles Used as Arsenic Adsorbents," *Chem. Eng. J.,* Vol. 168, pp. 1008–1015, (2011).

44) Manning, B. A., Fendorf, S. E., Bostick, B., Suarez, D. L., "Arsenic(III) Oxidation and Arsenic(V) Adsorption Reactions on Synthetic Birnessite," *Environ. Sci. Technol.,* Vol. 36, pp. 976–981, (2002).

45) Kong, S., Wang, Y., Zhan, H., Yuan, S., Yu, M., and Liu, M., "Adsorption/Oxidation of Arsenic in Groundwater by Nanoscale Fe–Mn Binary Oxides Loaded on Zeolite," *Water Environ. Res.,* Vol. 86, pp. 147–55, (2014).

46) Waychunas, G. A., Rea, B. A., Fuller, C. C., and Davis, J. A., "Surface chemistry of ferrihydrite EXAFS studies of the geometry of coprecipitated and adsorbed arsenate," *Geochimica et Cosmochimica Acta.,* Vol. 57, pp. 2251–2269, (1993).

47) Sun, X. H., and Doner, "An investigation of arsenite and arsenite bonding structures on goethite by FTIR," *Soil Sci.* Vol. 161, pp. 865–872, (1996).

48) Goldberg, S., and Johnston, C. T., "Mechanisms of Arsenic Adsorption on Amorphous Oxides Evaluated Using Macroscopic Measurements, Vibrational Spectroscopy, and Surface Complexation Modeling," *J. Colloid Interface Sci.* Vol. 234, pp. 204–216, (2001).

49) Oscarson, D. W., Huang, P. M., Defosse, C., and Herbillon, A., "Oxidative power of Mn(IV) and Fe(III) oxides with respect to As(III) in terrestrial and aquatic environments," *Nature.,* Vol. 291, pp. 50–51, (1981).

50) Scott, M. J., and Morgan, J. J., " Reactions at oxide surfaces. Oxidation of As(III) by synthetic birnessite," *Environ. Sci. Technol.,* Vol. 29, pp. 1898–1905, (1995).

51) Nesbitt, H. W., Canning, G. W., and Bancroft, G. M., "XPS study of reductive dissolution of 7Å-birnessite by H_3AsO_3 with constraints on reaction mechanism. Geochim," *Cosmochim Acta.,* Vol. 62, pp. 2097–2110, (1998).

52) Manning, B. A., Fendorf, S. F., Bostick, B., and Suarez, D. L., "Arsenic(III) oxidation and arsenic(V) adsorption reactions on synthetic birnessite," *Environ. Sci. Technol.* Vol. 36, pp. 976–981, (2002).

53) Moore, J. N., Walker, J. R., and Hayes, T. H., "Reaction scheme for the oxidation of As(III) to As(V) by birnessite," *Clays Clay Miner.,* Vol. 38, pp. 549–555, (1990).

54) Parsons, J. G., Lopez, M. L., Peralta-Videa, J. R., Gardea-Torresdey, J.L., Determination of arsenic(III) and arsenic(V) binding to microwave assisted hydrothermal synthetically prepared Fe_3O_4, Mn_3O_4, and $MnFe_2O_4$ nanoadsorbents," *Microchem. J.,* Vol. 91, pp. 100–106, (2009).

Chapter 2
Background

2.1.1 Oxides of iron

Iron (Fe) is a metal in the series. It is by mass the most common element on Earth, forming much of Earth's outer and inner core. It is the fourth most common element in the Earth's crust. Like other group 8 elements, iron exists in a wide range of oxidation states, −2 to +6, although +2 and +3 are the most common. Elemental iron occurs in meteoroids and other low oxygen environments, but is reactive to oxygen and water. The most available oxides of iron are FeO, Fe_3O_4, Fe_4O_5, Fe_5O_6, α-Fe_2O_3, β-Fe_2O_3, γ-Fe_2O_3 & ε-Fe_2O_3. The structural properties of some these oxides are listed in Table 2.2

Table 2.1: Structural properties of different oxides of Iron.

Oxide	**FeO**	**Fe_3O_4**	**Fe_4O_5**	**Fe_2O_3**
Mineral Name	wüstite	Magnetite		Hematite
Oxidation Number	+2	+2,+3	+2,+3	+3
Crystal Structure	Cubic	Face-centered cubic	Octahedral	α-Fe_2O_3 = Rhombohedral γ-Fe_2O_3 = Cubic β-Fe_2O_3 = Cubic body centered
Lattice Parameter	a = 4.296 A˚	a = 11.888 A˚ b = 11.847 A˚ c = 16.773 A˚	a = 2.873 A˚ b = 9.694 A˚ c = 12.411 A˚	α-Fe_2O_3 a = 5.035 A˚ c = 13.750 A˚

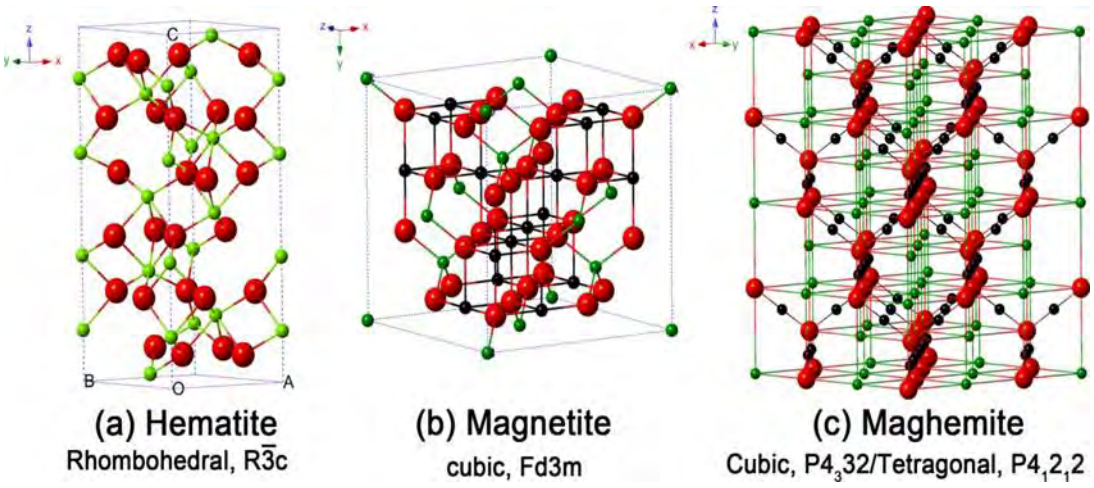

Fig.2.1: Crystal structure of the hematite, magnetite and maghemite (the black ball is Fe^{2+}, the green ball is Fe^{3+} and the red ball is O^{2-}).

2.1.2 Oxides of manganese

Manganese (Mn) is the 10th most abundant element in the earth's crust and second only to iron as the most common heavy metal; on average crustal rocks contain about 0.1% Mn [35]. It occurs in natural systems mainly in three different oxidation states: +2, +3, and +4, giving rise to a range of multivalent phases. The most available oxides of manganese are MnO, Mn_3O_4, Mn_2O_3, MnO_2 and Mn_5O_8. The structural properties of these oxides are listed in Table 2.2

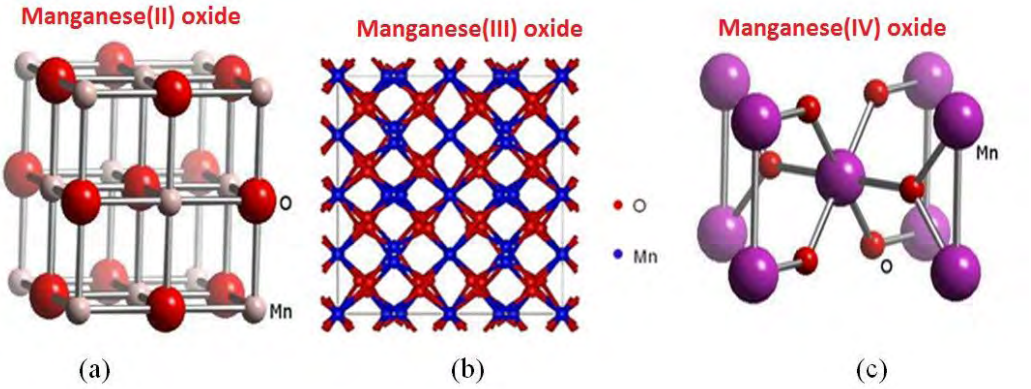

Fig. 2.2: Crystal structures of (a) Mn(II), (b) Mn(III) and (c) Mn(IV) oxides.

Table 2.2: Structural properties of different oxides of Mn

Oxide	**MnO**	**Mn_3O_4**	**Mn_5O_8**	**Mn_2O_3**	**MnO_2**
Mineral Name	Manganosite	Hausmannite	n/a	Bixbyte	Pyrolusite
Oxidation Number	+2	+2, +3	+2, +4	+3	+4
Crystal Structure	Cubic	Tetragonal	Monoclinic	Cubic	Tetragonal
Lattice Parameter	a = 4.446	a = 5.7621 c = 9.4696	a = 10. 392 b = 5.730 c = 4.866 β = 109.62	a = 9.409	a = 4.3999 c = 2.8740

2.2 Arsenic contamination

Arsenic contamination of groundwater is a form of groundwater pollution which is often due to naturally occurring high concentrations of arsenic in deeper levels of groundwater. It is a high-profile problem due to the use of deep tube wells for water supply in the Ganges Delta, causing serious arsenic poisoning to large numbers of people. A study found that over 140 million people in more than 70 countries are probably affected by arsenic poisoning of drinking water[1]. Arsenic contamination of ground water is found in many countries throughout the world, including Bangladesh

Arsenic occurs in two major forms inorganic and the organic. The inorganic arsenic is more toxic than the organic form and is predominantly seen in drinking water, whereas organic form is seen in sea foods. Inorganic arsenic are the components of geological formation and extracted into ground water, the contamination can also be

due to mining, human activities and natural well waters with high concentrations of arsenic. These contaminations extort into drinking water and make it more toxic than organic arsenic. The inorganic forms of arsenic are arsenate, As (V) and arsenite As (III). Arsenite is the reduced inorganic species and is more toxic than the oxidized form arsenate

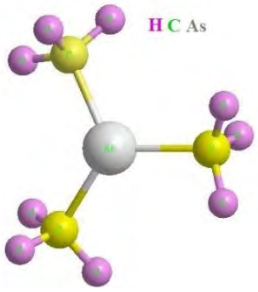

Fig 2.3: Trimethylarsine.

2.2.1 Health hazards

The main source of arsenic contamination for humans is by drinking water. Arsenic contamination in ground water may be from mining activities and other anthropogenic sources, but is often from non-anthropogenic sources such as bed-rock aquifers and minerals. Inorganic and Organic forms of arsenic are responsible for carcinogenic and non-carcinogenic effects. The carcinogenic effects are associated with breast, colon, stomach, head and neck leukemia and lymphoma. Increased risk of contamination may lead to cancer in skin, liver, lungs and bladder [2]. Non-carcinogenic effects are keratosis, cardiovascular effects, diabetes mellitus and adverse birth outcomes. Arsenate and arsenite stimulate the signal pathway of the nervous system causing different physiological responses that lead to the development of cancer and other destructive diseases. Arsenite blocks the thiol (-SH) containing molecules such as glutathione and lipoic acid. Blocking of glutathione leads to oxidative damage and increase in reactive oxygen species. Lipoic acid which is an important co-factor in

pyruvate dehydrogenase enzyme leads to decrease in production of Acetyl-CoA and ATP. Arsenate is chemically similar to phosphate and enters the cell through phosphate transport protein system. It competes with phosphate in binding and inhibits glyceraldehyde 3-phosphate dehydrogenase and ATP production is also inhibited [3].

2.2.2 Global Scenario of arsenic contamination in groundwater

Over the past two or three decades, occurrence of high concentrations of arsenic in drinking-water has been recognized as a major public-health concern in several parts of the world. There have been a few review works covering the arsenic-contamination scenario around the world [1]. With the discovery of newer sites in the recent past, the arsenic-contamination scenario around the world, especially in Asian countries, has changed considerably. Before 2000, there were five major incidents of arsenic contamination in groundwater in Asian countries: Bangladesh, West Bengal, India, and sites in China. Between 2000 and 2005, arsenic-related groundwater problems have emerged in different Asian countries, including new sites in China, Mongolia, Nepal, Cambodia, Myanmar, Afghanistan, DPR Korea, and Pakistan . There are reports of arsenic contamination from Kurdistan province of Western Iran and Viet Nam where several million people may have a considerable risk of chronic arsenic poisoning. The summary of the current global scenario of arsenic contamination is shown in Fig. 2.4.

Fig. 2.4: Global Scenario of arsenic contamination in groundwater.

2.2.3 Scenario of arsenic contamination in Bangladesh

Bangladesh is located in the Padma-Meghna-Brahmaputra plain. Arsenic contamination in groundwater from the Padma-Meghna plain was first reported in 1995. During 1998, 41 of the 64 districts in Bangladesh were identified as having concentrations of arsenic in groundwater exceeding 50 µg/L. The survey revealed that 43.0% of the water samples exceeded 10 µg/L, and 31.0% exceeded 50 µg/L. It was identified arsenic in hand-tubewell water samples >50 µg/L (permissible limit of arsenic in drinking-water in India and Bangladesh) in 50 of the 64 districts. The populations at risk were 52 and 32 million respectively. Almost 19.8% (n=19,000) of patients screened showed skin lesions, whereas 6.1% of children (n=5,000) have skin lesions. In a study in Bangladesh, 83% of hair samples contained toxic levels of arsenic, and 93% of nail samples and 95% of urine samples showed arsenic above normal levels [4]. The normal level of arsenic in hair ranged from 80 to 250 µg/kg (levels ≥1,000 µg/kg indicate toxicity). In nails, normal levels range from 430 to

1,030 µg/kg [4]. Normal excretion of arsenic in urine ranges from 5 to 40 µg per 1.5 litres per day. Consequently, a considerable proportion of the population could be affected sub-clinically. The area and population of 50 arsenic-affected districts in Bangladesh are 118,849 sq km and 105 million respectively compared to the total area and population of the country–148,393 sq km and 120 million respectively [5]. This does not mean that all the affected people are drinking arsenic-contaminated water and suffering from arsenic-related diseases, but no doubt they are at risk.

Several other study have also shown that the level of concentrations of arsenic in tube wells in Bangladesh exceed both WHO guideline value of 10 µg/L and Bangladesh permissible limit of 50 µg/L, with concentrations ranging from 50 to 3,200 µg/L.

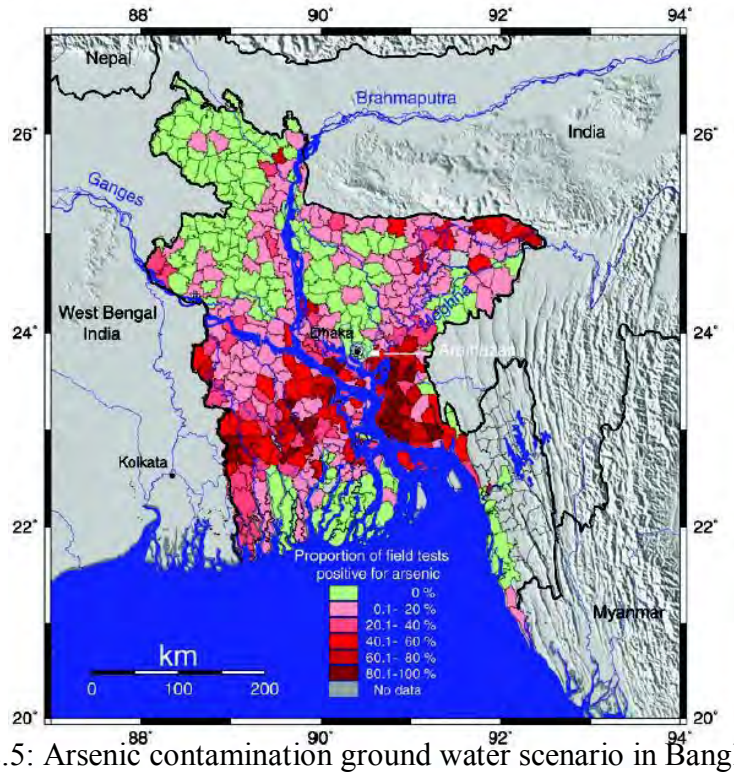

Fig. 2.5: Arsenic contamination ground water scenario in Bangladesh.

2.2.4 Arsenic removal technique from ground water

Regulations may necessitate large-scale treatment systems to remove arsenic from the water supply. The effectiveness of any method depends on the chemical makeup of a

particular water supply. The aqueous chemistry of arsenic is complex, and may affect the removal rate that can be achieved by a particular process.

Some large utilities with multiple water supply wells could shut down those wells with high arsenic concentrations, and produce only from wells or surface water sources that meet the arsenic standard. Other utilities, however, especially small utilities with only a few wells, may have no available water supply that meets the arsenic standard.

Coagulation/filtration

Coagulation/filtration (also known as flocculation) removes arsenic by coprecipitation and adsorption using iron coagulants. Coagulation/filtration using alum is already used by some utilities to remove suspended solids and may be adjusted to remove arsenic. But the problem of this type of filtration system is that it gets clogged very easily, mostly within two to three months. The toxic arsenic sludge are disposed of by concrete stabilization, but there is no guarantee that they won't leach out in future.

Sorption

Iron oxide adsorption filters the water through a granular medium containing ferric oxide. Ferric oxide has a high affinity for adsorbing dissolved metals such as arsenic. The iron oxide medium eventually becomes saturated, and must be replaced. The sludge disposal is a problem here too.

Activated alumina is an adsorbent that effectively removes arsenic. Activated alumina columns connected to shallow tube wells in India and Bangladesh have removed both As(III) and As(V) from groundwater for decades. Long-term column performance has been possible through the efforts of community-elected water committees that collect a local water tax for funding operations and maintenance. It has also been used to remove undesirably high concentrations of fluoride.

Ion exchange

Ion exchange has long been used as a water softening process, although usually on a single-home basis. Traditional anion exchange resins are effective in removing As(V), but not As(III), or arsenic trioxide, which doesn't have a net charge. Effective long-term ion exchange removal of arsenic requires a trained operator to maintain the column.

Both Reverse osmosis and electrodialysis (also called electrodialysis reversal) can remove arsenic with a net ionic charge. (Note that arsenic oxide, As_2O_3, is a common form of arsenic in groundwater that is soluble, but has no net charge.) Some utilities presently use one of these methods to reduce total dissolved solids and therefore improve taste. A problem with both methods is the production of high-salinity waste water, called brine, or concentrate, which then must be disposed of.

2.2.5 Metal–oxides nanoparticles for Arsenic removal from ground water

New approaches are continually being examined to supplement traditional water purification methods. These need to be lower in overall cost, durable and/or more effective than current options for the removal of contaminants from water, either in-situ or in water purification systems. Nanomaterials has high surface area than the normal sorbents. Using this concept now-a-days many water filters are produce

Many sorbents such as iron, aluminum, titanium, manganese and zirconium materials have been extensively investigated to remove arsenic from water. However, iron-oxides mostly studied because of their high affinity to arsenic species, low cost and environmental friendliness.

2.2.5.1 Iron–oxides nanoparticles for Arsenic removal from ground water

Iron exists in a wide range of oxidation states, −2 to +6, although +2 and +3 are the most common. The most available oxides of iron are FeO, Fe_3O_4, Fe_4O_5, Fe_5O_6, α-

Fe_2O_3, β-Fe_2O_3, γ-Fe_2O_3 & ε-Fe_2O_3.Iron oxides, oxyhydroxides and hydroxides, including amorphous hydrous ferric oxide (FeO-OH), goethite (α-FeO-OH) and hematite (α-Fe_2O_3), are promising adsorbents for removing both As(III)) from water.

The iron oxide-coated sand with an easy preparation procedure was investigated for its performance to remove arsenic in water [6, 7]. The adsorption reaction showed a Langmuir-type adsorption isotherm, where the electrostatic interaction was possibly involved in the adsorption. Recently, the iron-oxide coated natural rock was developed with As(III) adsorptive capacity of 1.647mg/g [8], which was in accordance with the data evaluated from the Langmuir isotherm.

Feng et al. synthesized superparamagnetic acid-coated Fe_3O_4 nanoparticles with a high specific surface area through an environmentally friendly hydrothermal route, which exhibited a maximum adsorption capacity of 16.56mg/g for arsenic(V) and 46.06mg/g for arsenic(III) [9].

2.2.5.2 Iron-Manganese binary oxides for arsenic removal

Recently, composite sorbents containing two or more metal oxides have gained considerable attention. Since the composite not only inherits the advantages of parent oxides but shows obviously synergistic effect. A few works had been done in order to synthesize Fe–Mn binary oxides. S.Q. Kong *et al* [10]. Prepared a Fe–Mn binary oxide sorbent, exhibiting a greater enhancement in both As(V) and As(III) removal. G. Zhang *et al.* [11] prepared a novel Fe–Mn binary oxide adsorbent for arsenic removal. Which combined the oxidation property of manganese dioxide and the high adsorption feature to As(V) of iron oxides. However they synthesized Fe–Mn binary oxides using co-precipitation method. But coprecipitation method has disadvantage, it is not ecofriendly since in this method various chemicals are used. So it is It is emergent to establish a process to synthesize nano structured Fe-Mn binary oxides without using toxic and expensive chemicals. One of the possible away may be sol-gel process.

2.3 Synthesis of metal-oxide nanoparticles

There are many bottom up methods of synthesizing iron–oxide nanomaterials, such as hydrothermal, combustion synthesis, gas-phase methods, microwave synthesis and sol-gel processing.

2.3.1 Sol-gel method

The sol-gel process is capable of wetting chemical process to make ceramic and glass materials. This synthesis technique involves the conversion of a system from a colloidal liquid, named sol, into a semi-solid gel phase [12]. The sol-gel technology can be used to prepare ceramic or glass materials in a wide variety of forms: ultra-fine or spherical shaped powders, thin film coatings, ceramic fibres, microporous inorganic membranes, monolithics, or extremely porous aerogels. An overview of the sol-gel process is illustrated in Fig. 2.6.

This technique offers many advantages including the low processing temperature, the ability to control the composition on molecular scale and the porosity to obtain high surface area materials, the homogeneity of the final product up to atomic scale. Moreover, it is possible to synthesize complex composition materials, to form higher purity products through the use of high purity reagents. The sol-gel process allows obtaining high quality films up to micron thickness, difficult to obtain using the physical deposition techniques. Moreover, it is possible to synthesize complex composition materials and to provide coatings over complex geometries [12].

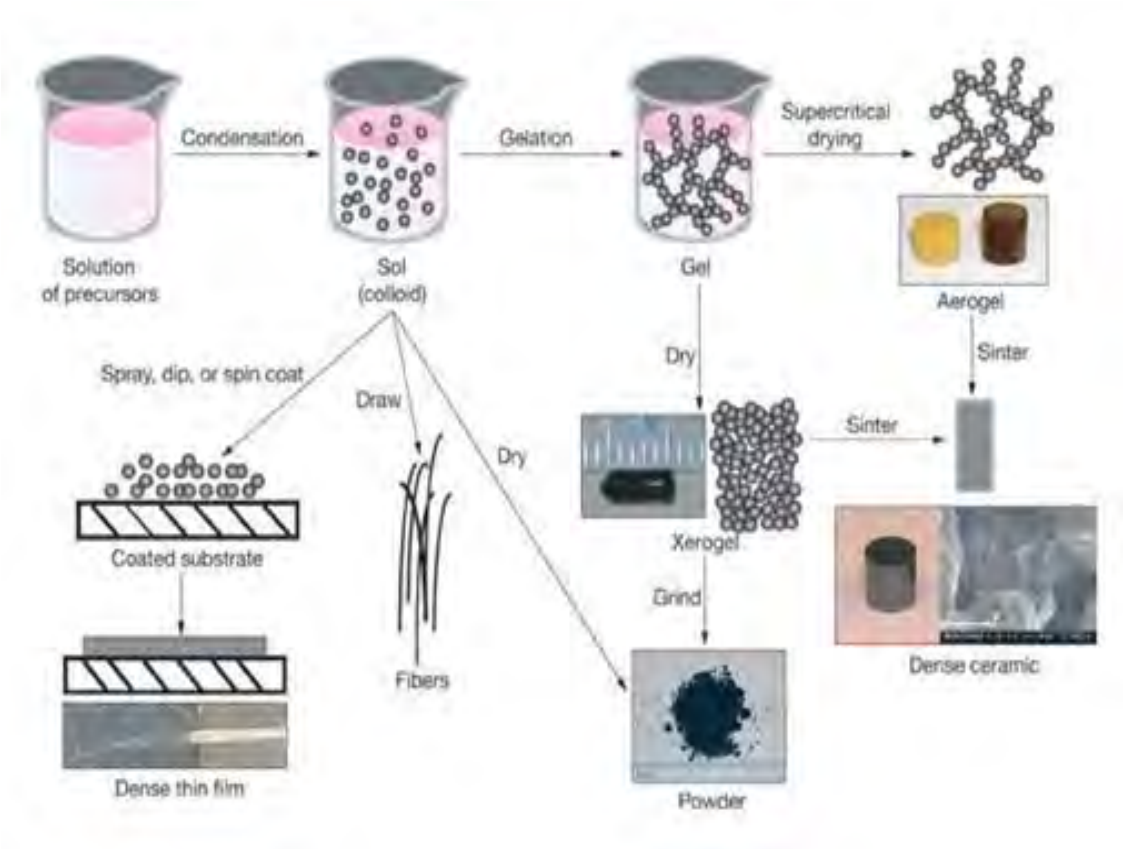

Fig. 2.6: Mechanism of sol-gel process.

The starting materials used in the preparation of the sol are usually inorganic metal salts or metal organic compounds, which by hydrolysis and polycondensation reactions form the sol [12]. Further processing of the sol enables one to make ceramic materials in different forms. Thin films can be produced by spin-coating or dip-coating. When the sol is cast into a mould, a wet gel will form. By drying and heat-treatment, the gel is converted into dense ceramic or glass materials. If the liquid in a wet gel is removed under a supercritical condition, a highly porous and extremely low density aerogel material is obtained. As the viscosity of a sol is adjusted into a suitable viscosity range, ceramic fibers can be drawn from the sol.

Ultra-fine and uniform ceramic powders are formed by precipitation, spray pyrolysis, or emulsion techniques.

2.4 Literature review and plan of the present research

The synthesis of nanoparticles is a subject of intensive research in recent years due to their potential technological applications. Metal-oxide nanocrystals are expected to find useful applications in catalysis, magnetic data storage, energy storage and sensors [13, 14]. In particular, metal-metal binary oxide nanocrystals are of great interest owing to their unique size dependent properties and excellent processability. Different forms of Fe–Oxide, Mn–Oxide nanoparticles and Fe–Mn based binary oxides nanoparticles have potential applications in wastewater treatment, catalysis, sensors, super capacitors, rechargeable batteries and imaging technologies [15] due to their high theoretical capacity, low cost, environmental benignity, and special properties [15]. Very recently, several groups reported the synthesis of iron oxides nanoparticles, manganese oxides nanoparticles and iron-manganese binary oxides nanoparticles characterization, variety of applications and oxidative study. Some of them are cited bellow:

A. Prakash *et al.* [16] prepare nanoporous iron-oxide nanoparticles with high internal surface area using aerosol-based sol-gel method (Aero-sol-gel). They observed that nanoporous iron-oxide nanoparticles works as potential Oxidizer for Nanoenergetic Materials.

W. Wu *et al.* [17] write a review focuses on the recent development and various strategies in preparation, structure, and magnetic properties of naked and surface functionalized iron oxide NPs and their corresponding application briefly.

S. F. Hasany *et al.* [18] write a review summarizes comparative and brief study of the methods for the preparation of iron oxide magnetic nanoparticles with a control over the size, morphology and the magnetic properties.

M. Nidhin *et al.* [19] prepared iron oxide nanoparticles using polysaccharide templates. Interaction between iron (II) sulfate and template has been carried out in aqueous

phase, followed by the selective and controlled removal of the template to achieve narrow distribution of particle size.

J. Sun *et al.* [20] synthesized magnetite (Fe_3O_4) nanoparticles with a size range of 8–20 nm were prepared by the modified controlled chemical coprecipitation method from the solution of ferrous/ferric mixed salt-solution in alkaline medium. They observed that the Fe_3O_4 nanoparticles coated by sodium oleate had a better biocompatibility, better magnetic properties, easier washing, lower cost, and better dispersion than the magnetite nanoparticles coated by PEG (polyethylene glycol).

S. Bagheri *et al.* [21] generated Nanocrystalline α–Fe_2O_3 (hematite) particles by sol-gel method using gelatin as a polymerizing agent. The sol-gel synthesized α–Fe_2O_3 powder was simple, cost effective and eco-friendly in nature and also can be extended to prepare nanosized particles of other interesting materials.

L. Willis *et al.* [22]. This method employed the reactions of metal acetylacetonate precursors and oxygen containing solvents in a reaction to prepare metal oxide nanoparticles. A convenient reaction for the reparation of γ-Fe_2O_3 was discovered and had been expanded to the preparation of γ-Fe_2O_3, Mn_2O_3, Mn_3O_4, and Cr_2O_3. Characterization of these nanocrystalline materials was carried out employing transmission electron microscopy (TEM), high resolution TEM (HRTEM), X-ray diffraction (XRD) and elemental analysis.

Z. W. Chen *et al.* [23] reported a simple and effective method for the generation of bulk quantity nanorods of manganese oxide, Mn_3O_4 under surroundings of a suitable

Q. Zhou *et al* [24] reported a magnetic core-shell material, polyaniline coated Fe_3O_4 (Fe_3O_4@PANI) synthesized using a simple two-step polymerization method. They examined that the adsorption capacity (qmax) of Fe_3O_4@PANI for arsenite and arsenate in terms of monolayer adsorption were 1.066 and 1.385 mg/g, respectively.

B. A. Manning *et al.* [25] studied investigates the speciation of arsenate (As(V)) and arsenite (As(III)) after reaction with two Fe^0 materials, their iron oxide corrosion products, and several model iron oxides. They found that under aerobic conditions, the Fe^0 corrosion reaction did not cause As(V) reduction to As(III) but did cause As(III) oxidation to As(V) and from As–Fe complex.

B. An *et al.* [26] synthesized Fe–Mn binary oxides nanoparticles and tested for removal and in-situ immobilization of arsenic, As(III) and As(V), in simulated groundwater and soil. They used a water soluble starch or carboxymethyl cellulose (CMC) to prevent the particles from aggregation and facilitate in situ delivery of the particles into contaminated soil.

J. Lai *et al.* [27] prepared nanosized manganese iron oxide powder using sonochemical process. They observed that the Mn(III) content has profound effect of size and shape of the iron-oxide nanoparticles.

Kong *et al.* [28] reported Fe-Mn binary oxides loaded on zeolite is effective for the adsorption of both As(III) and As(V) in synthetic groundwater. It has high adsorption capacities of 296.23 and 201.10 mg/g for As(III) and As(V), respectively.

S. Q. Kong *et al.* [29] synthesize Fe–Mn binary oxides using coprecipitation method. They observed that it has high adsorption capacity of As(III) by using a simultaneous oxidation and co-adsorption process in synthesized groundwater.

In this study, attempt will be made to prepare iron–oxides nanoparticles, manganese–oxides nanoparticles, and a series of iron–manganese binary mixed oxides nanoparticles, also investigate their arsenic sorption properties. The iron oxide, manganese oxide and iron–manganese binary oxides precursor will be formed through a gel formation method with the reaction of $Fe(NO_3)_3$, $KMnO_4$ and starch. This method differs from the traditional sol–gel technique in that no expensive alkoxides or any hazardous chemicals are used. Another distinct advantage of this method is that it avoids the aggregation of particles and it needs only very simple equipment and the

process is very facile and it is a green process because no organic agent except the biodegradable starch is used. Arsenic (As) is an element of particular interest in terms of human and environmental health. The consumption of high concentrations of As by humans has been linked to vascular and skin diseases, Blackfoot disease, as well as cancer in the lungs, bladder, and kidneys [30]. To abate health problems associated with As in drinking water, the US EPA has decreased the previous As maximum contaminant level (MCL) from 50 μg/L (50 ppb) to 10 ppb. The most frequently detected As compounds in groundwater are oxyanions of trivalent arsenite [As(III)] or pentavalent arsenate [As(V)], and the uncharged arsenite $H_3AsO_3^0$ [As(III)] predominate under reducing conditions below pH 9.2 [31]. As(III) is about 60 times more toxic than As(V). Inorganic arsenic compounds are about 100 times more toxic than organic arsenic compounds [32]. Therefore, from a practical perspective, the primary means of treating arsenic in contaminated groundwater is to remove the inorganic As(V) and, especially, As(III).

Among the optional physical, chemical, and biological technologies for arsenic removal, adsorption is one of the most promising processes because of its cost effectiveness [33]. Iron oxides (hydroxide) have been used to adsorb arsenic from water because of their high affinity to arsenic [34]. The adsorption of As(III) by iron oxides is less significant than that of As(V) [35]. Therefore, oxidation of As(III) to As(V) is proposed as an effective option to increase the adsorption capacity and to decrease the environmental risk [36]. Manning et al. (2002) [37] studied As(III) oxidation and As(V) adsorption reactions on synthetic birnessite. Moreover, a novel Fe-Mn binary oxides preparation was synthesized by Zhang et al. (2007) [36]. However, the prepared Fe-Mn oxides are 26-μm particles, having long adsorption equilibrium time and limited adsorption capacity [36].

Nano materials have shown great potentials in a wide range of environmental applications because of the extremely small particle size, large surface area, and high reactivity [38]. It can be hypothesized therefore that decreasing the particle size of the Fe-Mn oxides from microscale to nanoscale can improve the oxidation and adsorption

of arsenic in groundwater. The reactivity of nano materials is challenged by the agglomeration effect, which decreases the effective reactive surface area. However, the tunable particle size covering uniform distribution can be obtained by utilizing chemical methods such as sol-gel, microemulsion and precipitation from metal-organic complex [39]. The mentioned methods are expensive and need multistep purification. The alternative method of template formation using starch *via* a gel formation route might promising in formation of single and binary oxides of Iron and Manganese nanoparticles. This green process requires starch a eco-friendly, abundant, low-cost, non-toxic materials - in aqueous solution along with the metal salts in controlled heating condition for the formation of a metal oxide-starch gel. Despite the potentiality of the method, a very few reports available in this respect. Consequently, in the present work attempt would be made to prepare *nps* of Fe–oxides, *nps* of Mn–oxides and *nps* of Fe–Mn binary oxides using starch assisted gel formation route and a systematic study of their structure also there sorption properties.

References

1) Schwarzenbach, R. P., Egli, T., Hofstetter, T. B., Gunten, U., and Wehrli, B., "Global water pollution and human health," *Annu Review Environ Resources.,* Vol. 35, pp. 109–136, (2010).

1) Smith, A. H., Lingas, E. O., and Rahman, M., "Contamination of Drinking-Water by Arsenic in Bangladesh: A Public Health Emergency," *Bull World Health Organ.,* Vol. 78, pp. 1093-1103, (2000).

2) Jain, C. K., and Ali, I., "Arsenic: Occurance, toxicity and speciation techniques," *Water Res.,* Vol. 34, pp. 4304–4312, (2000).

3) Mukherjee, A., Sengupta, M. K., Hossain, M. A., Ahamed, S., Das, B., Nayak, B., D. Lodh, M. M. Rahman and D. Chakraborti, "Arsenic Contamination in Groundwater: A Global Perspective with Emphasis on the Asian Scenario," *J Health Popul Nutr.,* Vol. 24, pp. 142-163, (2006).

4) Chakraborti, D., Sengupta, M. K., Rahman, M. M., Ahamed, S., Chowdhury, U. K., and Hossain, M. A., "Groundwater arsenic contamination and its health effects in the Ganga-Meghna-Brahmaputra plain," *J. Environ. Monit.,* Vol. 6, pp. 74-83, (2004).

5) Joshi, A., and Chaudhuri, M., "Removal of arsenic from ground water by iron oxide-coated sand," *J. Environ. Eng.,* Vol. 122, pp. 769–771, (1996).

6) Huang, J. G., and Liu, J. C., "Enhanced removal of As(V) from water with iron-coated spent catalyst," *Sep. Sci. Technol.,* Vol. 32, pp. 1557–1569, (1997).

7) Maji, S. K., Kao, Y. H., Liao, P. Y., Lin, Y. J., and Liu, C. W., "Implementation of the adsorbent iron-oxide-coated natural rock (IOCNR) on synthetic As(III) and on real arsenic-bearing sample with filter," *Appl. Surf. Sci.,* Vol. 284, pp. 40–48, (2013).

8) Feng, L. M., Cao, X. M., Zhu, Y., and Hu, C., "Superparamagnetic high-surface-area Fe_3O_4 nanoparticles as adsorbents for arsenic removal," *J. Hazard. Mater.,* Vol. 217, pp. 439–446, (2012).

9) Kong, S. Q., Wang, Y. X., Yu, M., and Liu, M. L.,"Adsorption-oxidation of arsenite by nano-iron-manganese binary oxide in synthesized groundwater," *Understanding the geological and meical interface of arsenic,* pp. 544–546, (2012).

10) Zhang, G., Qu, J., Liu, H., Liu, R., and Wu, R., "Preparation and evaluation of a novel Fe–Mn binary oxide adsorbent for effective arsenite removal," *Water Res.* Vol. 41, pp. 1921–1928, (2007).

11) Ivanets, A. I., Kuznetsova, T. F., and Prozorovich, V. G., "Sol-gel synthesis and adsorption properties of mesoporous manganese oxide," *Russ J Physical Chem. A.* Vol. 89, pp. 481–489, (2015).

12) Kim, H. M., Kim, S. J., and Oh, S. M., "Preparation of layered MnO_2 via thermal decomposition of $KMnO_2$ and its electrochemical characterizations," *Chem. Mater.* Vol. 11, pp. 557, (1999).

13) Nayak, S. K., and Jena, P., "Equilibrium Geometry, Stability, and Magnetic Properties of Small MnO Clusters," *J. Am. Chem. Soc.* Vol. 121, pp. 644–652, (1999).

14) Peng, X. H., Qian, X., Mao, H., and Wang, A. Y., "Targeted magnetic iron oxide nanoparticles for tumor imaging and therapy," *Int. J. Nanomedicine.* Vol. 3, pp. 311–321, (2008).

15) Prakash, A., Cormick, A. V. M., and Zachariah, M. R., "Aero-Sol−Gel Synthesis of Nanoporous Iron-Oxide Particles: A Potential Oxidizer for Nanoenergetic Materials," *Chem. Mater.,* Vol. 16, pp. 1466-1471, (2004).

16) Wu, W., He, Q., and Jiang, C., "Magnetic Iron Oxide Nanoparticles: Synthesis and Surface Functionalization Strategies," *Nanoscale Res. Lett.* Vol. 3, pp. 397–415, (2008).

17) Hasany, S. F., Ahmed, I., Rajan, J., and Rehman, A., "Systematic Review of the Preparation Techniques of Iron Oxide Magnetic Nanoparticles," *Nanoscience and Nanotechnology,* Vol. 2, pp. 148-158, (2012).

18) Nidhin, M., Indumathy, R., Sreeram, K. J., and Nair, B. U., "Synthesis of iron oxide nanoparticles of narrow size distribution on polysaccharide templates," *Bull. Mater. Sci.*, Vol. 31, pp. 93–96, (2008).

19) Sun, J., Zhou, S., Hou, P., Yang, Y., Weng, J., Li, X., and Li, M., "Synthesis and characterization of biocompatible Fe3O4 nanoparticles," *J.Bio.Mate. Res.,* Vol. 80A, pp. 333–341, (2007).

20) Bagheri, S., Chandrappa and Hamid, S. B. A., "Generation of Hematite Nanoparticles via Sol-Gel Method," *Res. J. Chem Sci.,* Vol. 3, pp. 62-68, (2013).

21) Willis, A. L., Chen, Z., He, J., Zhu, Y., Turro, N. J., and Brien, S. O., "Metal acetylacetonates as general precursors for the synthesis of early transition metal oxide nanomaterials," *J Nanomater.,* Vol. 7, pp. 7, (2007).

22) Chen, Z. W., Lai, J. K. L., and Shek, C. H., "Nucleation site and mechanism leading to growth of bulk-quantity Mn_3O_4 nanorods," *Appl. Phys. Lett.*, Vol. 86, pp. 181–911, (2005).

23) Zhou, Q., Wang, J., Liao, X., Xiao, J., and Fan, H., "Removal of As(III) and As(V) from Water Using Magnetic Core-Shell Nanomaterial Fe_3O_4@ Polyaniline," *Int. J. Green Technol.,* Vol. 1, pp. 54–64, (2015).

24) Manning, B. A., Hunt, M. L., Amrhein, C., and Yarmoff, J. A., "Arsenic(III) oxidation and arsenic(V) adsorption reactions on synthetic birnessite," *Environ. Sci. Technol.,* 36 (2002) 5455-5461.

25) An, B., Xie, W., and Zhao, D., "In Situ Immobilization of Arsenic in Water and Soil Using Polysaccharide Stabilized Iron Manganese Binary Oxide Nanoparticles" *ACS,* pp. 2015–1197, (2015).

26) Lai, J., Shafi, K. V. P. M., Ulman, A., Yang, N. L., Cui, M. H., Vogt, T., and Estournes, C., "Mixed iron-manganese oxide nanoparticles," *ACS*, Vol. 48, pp. 729–730, (2003).

27) Kong, S., Wang, Y., Zhan, H., Yuan, S., Yu, M., and Li, M., "Adsorption/oxidation of arsenic in groundwater by nanoscale Fe–Mn binary oxides loaded on zeolite," *Water Environ Res.,* Vol. 86, pp. 147–155, (2014).

28) Kong, S. Q., Wang, Y. X., Yu, M., and Liu, M. L., "Adsorption-oxidation of arsenite by nano-iron-manganese binary oxide in synthesized groundwater" *Applied Mechanics and Materials,* Vol. 319, pp. 209-212, (2013).

29) Smith, A. H., Lingas, E. O., and Rahman, M., "Contamination of Drinking-Water by Arsenic in Bangladesh: A Public Health Emergency," *Bull World Health Organ.,* Vol. 78, pp. 1093-1103, (2000).

30) Yan, X. P., Kerrich, R., and Hendry, M. J., "Distribution of arsenic(III), arsenic(V) and total inorganic arsenic in porewaters from a thick till and clay-rich aquitard sequence, Saskatchewan, Canada," *Geochim Cosmo-chim Acta,* Vol. 64, pp. 2637-48, (2000).

31) Jain, C. K., and Ali, I., "Arsenic: Occurrence, Toxicity and Speciation Techniques," *Water Res.* Vol. 34, pp. 4304–4312, (2000).

32) Mohan, D., and Pittman, C.U., "Arsenic removal from water/ wastewater using adsorbentse–A critical review," *J. Hazard. Mater.,* Vol. 142, pp. 1–53, (2007).

33) Chang, Q. G., Lin W., and Ying, W. C., "Impacts of Amount of Impregnated Iron in Granular Activated Carbon on Arsenate Adsorption Capacities and Kinetics," *Water Environ. Res.* Vol. 84, pp. 514–520, (2012).

34) Simeonidis, K., Gkinis, T., Tresintsi, S., Martinez-Boubeta, C., Vourlias, G., Tsiaoussis, I., Stavropoulos, G., Mitrakas, M., Angelakeris, M., "Magnetic Separation of Hematite-Coated Fe_3O_4 Particles Used as Arsenic Adsorbents," *Chem. Eng. J.*, Vol. 168, pp. 1008–1015, (2011).

35) Zhang, G. S., Qu, J. H., Liu, H. J., Liu, R. P., and Wu, R. C., "Preparation and Evaluation of a Novel Fe–Mn Binary Oxide Adsorbent for Effective Arsenite Removal," *Water Res.*, Vol. 41, pp. 1921–1928, (2007).

36) Manning, B. A., Fendorf, S. E., Bostick, B., and Suarez, D. L., "Arsenic(III) Oxidation and Arsenic(V) Adsorption Reactions on Synthetic Birnessite," *Environ. Sci. Technol.,* Vol. 36, pp. 976–981, (2002).

37) Masciangioli, T., and Zhang, W. X., "Peer Reviewed: Environmental Technologies at the Nanoscale," *Environ. Sci. Technol.,* Vol. 37, pp. 102–108, (2003).

38) Hyeon, T., "Chemical synthesis of magnetic nanoparticles," *Chem. Commun.* (2003) 927-934.

Chapter 3
Characterization Techniques

3.1 X-ray diffraction

The German Physicist Wilhelm Roentgen discovered X-rays in 1885. X-rays are electromagnetic waves of short wavelengths in the range of 10^{-2} to 10^{2} Å. Unlike ordinary light, these rays are invisible, but they travel in straight lines and affect photographic film in the same way as light. On the other hand, they were much more penetrating than light and could easily pass through the human body, wood, quite thick pieces of metal and other "opaque" objects.

3.1.1 Electromagnetic radiation

X-rays are electromagnetic radiation of exactly the same nature as light but of very much shorter wavelength. The unit of measurement of wavelength in the X-ray region is the Angstrom (Å), equal to 10^{-10} m and X-ray used in diffraction have wavelengths lying approximately in the range 0.5 to 2.5 Å, whereas the wavelength of visible light is of the order of 6000 Å.

X-ray therefore occupies the region between gamma and ultraviolet rays in the complete electromagnetic spectrum as shown in Fig.3.1.

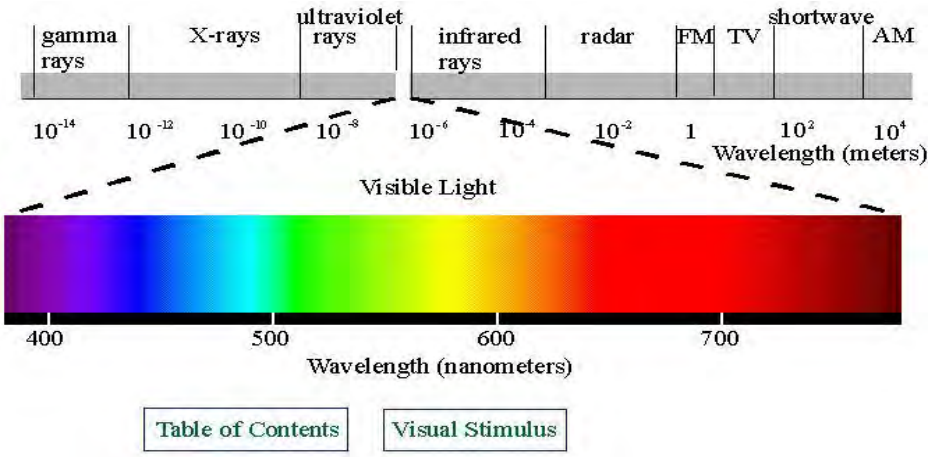

Fig.3.1: Electromagnetic spectrum

The approved SI unit for wavelength in the X-ray region is nanometer: 1 nanometer = 10^{-9}m = 10 Å.

3.1.2 Production of X-ray

We have seen that X-rays are produced whenever high-speed electrons collide with a metal target. Any X-ray tube must therefore contain (i) a source of electrons, (ii) a high accelerating voltage and (iii) a metal target. Furthermore since most of the kinetic energy of the electron is converted into heat, the latter is almost always water-cooled to prevent its melting.

All X-ray tubes contain two electrodes, an anode (the metal target) maintained, few exceptions, at ground potential, on a cathode maintained at a high negative potential, normally of the order of 30000 to 50000 volt for diffraction work. X-ray tubes may be divided into two basic types, according to the way in which sections are produced by the ionization of small quantity of gas (residual) air in a partly evacuated tube and filament tubes, in which the source of the electrons is a hot filament.

3.1.3 X-ray diffractometer

Thin sheets of the samples were prepared from the alloy ingot by rolling the ingot. Sharp strip like samples were cut from the thin sheet for Debye-Scherrer experiment. After heat treatment of the samples separately to remove strain the lattice parameter of the quenched specimen in the disordered state were measured by Debye-Scherrer method using Cu radiation. In the present case, a special technique was used to determine the lattice parameter using Debye-Scherrer method. The shape of the sample was used as the same of Debye-Scherrer method sample. But in the conventional Debye-Scherrer experiment, sharp strip sample rotates and X-ray tube and camera remain fixed. In the present case, sample was kept fixed and X-ray tube and detector were moved to the θ and 2θ ranges respectively. Instead of the film, digital data was recovered for the whole 2θ range.

After the pattern is obtained the value of 2θ is calculated for each diffraction line; set of 2θ values is the raw data for the determination of the lattice parameters of the unit cell.

A Bruker D8 X-ray diffractometer was used for the lattice parameter determination in the Materials Science Division, Atomic Energy Center, Dhaka. Fig. 3.2 shows the A Bruker D8 X-ray diffractometer,

Fig. 3.2: A Bruker D8 X-ray diffractometer

X-ray diffractometer was used to study the crystalline phases of the prepared samples. The powder diffraction technique was used with a primary beam power of 40 kV and 30 mA for Cu radiation. A nickel filter was used to reduce CuK_β radiation and finally Cu-K_α radiation was only used as the primary beam. A 2θ scan was taken from 10° to 70° to get possible fundamental peaks with the sampling pitch of 0.02° and time for each step data collection was 1.0 sec. After that data of the samples were analyzed by computer software. A schematic diagram of X-ray is shown in Fig. 3.3.

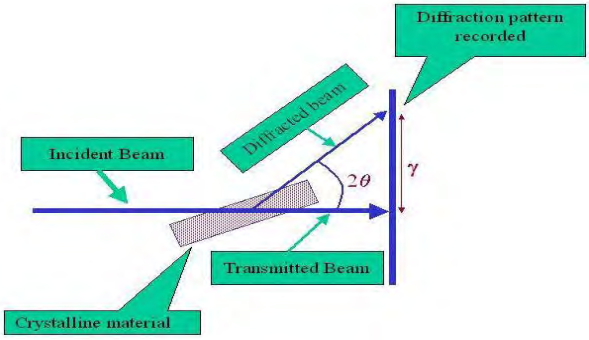

Fig. 3.3: Schematic diagram of X-ray

The aim of the present study was to determine the grain size of manganese oxides nanoparticles. The grain size of the prepared samples were determined from the strongest peak of each XRD patterns using Scherrer‟s formula,

$$D_g = \frac{0.9\lambda}{\beta cos\theta} \ldots \ldots \ldots \ldots \ldots (3.1)$$

Where D_g is the average grain size, λ is the wavelength of the radiation used as the primary beam of Cu-K_α (λ = 1.54178 Å), θ is the angle of incident in degree and β is the full width at half maximum (FWHM) of the strongest reflection in radian which was determined experimentally after correction of instrumental broadening (in the present case it is 0.07^o)

The peaks in an X-ray diffraction pattern are directly related to the atomic distance. Let us consider an incident X-ray beam interacting with the atoms arranged in a periodic manner as shown in Fig. 3.4. The atoms represented as block spheres in the figure, can be viewed as forming different sets if planes in the crystal.

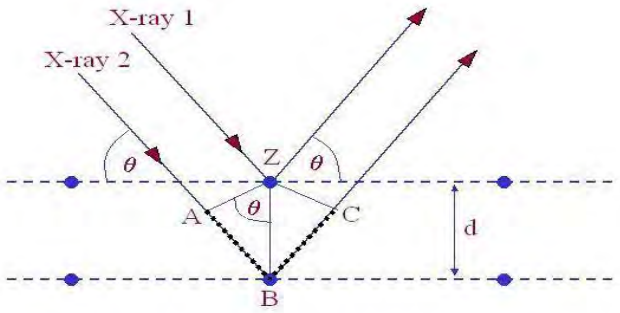

Fig.3.4: Bragg‟s diffraction pattern

For a given set of lattice plane with an inter planner distance of d, the condition for a diffraction to occur can simply written as

$$2d_{hkl}sin\theta = n\lambda \ldots \ldots \ldots \ldots \ldots (3.2)$$

which is known as Bragg‟s law. Where, λ is the wavelength of the X-ray, θ is the scattering angle and n is an integer representing the order of the diffraction.

3.1.4 Determination of nanometric grain Size by X-ray diffraction

Nanocrystalline alloys are above all crystalline and because of their crystallinity exhibit Bragg scattering peaks in X-ray diffraction experiments. However, due to their small size, significant fine particle broadening is observed in the Bragg peaks. The condition for constructive interference, reinforcement of X-ray scattering from a crystalline solid is given by Bragg"s law:

$$n\lambda = 2d\ sin\theta \ldots \ldots \ldots \ldots \ldots (3.3)$$

This equates the path difference of X-rays scattered from parallel crystalline planes spaced d = d_{hkl} apart to an integral (n) number of X-ray wavelengths λ. Here θ is the X-ray angle of incidence (and of diffraction) measured with respect to the crystalline planes. For an infinite crystal Bragg scattering occurs at discrete values of 2θ satisfying the Bragg condition, i.e., Bragg peaks are δ-functions. For finite sized crystals the peaks are broadened over a range of angles as shown in Fig. 3.5.

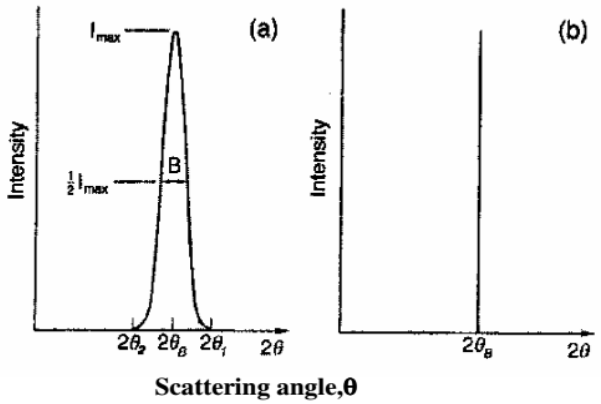

Fig.3.5: Effect of fine particle size on diffraction curves (schematic)

To better understand the phenomenon of fine particle broadening following argument of Cullity, [1] we consider a finite crystal of thickness, $D = md$, where m is an integer, and d is the distance between crystalline planes, i.e., there are m planes in D. Now if the broadened Brag peak begins at an angle $2\theta_2$ and ends at $2\theta_1$, the breadth of

the peak or full width at half maximum is given as:

$$\beta = \frac{1}{2}(2\theta_1 - 2\theta_2) = \theta_1 - \theta_2 \ldots \ldots \ldots \ldots \ldots (3.4)$$

Now consider the path differences for each of the two angles θ_1 and θ_2, for X-rays traveling the full thickness of the crystal. The width β is usually measured in radians.

We now write path difference equations for these two angles, related to the entire thickness of the crystal rather to the distance between adjacent planes.

$$2D\ sin\theta_1 = (m+1)\lambda \ldots \ldots \ldots \ldots \ldots (3.5)$$

$$2D\ sin\theta_2 = (m-1)\lambda \ldots \ldots \ldots \ldots \ldots (3.6)$$

By subtracting we find,

$$D\ (sin\theta_1 - sin\theta_2) = \lambda \ldots \ldots \ldots \ldots \ldots (3.7)$$

$$D\ 2cos\left(\frac{\theta_1 + \theta_2}{2}\right) sin\left(\frac{\theta_1 - \theta_2}{2}\right) = \lambda \ldots \ldots \ldots \ldots \ldots (3.8)$$

But θ_1 and θ_2 are both very nearly equal to θ, so that $\theta_1 + \theta_2 \approx 2\theta$ and $sin\left(\frac{\theta_1 - \theta_2}{2}\right) \approx \left(\frac{\theta_1 - \theta_2}{2}\right)$ so that the equation (3.8) can be written as

$$2Dcos\theta\left(\frac{\theta_1 - \theta_2}{2}\right) = \lambda \ldots \ldots \ldots \ldots \ldots (3.9)$$

From equation (3.4) and (3.9) we can write

$$\beta D\ cos\theta = \lambda \ldots \ldots \ldots \ldots \ldots (3.10)$$

$$D = \frac{\lambda}{\beta\ cos\theta} \ldots \ldots \ldots \ldots \ldots (3.11)$$

A more exact empirical treatment yields:

$$D = \frac{0.9\lambda}{\beta \cos\theta} \ldots \ldots \ldots \ldots \ldots (3.12)$$

which is known as the Scherrer's formula. It is used to estimate the particle size of very small crystals from the measured width of their diffraction curves.

3.1.5 Determination of nanometric lattice parameters by X-ray diffraction

A crystal consists of a periodic arrangement of the unit cell into a lattice. The unit cell can contain a single atom or atoms in a fixed arrangement. Crystals consist of planes of atoms that are spaced a distance d apart, but can be resolved into many atomic planes, each with a different d-spacing. Fig.3.6 represents the view of a crystal lattice.

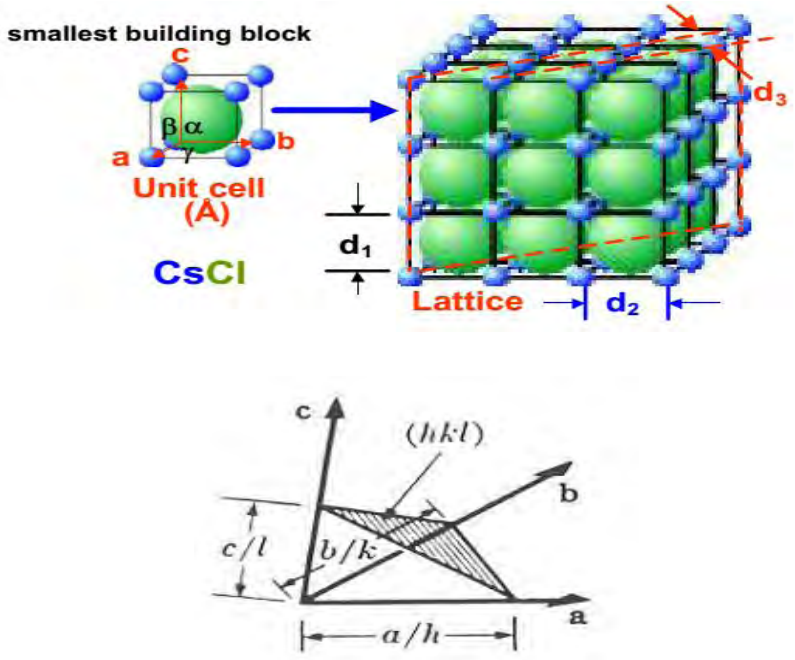

Fig.3.6: A view of crystal lattice with lattice parameters

In the figure a, b and c (length) and α, β and γ are angles between a, b and c which are lattice constants or parameters and can be determined by XRD.

The distance d, between adjacent planes in the set (hkl) may be found from the following equations where a, b, c, α, β and γ represent the lattice parameters of the unit cell [2].

$$Cubic \quad : \frac{1}{d^2} = \frac{h^2+k^2+l^2}{a^2} \ldots\ldots\ldots\ldots (3.13)$$

$$Monoclinic \quad : \frac{1}{d^2} = \frac{1}{\sin^2\beta}\left(\frac{h^2}{a^2} + \frac{k^2\sin^2\beta}{b^2} + \frac{l^2}{c^2} - \frac{2hl\cos\beta}{ac}\right) \ldots\ldots\ldots (3.14)$$

$$Tetragonal \quad : \frac{1}{a^2} = \frac{h^2+k^2}{a^2} + \frac{l^2}{c^2} \ldots\ldots\ldots\ldots (3.15)$$

The values of the lattice parameters (a, b and c) obtained for each reflected plane are plotted against the function F (θ)

$$where, F(\theta) = \frac{1}{2}\left[\frac{\cos^2\theta}{\sin^2\theta} + \frac{\cos^2\theta}{\theta}\right]^{\frac{1}{2}} \ldots\ldots\ldots\ldots (3.16)$$

Here, θ is the Bragg‟s angle

Straight lines are obtained and the accurate values of lattice parameters (a_o, b_o and c_o) are determined from the extrapolation of these lines to $\theta = 0$ [1]

3.2 Field emission scanning electron microscope (FESEM)

A FESEM is microscope that works with electrons (particles with a negative charge) instead of light. These electrons are liberated by a field emission source. The object is scanned by electrons according to a zig-zag pattern.

FESEM is a powerful tool for examining and interpreting microstructures of materials, and is widely used in the field of material science. The principle of FESEM is based on the interaction of an incident electron beam and the solid specimen [3]. Electron bombardment can produce a wide variety of emissions from the specimen, including backscattered electrons, secondary electrons, Auger electrons, X-rays, visible photons and so on.

Secondary electron imaging and X-ray analysis were the primary functions used for FESEM sample characterization in this study.

A FESEM consists of three distinct parts: an electron column; a detection system; and a viewing system. Fig. 3.7 shows a schematic of a simple scanning electron microscope. Two electron beams are controlled simultaneously by the same scan generator: one is the incident electron beam; the other is for the cathode ray tube (CRT) screen. The incident beam is scanned across the sample, line by line, and the signal from the resulting secondary electrons is collected, detected, amplified and used to control the intensity of the second electron beam. Thus a map of intensity of secondary electron emission from the scanned area of the sample will be shown on the CRT screen as variations in brightness, reflecting the surface morphologies of the specimen. Given this mechanism, the magnification of the SEM image can be adjusted simply by changing the dimensions of the area scanned on the sample surface.

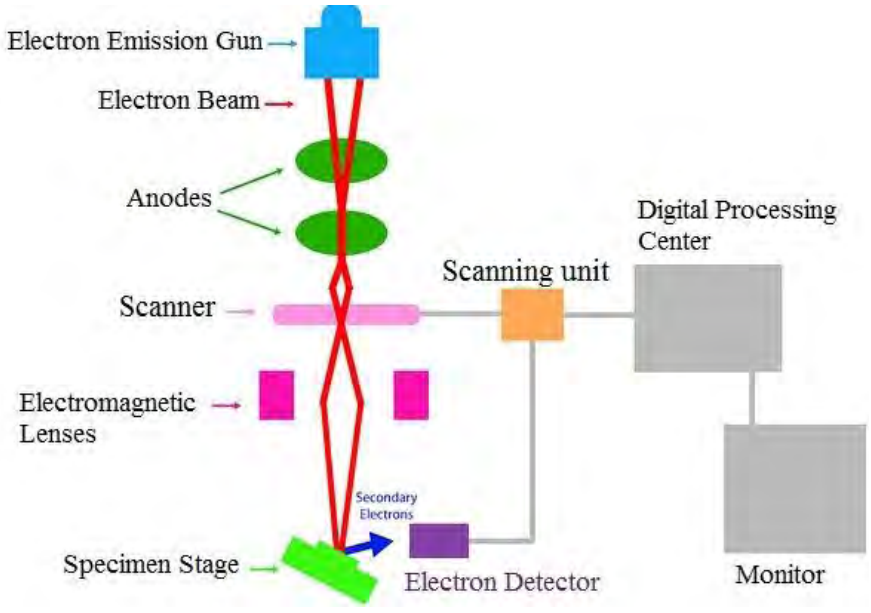

Fig.3.7: Schematic diagram of a scanning electron microscope

The spatial resolution of the FESEM is strongly dependent on diameter (spot size) of the electron probe beam at the specimen surface. In a FESEM system, the diameter of the incident electron beam is demagnified using two or more electron lenses before it reaches the sample surface. At the same time, the effective diameter of the electron source is a key factor in determining the resolution of the FESEM. The diameters of the electron beam originating from field emission electron gun are about 20-50 μm and 10 nm, respectively. Thus, field emission SEM (FESEM) is the electron source of choice for high-resolution SEM images.

The FESEM systems employed in this work. Fig.3.8 shows a photo of the JSM-7600F (FE-SEM, Tokyo, Japan) system using in the Department of Glass and Ceramic Engineering, Bangladesh University of Engineering and Technology (BUET).

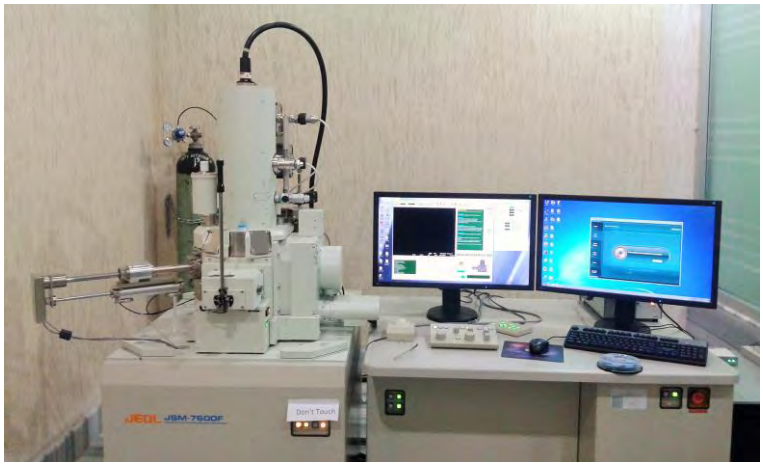

Fig.3.8: A photo of SEM JSM-7600F

3.3 Energy dispersive X-ray spectroscopy (EDX)

Energy dispersive X-ray spectroscopy (EDX or EDS) is an analytical tool predominantly used for chemical characterization. Being a type of spectroscopy, it relies on the investigation of a sample through interactions between light and matter, analyzing X-rays in this particular case. High energy electron beams (in an SEM or TEM) strike the material to be analyzed, and X-rays are emitted. These X-rays can be detected by a Si Li detector, calibrated with respect to cobalt metal emission (6.925

keV), and then used to identify and analyze the elemental composition of the specimen surface. Its characterization capabilities are due in large part to the fundamental principle that each element of the Periodic Table has a unique electronic structure and, thus, a unique response to electromagnetic waves [4].

Essentially, an X-ray photon hits a diode in the detector producing a charge that is converted into a positive voltage pulse via a field effect transistor (FET). The pulse is subsequently converted by an analogue to digital converter, into a numerical value relative to the X-ray‟s incoming energy. The signal is then assigned to a particular energy channel and registered as a single count. Counts are compiled to produce an energy dispersive spectrum. The various emission lines associated with X-rays emitted from an atom are named after the shell of the initial vacancy, i.e. K, L, M, etc. A Greek letter subscript is used to indicate the shell of the electron that fills the gap.

EDX spectra can be acquired over short time-periods and be displayed almost simultaneously, providing a near instant visual representation of the chemical analysis. Qualitative analysis determines what elements are present in a sample by identification of the peaks in the spectrum, whilst quantitative analysis is used to derive the relative abundance of the elements from their corresponding peak intensities, either compared to other elements present in the spectrum or to standards.

In this study, EDX analysis was used mainly to determine the bulk composition of the sample materials. In an SEM, a fixed accelerating voltage of 20 kV was used in order to obtain high signal intensity.

3.4 Fourier transform infrared spectroscopy (FTIR)

Fourier Transform Infrared spectroscopy (FTIR) is a technique based on the vibrations of the atoms within a molecule. An infrared (IR) spectrum is obtained by passing IR radiation through a sample and determining what fraction of the incident radiation is absorbed at a particular energy. The energy at which any peak in an absorption spectrum appears corresponds to the frequency of a vibration of a part of a

sample molecule [5]. Moreover, chemical bonds in different environments will absorb varying intensities and at varying frequencies. Thus IR spectroscopy involves collecting absorption information and analyzing it in the form of a spectrum - the frequencies at which there are absorptions of IR radiation („peaks" or „signals") can be correlated directly to bonds within the compound in question. Each inter-atomic bond may vibrate in several different motions (stretching or bending), individual bonds may absorb at more than one IR frequency. Stretching absorptions usually produce stronger peaks than bending, however the weaker bending absorptions can be useful in differentiating similar types of bonds (e.g. aromatic substitution).

The basic components of an FTIR spectrometer are shown schematically in Fig. 3.9. The radiation emerging from the source is passed to the sample through an interferometer before reaching a detector. Upon amplification of the signal, in which high-frequency contributions have been eliminated by a filter, the data are converted to a digital form by an analogue-to-digital converter and then transferred to the computer for Fourier transformation to be carried out [5]. The photo image of the instrument is shown in Fig. 3.10.

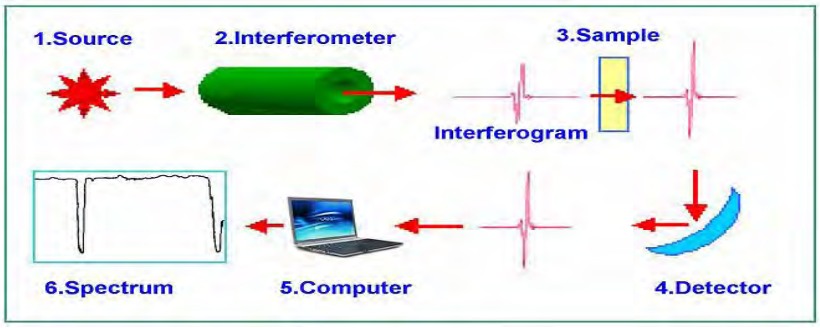

Fig.3.9: Schematic illustration of an FTIR system

Fig.3.10: A photo of Shimadzu-FTIR-8400 FTIR machine

3.5 Thermogravimetric Analysis (TGA)

Thermogravimetric analysis (TGA) is a technique in which the mass of the sample is measured against time or temperature while the temperature is changed under a certain atmosphere. This method is used for the determination of sample purity, water content, carbonate or organic content present in it and also for studying decomposition reactions. The graph of the resultant change in mass with respect to temperature is called a thermogravimetric curve [6]. An arbitrary TGA thermogram is displayed in Fig.3.11 showing the change in sample mass with the increase in temperature. In the figure each slope corresponds to a weight loss produced by the evaporation of one or more compounds of the analyzed mixture.

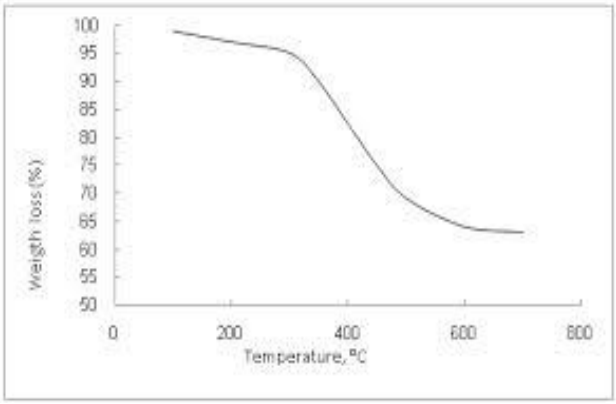

Fig.3.11: Weight loss as a function of temperature

In fact the kinetics i.e. the rate at which the property changes with temperature can

also be measured. The instrument or the detector for TGA is a balance, called a thermobalance or thermogravimetric analyzer. The TGA apparatus detects small mass changes of a specimen, kept in thermobalance, which caused with change in temperature of the furnace. The flow of temperature in furnace is under a controlled temperature program. Any change in sample weight can be detected by thermobalance. Sensitivities of the order of 0.1 μg or less are determined. It can be carried out in both inert or air atmosphere. Continuously, mass change with time and temperature is recorded. Some of the major factors affecting TGA measurements include sample size, heating rate, buoyancy, electrostatic effects, gas flow and sample holder. By analyzing the TGA curve, relative mass change with respect to the initial quantity (%) is obtained.

3.6. Analysis of heavy metals

3.6.1. Samples preparation, preservation and storage

The water samples were filtered using 41 Whatman filter paper. The filtered were preserved with ultra-pure nitric acid to bring down the pH to <2.0 and also to prevent the absorption of heavy metals onto the bottle. Samples not immediately analysed were kept in the refrigerator at 40C until further analysis.

3.6.2. Water pre-concentration technique for heavy metal analysis

250 mL of samples were taken using 250 mL volumetric flask and then transferred in a 250 mL beaker. Duplicates were taken to minimize any error. 3mL of HNO_3 was taken to each of these beakers and then placed the beaker in a hot plate at approximately 800 C covered with watch glass. When the volume of the water is reduced below 25mL, the beakers were removed from hot plate cooled at room temperature. The samples were then transferred into 25mL volumetric flask through filtration by 40 Whatman filter paper, the watch glass and beaker were rinsed with de-ionized water and then poured into the flask up to the level. Then the pre-concentrated samples were taken in 25mL polyethylene vials. Blank were prepared with 3 mL

HNO_3 followed by the similar process. Then the vials were kept to the refrigerator for the next step of the analysis. All chemicals and standard solutions used in the study were obtained from Merck, India /Germany and were of analytical grade. De-ionized water was used throughout the study. All containers and glassware were thoroughly cleaned with detergent powder then soaked in 10% HNO_3 for 24 hours and finally rinsed with de-ionised water for several times.

3.6.3. Quantitative analysis by AAS

FAAS is used to determine the concentration of an absorbing species in a sample is determined by applying Beer-Lamberts Law. Light at the resonance wave length of initial intensity I_0 is focused on the flame all containing ground state atom. The initial light intensity is decreased onto the detector where the reduced intensity (i) is measured. The amount of the absorbed is determined by comparing I_1 to I_0. Absorbance is the most convenient term and purely a mathematical quantity for characterizing light absorption, as this quantity follows a linear relationship with concentration. Bear- Lamberts Law defines this relationship:

K = absorption co- efficient
L = length of the absorbing cell
I_0 = incident length
I_1 = transmitted light

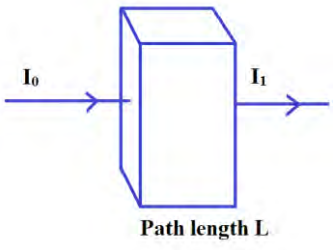

Fig.3.12: Principle of AAS.

The equation simply states that the absorbances is directly proportional to the concentration of the absorbing species for a given set of instrumentation conditions. The relation is A∞C. When the absorbances of the standard solutions containing known concentrations of analyte are measured and the absorbance data are plotted against concentration, a calibration curve is established. As the concentration and absorbance increase, non-ideal behaviour in the absorption process can cause

deviation from linearity. After such calibration is established the absorbance of solutions of unknown concentrations may be measured and the concentrations determined from the calibration. Concentration is determined by the following formula:

$$\text{Concentration (ppm)} = \frac{\text{absorbance}}{\text{Slope of the calibration curve}} \text{factor}$$

3.6.4. Hydride generation atomic absorption spectrometer (HGAAS)

In this study Varian AA280Z HGAAS is used for the determination of Arsenic (As) presented in the collected sample. In hydride generation sampling systems for atomic absorption, samples are reacted in an external system with a reducing agent, usually sodium borohydride. Gaseous reaction products are then carried to a sampling cell in the light path of the AA spectrometer. The gaseous reaction products are the volatile hydrides. These molecular species are not capable of causing atomic absorption. To dissociate the hydride gas into free atoms, the sample cell must be heated. In some hydride system, the absorption cell is mounted over the burner head of the AA spectrometer, and the cell is heated by an air acetylene flame. In other systems, the cell is heated electrically. In either case, the hydride gas is dissociated in the heated cell in to free atoms, and the atomic absorption rises and falls as the atoms are created and then escape from the absorption cell. The maximum absorption reading, or peak height, or the integrated peak area is taken as analytical signal. The accuracy and detection limits depend on the proper isolation of hydrade.

The reaction sequence for **As** may be represented as:

$$As_{(sol)} \xrightarrow{NaBH_4/[H^+]} AsH_3 \xrightarrow{Heat\ \ in\ \ Falme} As^0_{(gas)} + H_2$$

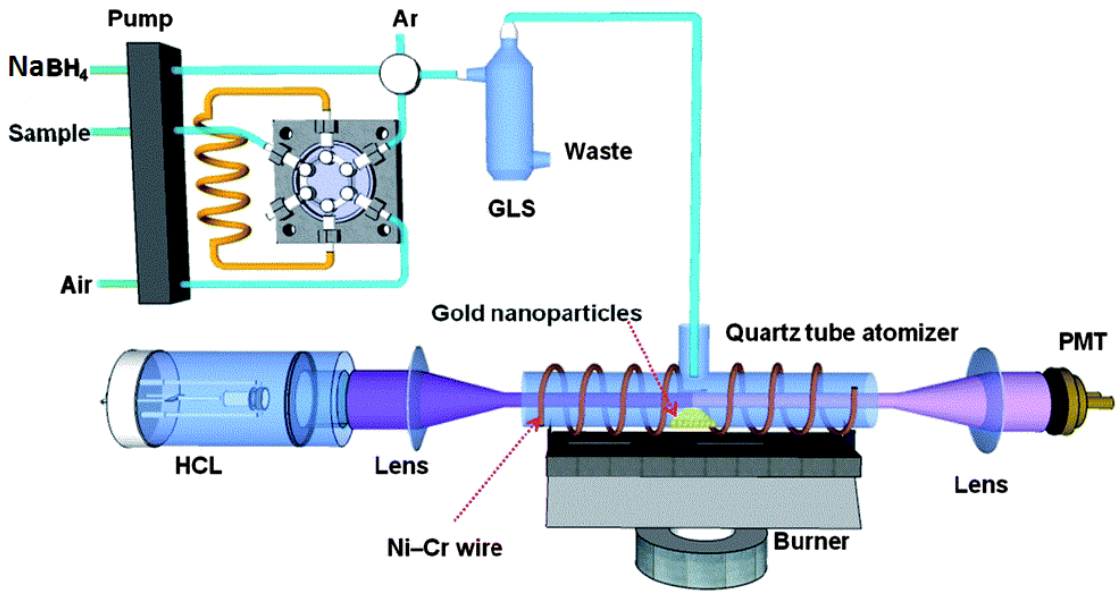

Fig.3.13: Schematic diagram of hydride generation system.

References

1) Cullity, B. D., "Elements of X-ray diffraction," *Addision-Wesley,* 1972.

2) Suryanarayana, C., and Norton, M. G., "X-ray Diffraction, A Practical Approach."*Plenum Press,* 1998.

3) Grundy, P. J., and Jones, G. A., (1976) *Electron microscopy in the study of materials*. Edward Arnold Publishers Limited.

4) http://en.wikipedia.org/wiki/Energy-dispersive X-ray spectroscopy

5) Stuart, B., (1996) *Modern Infrared Spectroscopy.* John Wiley & Sons Ltd. West Sussex, England, 1996.

6) Dean, J. A., (1995) *The Analytical Chemistry Handbook.* New York. McGraw Hill, Inc.

Chapter 4
Experimental

4.1 Materials and instruments

4.1.1 Chemical and reagents

The chemicals and reagents used in this work were analytical grade and used without further purification. De-ionized water was used as solvent to prepare most of the solutions of this work. The chemicals and reagents used in this work are listed below:

(i) Iron (III) nitrate purified (Merck, Germany)
(ii) Potassium permanganate (Merck, India)
(iii) Nitric acid 65% (Merck, Germany)
(iv) Starch soluble extra pure (Merck, Germany)
(v) pH buffer capsules (Merck, Germany)
(vi) Sodium hydroxide pellets pure. (Merck, Germany)
(vii) $Na_2HAsO_4.7H_2O$ (E. Merck, India)
(viii) Arsenic Trioxide (Qualikems, India)

4.1.2 Instruments

Analysis of the samples was performed using the following instrument

(i) X-ray Diffractometer (Philips, Expert Pro, Holland)
(ii) Fourier Transform Infrared Spectrophotometer (Shimadzu-FTIR-8400)
(iii) Field Emission Scanning Electron Microscopy (JSM-7600F, Tokyo, Japan)
(iv) Atomic absorption spectrometer (Varian, AA240)
(v) TGA machine (TGA-50, Shimadzu, Japan)
(vi) Furnace (Naber Therm, N-7, Germany)
(vii) pH meter (Jenway 3510 pH meter)
(viii) Centrifuge machine (Jenway model 3510)
(ix) Digital Balance (Scientech SA 120)

4.2 Synthesis of Fe_2O_3 oxide nanoparticles

Iron oxide (α–Fe_2O_3) nanoparticles were synthesized by gel formation method using iron nitrate as an iron source and starch as polymerizing agent. 50 mL of 0.248 M iron nitrate solution added with 200 mL of 25% starch solution with the help of burette under vigorous magnetic stirring. After that the so prepared solution was continuously stirred for few hours (4 hours) until the gel is formed. The as prepared gel is dried at 80˚C temperature 48 hours. Then the precursor was dispersed into water and washed with DI water for several times. Then the precursor was heat treated for 650˚C for 4 hours to form α–Fe_2O_3 nanoparticles.

4.3 Synthesis of MnO_2 oxide nanoparticles

Mn-oxide was prepared by a gel formation route based on reduction of $KMnO_4$ with starch. The gel precursor was obtained by adding 50 mL of 0.632 M $KMnO_4$ solution into 200 mL of 25% starch solution with the help of burette under vigorous magnetic stirring. After addition, the formed solution was continuously stirred for few hours (4 hours) at 80˚C until the gel is formed. The solution was set aside to gel undisturbed for 24 hours. Then gel is dried at 80˚C temperature for 48 hours. Then the residue was dispersed in water and excess K^+ was washed with de-ionized water and centrifuge at 3000 rpm for 15 min for several times. Then the precursor was heat treated at 650˚C for 4 hours to form MnO_2 nanoparticles.

4.4 Synthesis of Fe–Mn binary oxide nanoparticles

A series of Fe–Mn binary oxide nanoparticles were synthesized at 1:0.64, 1:1.28, and 1:2.55 1 Fe:Mn molar ratios at elevated temperature. The Fe–Mn binary oxides were prepared according to the following procedure: A certain amount of ferric nitrate ($Fe(NO_3)_3.9H_2O$) and potassium permanganate ($KMnO_4$) were dissolved in 100 ml deionized water in different conical flask. The Fe–Mn molar ratio was adjusted to the pre-determined value via changing the amount of $Fe(NO_3)_3.9H_2O$ or $KMnO_4$ added under vigorous magnetic stirring. Then the so prepared $Fe(NO_3)_3.9H_2O$ and $KMnO_4$

solutions were added drop wise to the 200 mL 25% of starch solution. After that the prepared solution was continuously stirred for few hours (4 hours) until the gel was formed. Then the gel was set for 24 hours. The as prepared gel was dried at 60 ˚C for 48 hours. Then the residue was dispersed in water and excess K^+ and other impurities was washed with de-ionized water and centrifuged at 3000 rpm for 15 min for several times. Then the precursor was heat-treated at 650 ˚C in air atmosphere for four hours using furnace. The dried product was then stored in a desiccator.

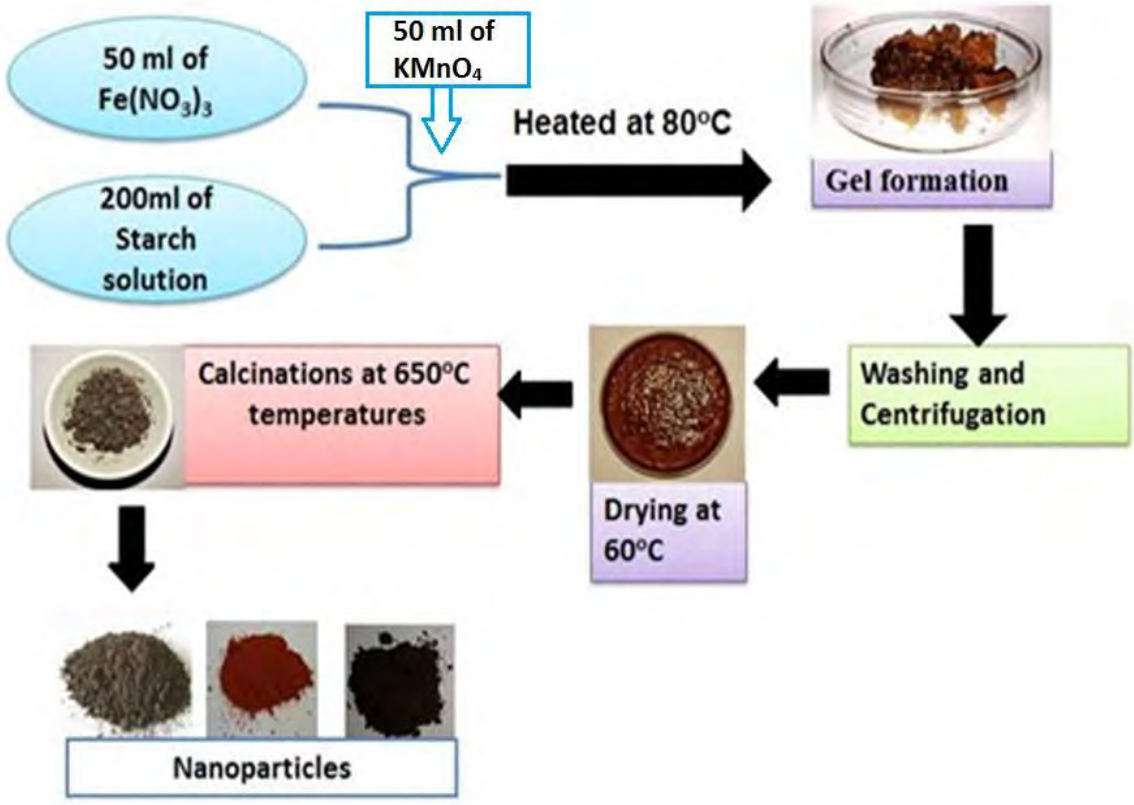

Fig.4.1: Schematic diagram of Fe–Mn binary oxides nanoparticles synthesis process.

4.5 Spectral analysis

4.5.1 X-ray diffraction

Iron oxide, manganese oxide and iron–manganese binary oxide nanomaterials were analyzed for their X-ray diffraction pattern in the powder state. The powder samples were pressed in a square aluminum sample holder (40mm × 40mm) with a 1 mm deep rectangular hole (20mm x 15mm) and pressed against an optical smooth glass plate. The upper surface of the sample was labeled in the plane with its sample holder. The sample holder was then placed in the diffractometer.

4.5.2 Energy dispersive X-ray (EDX) spectra

Elemental analyses of the synthesized iron oxide, manganese oxide and iron–manganese binary oxide nanomaterials were performed by EDX spectra. The dried powders of Iron oxide, manganese oxide and iron–manganese binary oxide nanomaterials were placed on a 1 cm × 1cm conducting copper plate. The copper plate was then placed on a conducting carbon glued strip. The sample was then placed in the main FESEM chamber integrated with the EDX instrument.

4.5.3 Infrared spectra

The infrared spectra of the dried samples of iron oxide, manganese oxide and iron–manganese binary oxide nanomaterials were recorded on an FTIR spectrometer in the region of 4000 – 400 cm^{-1}. IR spectra of the solid samples were frequently obtained by mixing and grinding a small amount of materials with dry and pure KBr crystals. The mixing and grinding were done in a mortar by a pestle. The powder mixture was then compressed in a metal holder under a pressure of 8–10 tons to make a pellet. The pellet was then placed in the path of IR beam for measurements.

4.6 Surface morphology

The surface morphology of the iron oxide, manganese oxide and iron–manganese binary oxide nanomaterials was adopted using Field Emission Scanning Electron

Microscopy. The dried powders of the synthesized iron oxide, manganese oxide and iron–manganese binary oxide nanomaterials were dispersed on a conducting carbon glued strip separately. The sample loaded strip was then mounted to a chamber that evacuated to ~ 10^{-3} to 10^{-4} torr and then a very thin gold layer (~few nanometers thick) were sputtered on the sample to ensure the conductivity of the sample surface. The samples were then placed in the main SEM chamber to view its surface. The system was computer interfaced and thus provides recording of the surface images in the computer file for its use as hard copy.

4.7 Sorption experiments

4.7.1. Stock solution preparation

Stock solutions of arsenic(III), with a concentration of 1000 ppm, was prepared by dissolving As2O3 in sodium hydroxide solution using deionized water, pH was adjusted to 7.0. Stock solution of arsenic(V), with a concentration of 1000 ppm, was prepared in the similar away by dissolving disodium hydrogen arsenate heptahydrate ($Na_2HAsO_4.7H_2O$) in deionized water at a pH of 7.0. Again the stock solution containing As(III) and As(V) species was prepared mixing the equal volume of the as prepared stock solution of arsenic(III) and arsenic(V).

4.7.2. Effect of Fe:Mn molar ratio on arsenic sorption

To determine the optimal molar Fe–Mn ratio, batch tests were carried out by adding 20mg of prepared sorbents into 150 mL glass vessels, containing 50 mL of 50 ppm arsenic solution. The pH of the solutions was adjusted around 7.0 during shaking process by using buffer capsules. The equilibrium pH was measured and the supernatant was filtered through Whatman grade 40 ashless filter paper after the solutions were mixed for 24 hours. Then the supernatant was centrifuged for 15 min for more purity of supernatant. After that the supernatant were collected for Varian AA280Z HGAAS for the determination of Arsenic (As) concentration .

Chapter 5
Results
And
Discussion

5.1 Preparation of iron oxide, manganese oxide and Fe–Mn binary oxides

The condition of starch–Fe, starch–Mn and starch–Fe–Mn gel formation were not well reported and as a result trial and error method was applied to in this present investigation. The conditions for the formation of a gel with the target metal oxides were established in the laboratory as follows.

- **Starch–Fe gel:** 0.248M $Fe(NO_3)_3$ solution, 25% starch solution and reaction temperature was 80˚C.
- **Starch–Mn gel:** 0.632M $KMnO_4$ solution, 25% starch solution and reaction temperature was 80˚C.
- **Starch–Fe–Mn gel:** 0.248M $Fe(NO_3)_3$ solution, 0.632M $KMnO_4$ solution, 25% starch solution and reaction temperature was 80˚C.

The as prepared starch–Fe, starch–Mn and starch–Fe–Mn precursor were heat treated in a muffle furnace at temperature 650 °C for four hours.

(a) No iron-starch gel was formed. (b) Nice iron starch gel was formed.

Fig. 5.1: Formation iron starch-iron gel (a) No starch-iron gel was formed and. (b) Nice starch-iron gel was formed.

5.2 Proposed mechanism for M-oxides nanoparticles formation in starch matrix

From the recent microscopic and spectral studies [1] it has been confirmed that the polymeric structure of starch provides a helical-shaped carbonaceous matrix, carrying multiple polyol groups, which may create a protective and functionalized surrounding shield for nanoparticles. The constituent hydroxyl groups could be involved both in intra- or intermolecular supramolecular associations, but are able also to coordinate transitional metal ions, maintaining the nanoparticles highly aggregated. Moreover, the starch granules swell in aqueous solution and, at temperatures ranging between 50˚Cand 90˚C, the natural polysaccharide forms a gel, which could incorporate and disperse in an uniform fashion the incipient centers of nucleation of the nanoparticles.

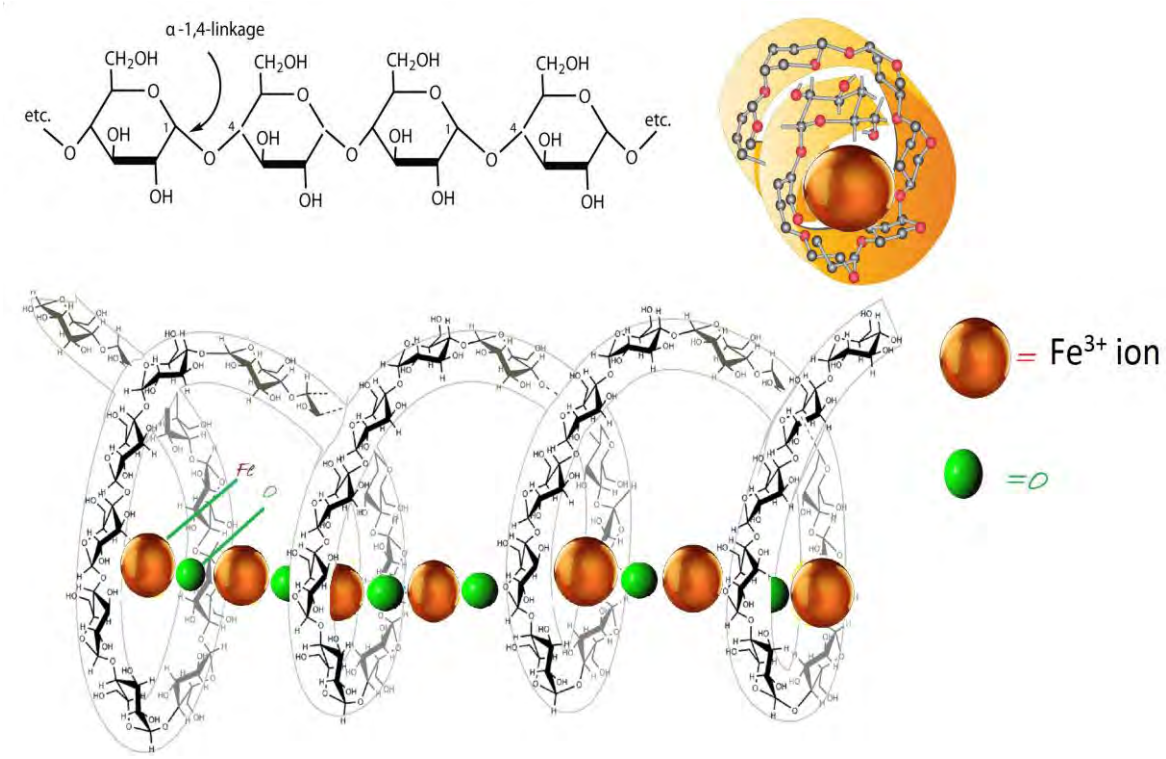

Fig. 5.2: Schematic diagram representing the Fe-oxide nanoparticles formation in starch matrix.

5.3 Structural Characterization

5.3.1 X-ray diffraction analysis

5.3.1.1 Phase identification

The X-ray Diffraction (XRD) patterns of the samples are obtained as a function of Bragg angle, 2θ with Cu-K_α radiation of wavelength λ = 1.54178 Å using a Bruker X-ray diffractometer as described in the Section 3.1. Fig.5.3 shows the XRD patterns of as prepared α-Fe_2O_3 nanoparticles. The diffraction peaks correspond to the Rhombohedral, space group R-3c (167) α-Fe_2O_3 single phase (ICSD Collection Code: 173655FIZ173655)

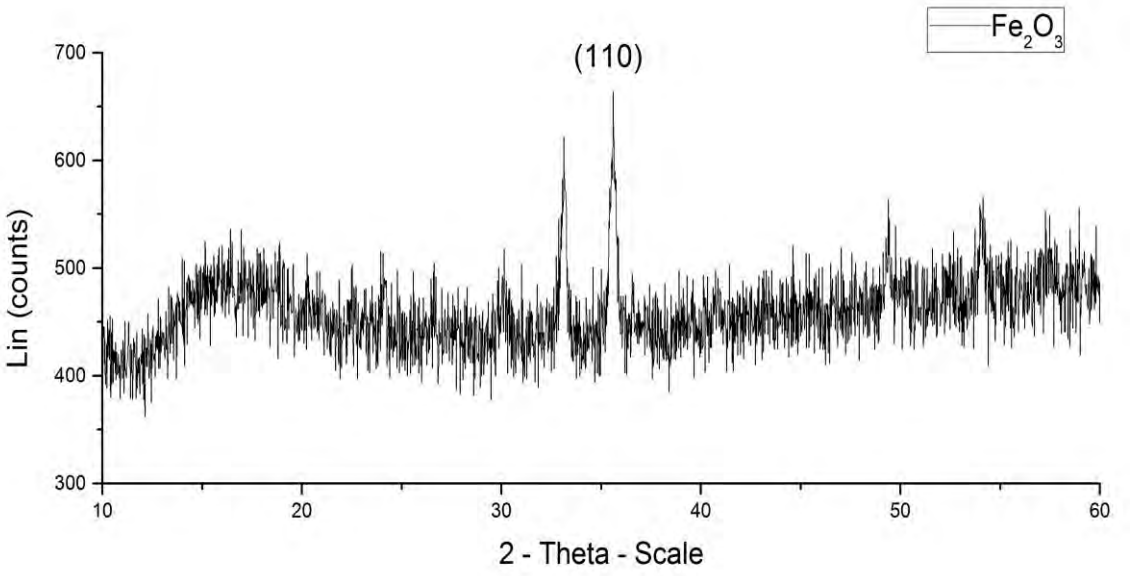

Fig. 5.3: XRD patterns of α-Fe_2O_3 nanoparticles heat treated at temperatures 650 °C.

From the XRD data the lattice constants were a = 5.035 A˚, b= 5.035 A˚, c=13.750 A˚ for Fe_2O_3 nanoparticles.

Fig.5.4 shows the XRD patterns of as prepared MnO_2 nanoparticles. The diffraction peaks correspond to the Manganese Oxide also called: α-MnO_2 (JCPDS Card 14-644). From the XRD data the crystal structure was Body-centered tetragonal, lattice constants were a= 9.784 A˚, b= 9.784 A˚, c= 2.863 A˚.

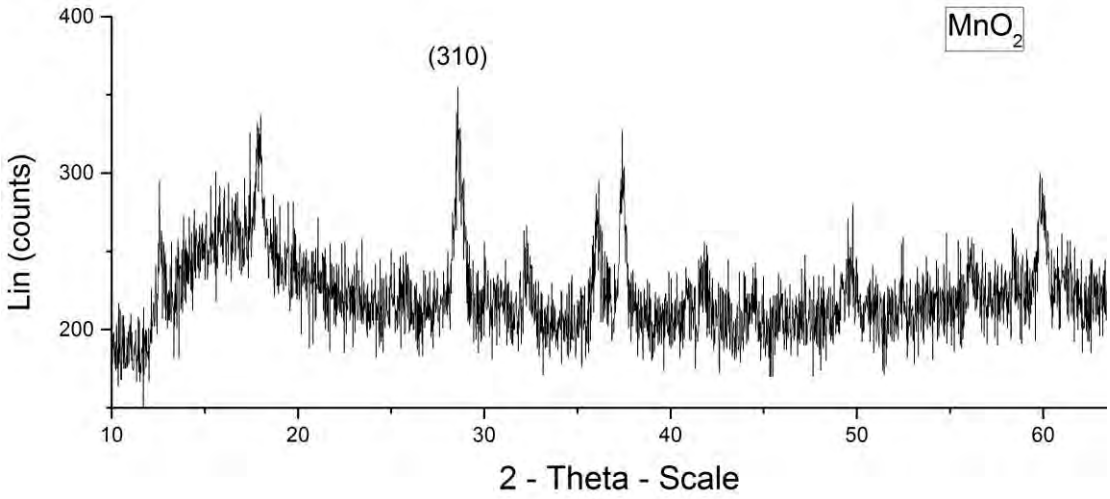

Fig. 5.4: XRD patterns of MnO_2 nanoparticles heat treated at temperatures 650 °C.

Fig.5.5 shows the XRD patterns of as prepared Fe–Mn binary oxide nanoparticles. The diffraction peaks for Fe–Mn binary oxide nanoparticles correspond to the Fe_3O_4 & Mn_3O_4 (JCPDS card no. 86–1354 and JCPDS card no. 75-0626). From the XRD data it indicated that there were two types of oxides present. One is Fe_3O_4 and another is Mn_3O_4. The crystal structure of Fe_3O_4 was Face-centered cubic, lattice constants were a=8.396 A˚, b=8.396 A˚, c=8.396 A˚ (JCPDS card no. 86–1354). The crystal structure of Mn_3O_4 Face-centered cubic and lattice constants were a=8.420 A˚, b=8.420 A˚, c=8.420 A˚.

Therefore, from the XRD patterns it can be concluded that Fe–Mn binary oxide nanoparticles with Face-centered cubic crystal geometry have been synthesized via a gel formation route by the reaction of $KMnO_4$ and $Fe(NO3)_3$ with starch at 80 °C. It was noteworthy that the presence of Mn changes the crystal structure of the nanoparticles as well as oxide from. It was observed that when they were treated individually with starch from Fe_2O_3 (rhombohedral) & MnO_2 (body-centered tetragonal). In the presence of Mn they from Fe_3O_4 & Mn_3O_4 both were face-centered cubic.

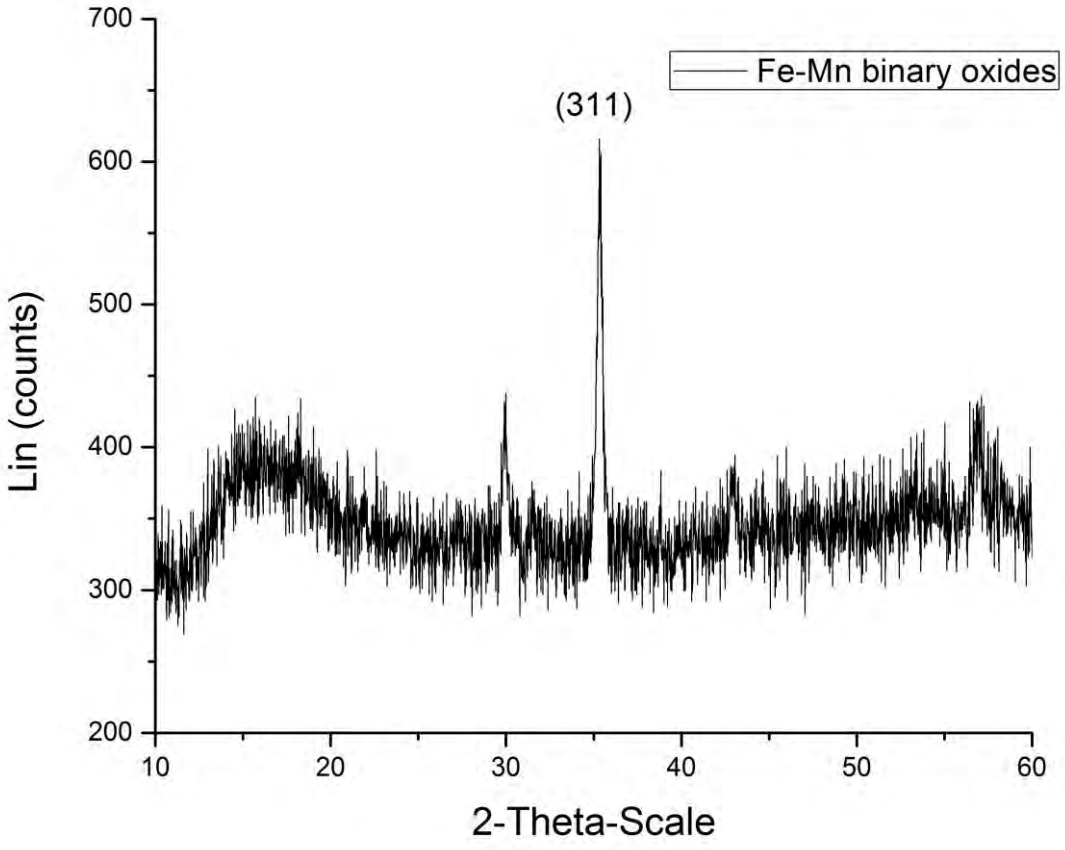

Fig. 5.5: XRD patterns of Fe–Mn binary oxide nanoparticles heat treated at temperatures 650 °C.

5.3.1.2 Crystallite size and lattice parameters

The crystallite size of the α-Fe_2O_3 MnO_2, Fe–Mn binary oxide nanoparticles nanomaterials were calculated using the procedure mentioned in Section 3.1.4. The crystallite sizes were measured from the base peaks of (110), (310), (311) and (311) for Fe_2O_3 MnO_2, Fe_3O_4, and Mn_3O_4 respectively and are summarized in Table 5.1. The lattice parameters of Fe_2O_3 MnO_2, Fe_3O_4, and Mn_3O_4 nanomaterials were calculated following the procedure mentioned in Section 3.1.5 and are also summarized in Table 5.1

Table 5.1: Crystallite size and lattice parameters of α-Fe_2O_3 MnO_2, Fe_3O_4, and Mn_3O_4 nanoparticles.

Oxides	**Crystallite size (nm)**	**Crystal system**	**Lattice parameters**		
			a (Å)	**B** (Å)	**c** (Å)
Fe_2O_3	21	Rhombohedral	5.035	5.035	13.750
Fe_3O_4	21	Face-centered cubic.	8.396	8.396	8.396
MnO_2	15	Body-centered tetragonal	9.784	9.784	2.863
Mn_3O_4	21	Face-centered cubic.	8.420	8.420	8.420

5.3.2 Energy dispersive X-ray spectral analysis

Elemental analyses of the α-Fe_2O_3, MnO_2, Fe–Mn binary oxide nanoparticles have been performed by Energy Dispersive X-ray (EDX) method. The principle of EDX is described in Section 3.3. The EDX patterns are presented in Fig. 5.6 - 5.8. The peaks observed at 0.525 keV for K lines of O, 6.398 keV for K lines of Fe,0.277 keV for k lines of C and at 5.894 keV for K lines of Mn elements. The percentages of Fe and O were determined from the intensity of the lines and are summarized in Table 5.2 for iron-oxides nanoparticles. Table 5.3 for elemental composition of Mn-oxides.

Table 5.2: Elemental composition of Fe-oxides nanoparticles

Sample location	Iron (%)	Oxygen (%)	Carbon (%)
1	50.37	35.59	14.04
2	49.78	35.31	14.91
3	52.18	33.83	14.00

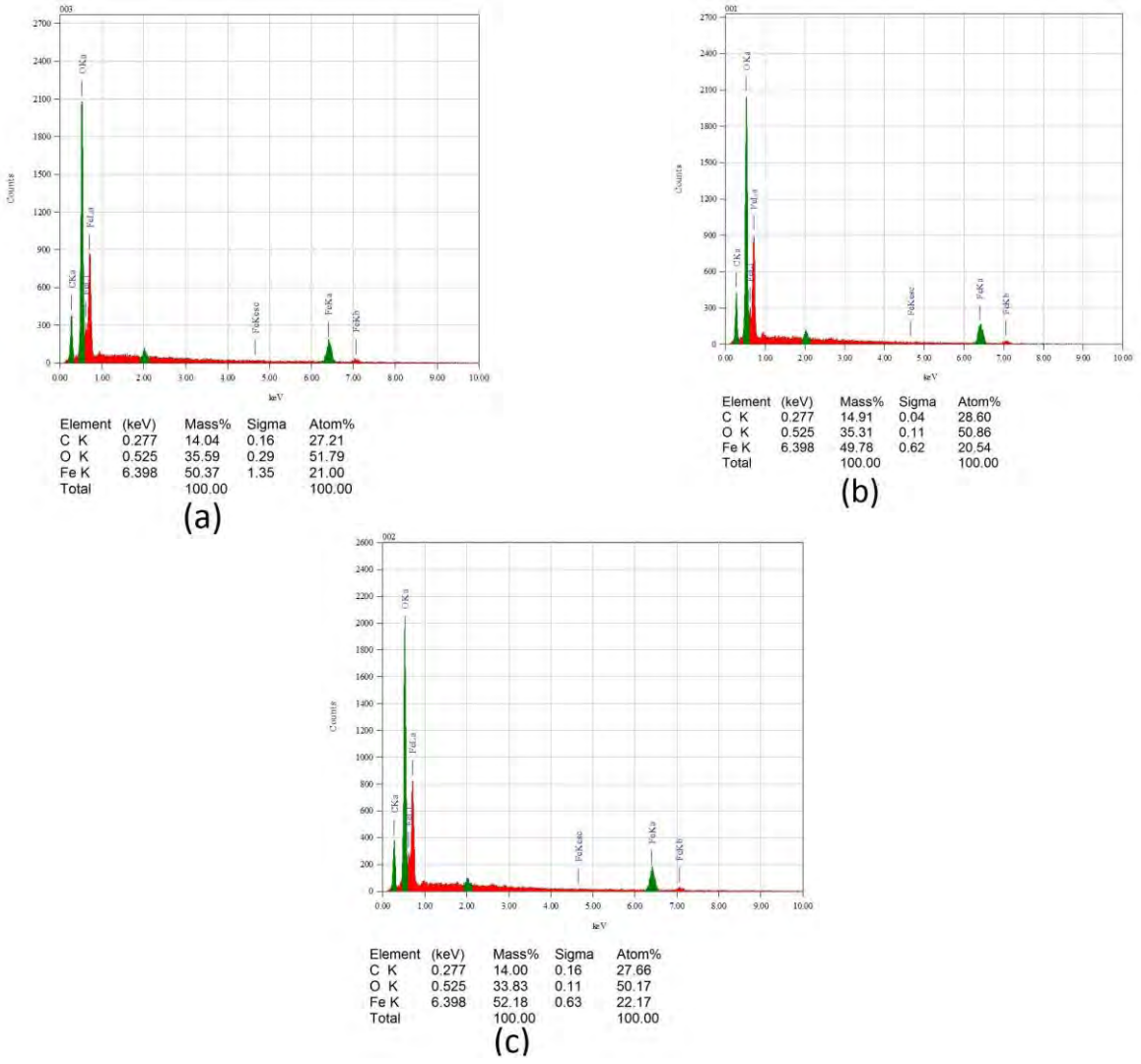

Fig. 5.6: EDX analysis of Fe_2O_3 nanoparticles at (a) location 1, (b) location 2, and (c) location 3.

Table 5.3: Elemental composition of Mn-oxides nanoparticles

Sample location	Manganese (%)	Oxygen (%)	Carbon (%)
1	74.08	13.92	12
2	74.15	13.70	12.15
3	73.05	14.23	12.72

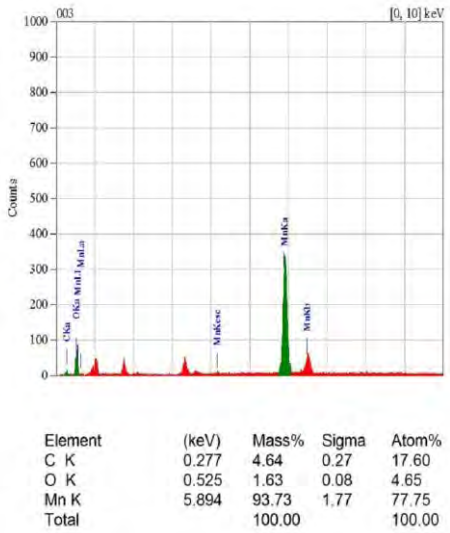

(a)

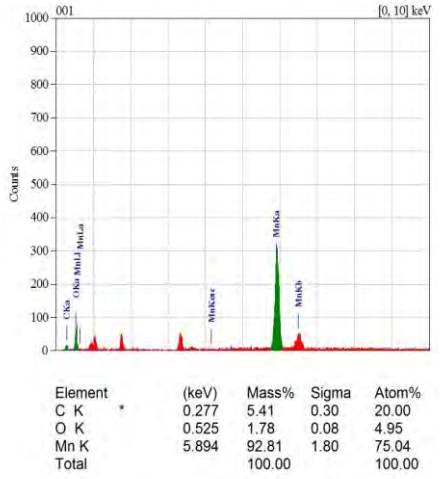

(b)

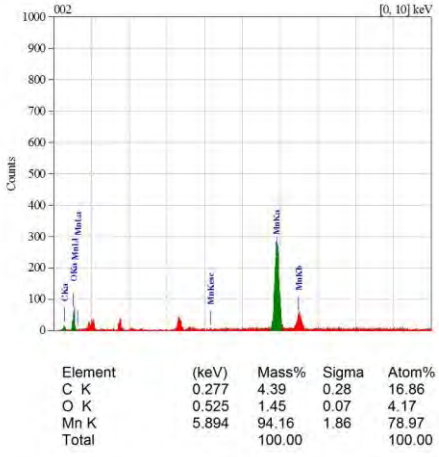

(c)

Fig.5.7: EDX analysis of MnO_2 nanoparticles at (a) location 1, (b)location 2, (c) location 3.

Table 5.4: Elemental composition of Fe–Mn binary-oxides nanoparticles.

Sample location	Iron (%)	Manganese (%)	Oxygen (%)	Carbon (%)
1	23.51	8.20	28.21	40.08
2	22.12	8.48	29.57	39.83
3	28.88	8.34	26.26	36.52

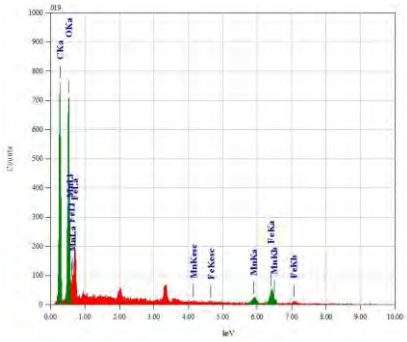

Element	(keV)	Mass%	Sigma	Atom%
C K	0.277	40.08	0.31	58.85
O K	0.525	28.21	0.40	31.10
Mn K	5.894	8.20	0.66	2.63
Fe K	6.398	23.51	1.27	7.42
Total		100.00		100.00

(a)

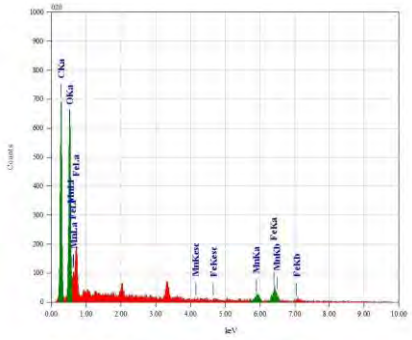

Element	(keV)	Mass%	Sigma	Atom%
C K	0.277	39.83	0.32	58.03
O K	0.525	29.57	0.42	32.34
Mn K	5.894	8.48	0.71	2.70
Fe K	6.398	22.12	1.30	6.93
Total		100.00		100.00

(b)

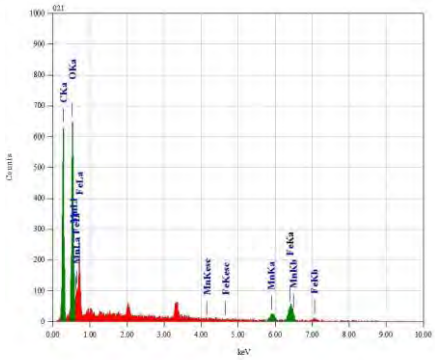

Element	(keV)	Mass%	Sigma	Atom%
C K	0.277	36.52	0.31	56.83
O K	0.525	26.26	0.38	30.67
Mn K	5.894	8.34	0.68	2.84
Fe K	6.398	28.88	1.41	9.67
Total		100.00		100.00

(c)

Fig.5.8: EDX analysis of Fe–Mn binary-oxides nanoparticles at (a) location 1, (b) location 2, (c) location 3.

5.3.3 Fourier transform infrared (FTIR) analysis

Figure 5.9 shows the FT-IR spectrum of α-Fe_2O_3 powder. According to figure 5.9 the small absorption peak in the range of 3300–3600 cm^{-1} is observed. This peak is centered at 3456 cm^{-1} corresponds to the stretching vibration of intermolecular hydrogen bond (O–H) existing between the adsorbed water molecules [2–5]. Absorption signal near 2360 cm^{-1} Indicate the presence of CO_2, this CO_2 somehow incorporated within the structure of α-Fe_2O_3 [6]. The absorption pick around 1627 cm^{-1}, is due to the asymmetric bending vibration of C=O [7]. Presence of strong band at 1056 cm^{-1} shows the C-O stretching vibration[8]. Broad peaks at 556.48 cm^{-1}may correspond to Fe-O stretching vibration mode, 466 cm^{-1} are assigned to Fe-O bending vibration mode of α-Fe_2O_3 respectively [9].

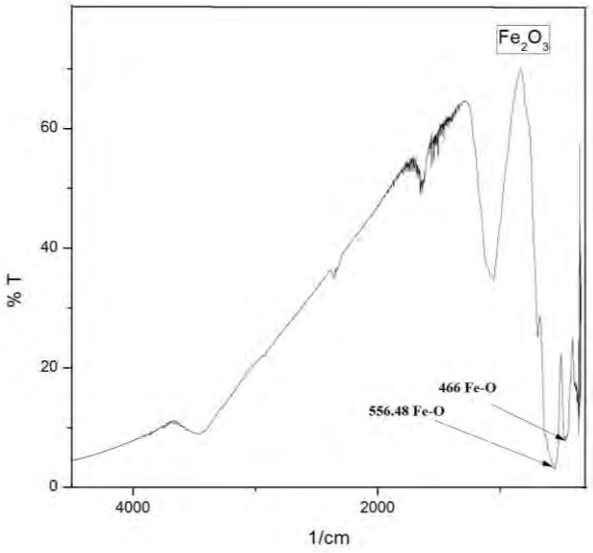

Table 5.5: Relevant FTIR bands of Fe_2O_3 nanoparticles.

Frequency (cm^{-1})	Band Assignments
3456	ν_3 (OH) (Coordinated water)
2360	CO_2
1627	C=O asymmetric bending vibration
1056	C-O stretching vibration
556.48	Fe-O stretching vibration
466	Fe-O bending vibration

Fig.5.9: FTIR spectra of Fe_2O_3 nanoparticles.

FTIR spectra of the MnO_2 samples are shown in Fig.5.10. Oxides and hydroxides of metal nanoparticles generally gives absorption peak in the finger print region i.e. below wavelength of 1000 nm arising from inter-atomic vibrations. The bands at 595 cm^{-1}, 532.37 $cm^{-1}$and 528.51 cm^{-1} are attributed due to the valency vibration ν_3 which represent the stability of the Mn^{3+}–O bond [10].A small pic at 706 cm^{-1} represented the presence of Mn^{4+} cations [11]. Broad absorption peaks centered at around 3448.8

$cm^{-1}$and 1635.6 cm^{-1} are caused by the absorbed water molecules and carbon dioxide respectively [12]. Absorption signal near 2362.8 cm^{-1} Indicate the presence of CO_2 somehow incorporated within the structure in specific local environments [6]. The presence of strong band at 1056 cm^{-1} shows the C-O stretching vibration [8]. From the above result it can be concluded that the synthesized nanomaterial was manganese oxide.

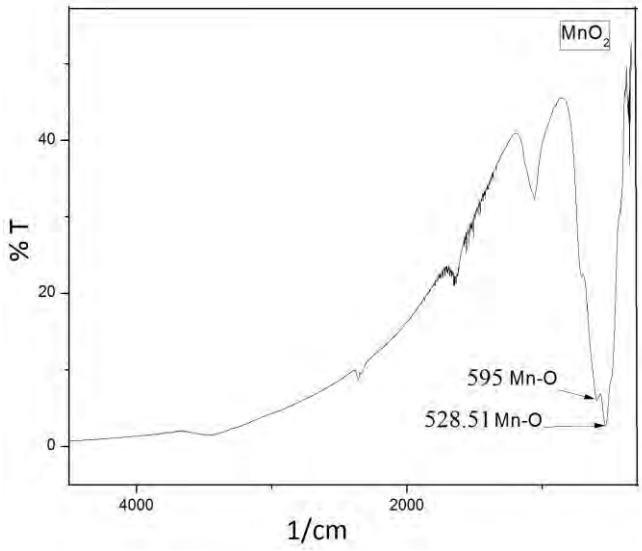

Table 5.6. Relevant FTIR bands of MnO_2 nanoparticles.

Frequency (cm^{-1})	Band Assignments
3448.8	v_3 (OH) (Coordinated water)
2362.8	CO_2
1635.6	C=O asymmetric bending vibration
1056	C-O stretching vibration
706	Mn-O stretching vibration (Mn^{4+} cation)
595	Mn-O bending
528.51	Mn-O bending

Fig.5.10: FTIR spectra of MnO_2

FTIR spectra of Fe–Mn binary oxide are shown in Fig.5.11, according to Fig.5.11 the broad absorption peak in the range of 3200–3650 cm^{-1} is observed. This peak is centered at 3445.9 cm^{-1} corresponds to the stretching vibration of intermolecular hydrogen bond (O–H) existing between the adsorbed water molecules [2–5]. The vibration frequency located at 2361 cm^{-1} indicates the presence of CO_2. This CO_2 somehow incorporated within the structure of Fe–Mn binary oxide nanomatrix [6]. The absorption pick around 1653 cm^{-1}, is due to the asymmetric bending vibration of C=O [13]. Small shoulder vibration peak at 1385 cm^{-1} represents in plane C-H bending mode of vibration. An intense peak at 1067.6cm^{-1} associated with two shoulder peak 1007.8 cm^{-1} and 963 cm^{-1} represented C-O stretching vibration [8, 14, and 15]. Peak value 668.35 cm^{-1} is characteristic for Mn_3O_4 [16]. The bands at 636.53

cm^{-1} represented Mn-O-Mn stretching mode of tetrahedral octahedral sites [17, 18]. The bands located at 590.23 cm^{-1} belong to the metal-oxygen (Mn–O) bending vibration [19]. The main Fe-O stretching was observed at 575.77 cm^{-1} indicating the presence of Fe_3O_4 nanoparticles [20, 21]. The observed vibration bands 562.25 cm^{-1} and small shoulder 462 cm^{-1} assigned to Fe–O–Fe stretching vibration [22, 23].The vibrational frequency located at 418.56 cm^{-1}, can be attributed to the vibration of manganese species (Mn^{3+}– O) in the octahedral site of Mn_3O_4 [24–28].

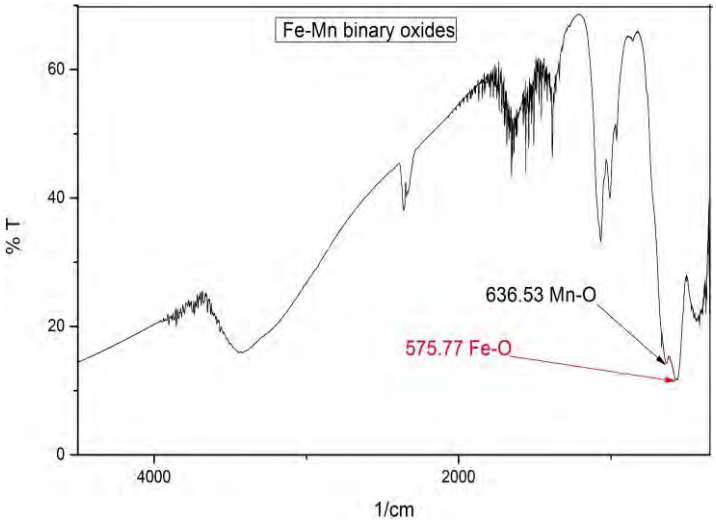

Table 5.7: Relevant FTIR bands of Fe–Mn binary oxide nanoparticles.

Frequency (cm^{-1})	Band Assignments
3445.9	ν_3 (OH) (Coordinated water)
2361	CO_2
1653	C=O asymmetric bending vibration
1385	C-H bending
1067.6	C-O stretching vibration
668.35	Mn-O
636.53	Mn-O-Mn stretching vibration
590.23	Mn-O bending vibration
575.77	Fe-O
562.25	Fe-O-Fe stretching vibration
462	Fe-O-Fe bending vibration
418.56	Mn^{3+}-O vibration in the octahedral site of Mn3O4

Fig.5.11: FTIR spectra of Fe–Mn binary oxides nanoparticles.

A comparative figure of FTIR analysis for Fe_2O_3, MnO_2 and Fe–Mn binary oxides shown in the Fig.5.12.

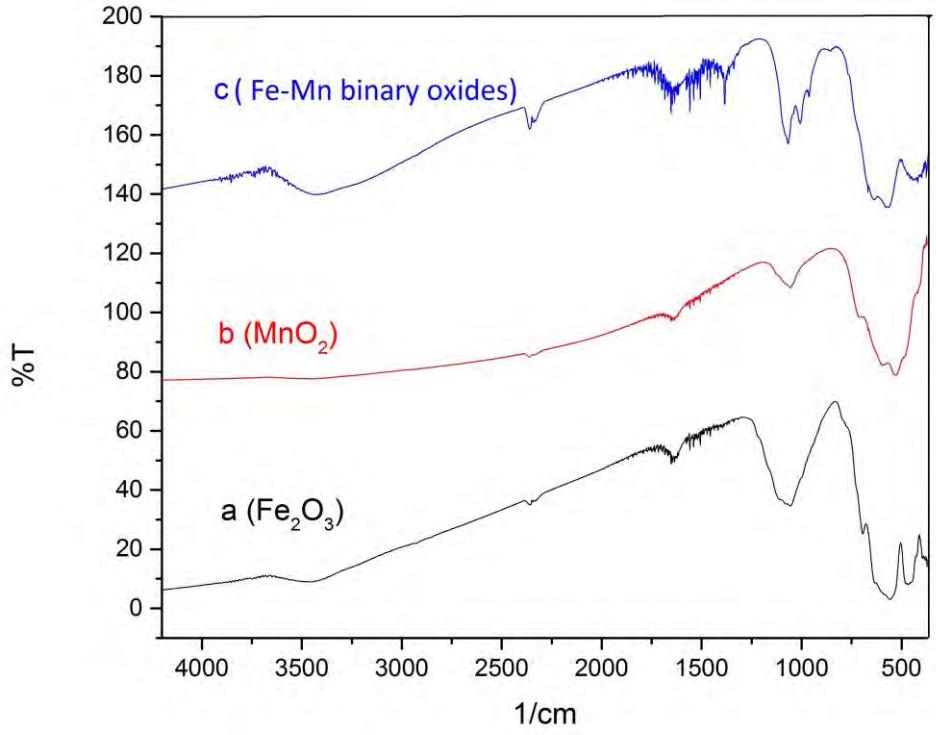

Fig.5.12: A comparative figure of FTIR spectra of (a) Fe_2O_3, (b) MnO_2 and (c) Fe–Mn binary oxides nanoparticles.

5.3.4 Surface morphologies of Fe-oxides, Mn-oxides and Fe-Mn binary oxides nanoparticles

Surface morphologies of Fe_2O_3, MnO_2, Fe–Mn binary oxide nanoparticles obtained using gel formation route were investigated by virtue of FESEM as shown in Fig. 5.13 - Fig. 5.17.

Figure 5.13 showed the FESEM image of α-Fe_2O_3 nanoparticles acquired from gel derived by starch media heat treated at 650˚C for 4 hours. From FESEM it can demonstrate that the obtained nanoparticles have a homogeneous size with an average diameter of ~10 nm.

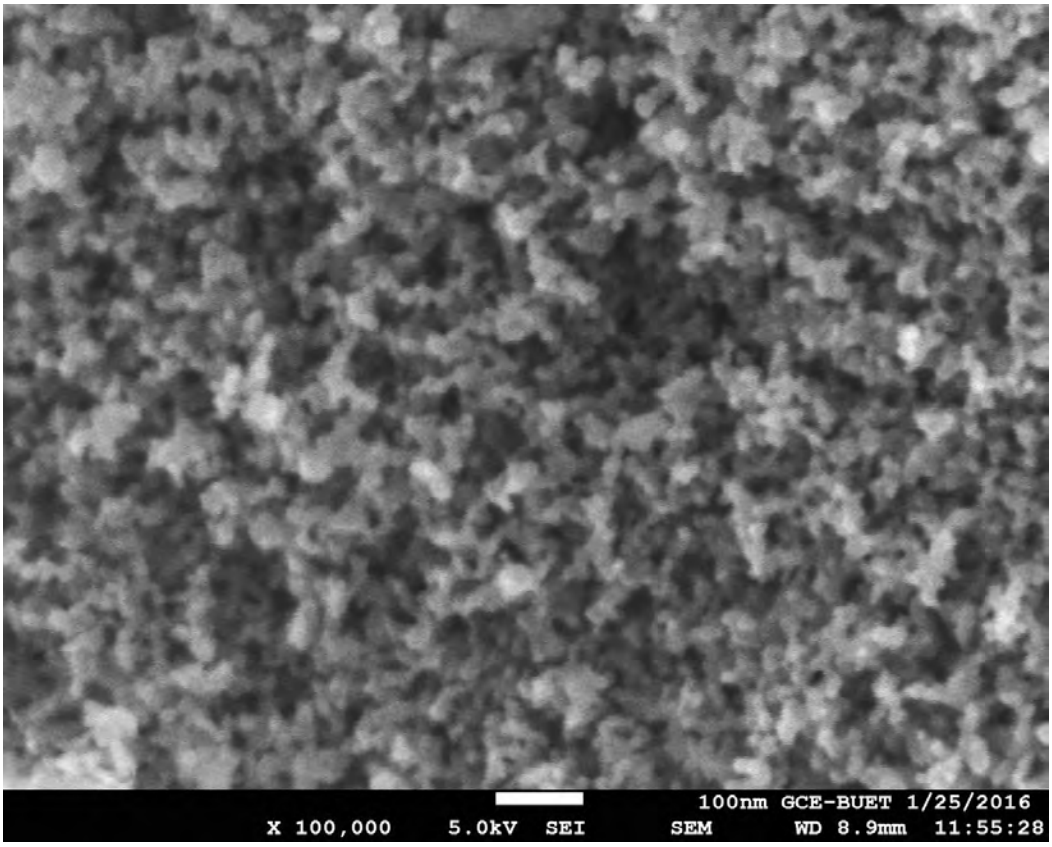

Fig. 5.13: SEM image of as prepared Fe_2O_3 nanoparticles.

From the FESEM image of Fe_2O_3 nanoparticles, it can be seen that the nanoparticles are of nanosphere materials which may enhance the functionality of the materials.

Fig. 5.14 shows the top view of FESEM image of the overall appearance of the combustion derived product MnO_2. It can be seen that the sample consisted of a large amount of cubic and rod like products having different diameter, which maintain the morphology of the product, might be due to the non-uniform distribution of temperature during heat treatment.

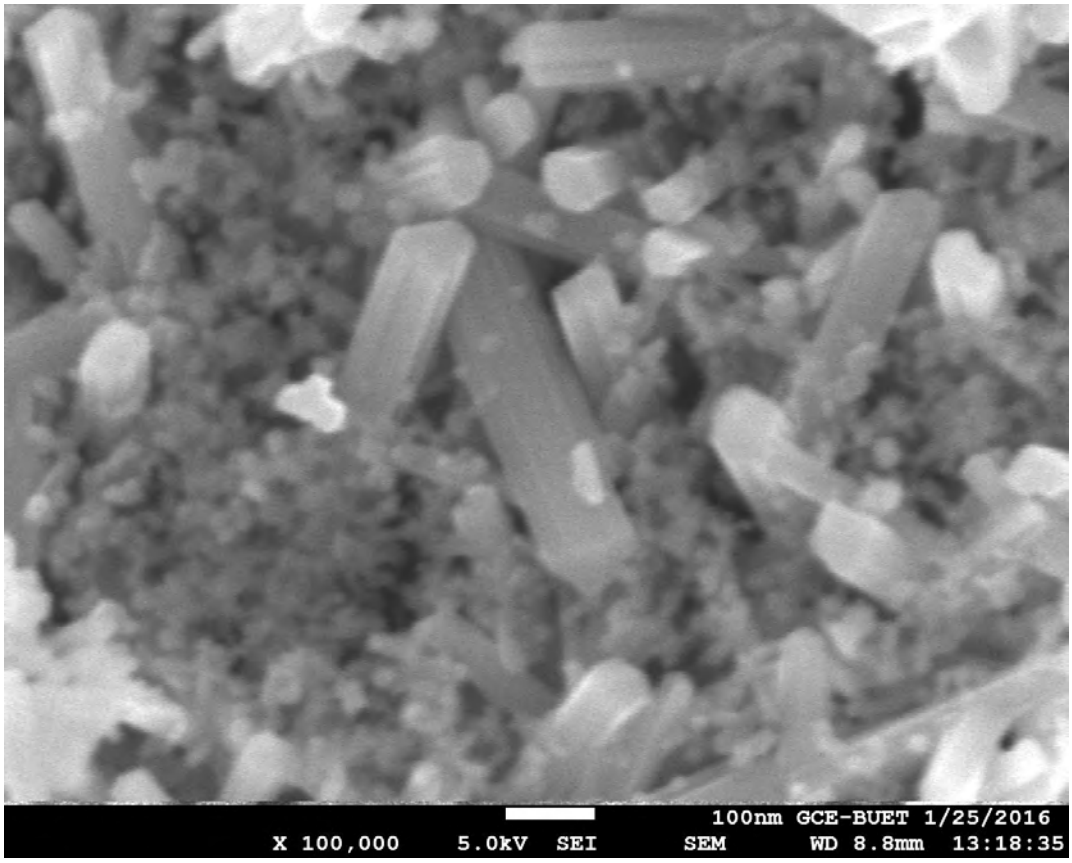

Fig. 5.14: SEM image of MnO_2 nanoparticles.

These rods, about 25-50 nm in diameter, have a lengths about 100-250nm. The surfaces of the rods are almost smooth along their entire length. Cubic forms are about 10-15 nm. in diameter.

A series of Fe-Mn binary oxides were synthesized with a Fe:Mn ratio of 1:2.55, 1:1.28 and 1:0.64. The morphology of the as-prepared Fe-Mn binary oxides were observed by FESEM, as shown in Fig. 5.15, 5.16 and 5.17.

From Fig. 5.15, it can be seen that the particles are uniformly distributed and are mainly composed of small sphere with around 5 nm of average grain size.

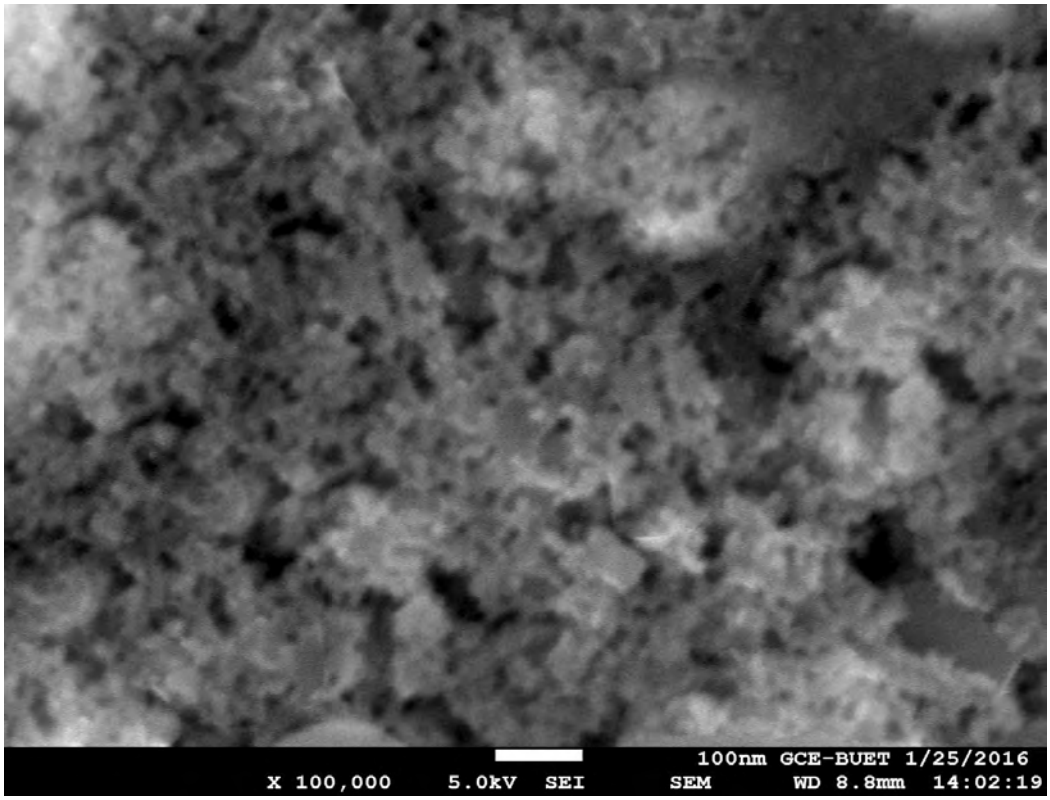

Fig. 5.15: FESEM image of Fe-Mn binary oxides nanoparticles obtained from 1:2.55 Fe-Mn molar ratio.

From Fig. 5.16, it can be seen that the particles are uniformly distributed and the products are mainly composed of cubic-like particles in the range of 23-40 nm. The as prepared sample (1:1.28) seems aggregated having micro porous structure.

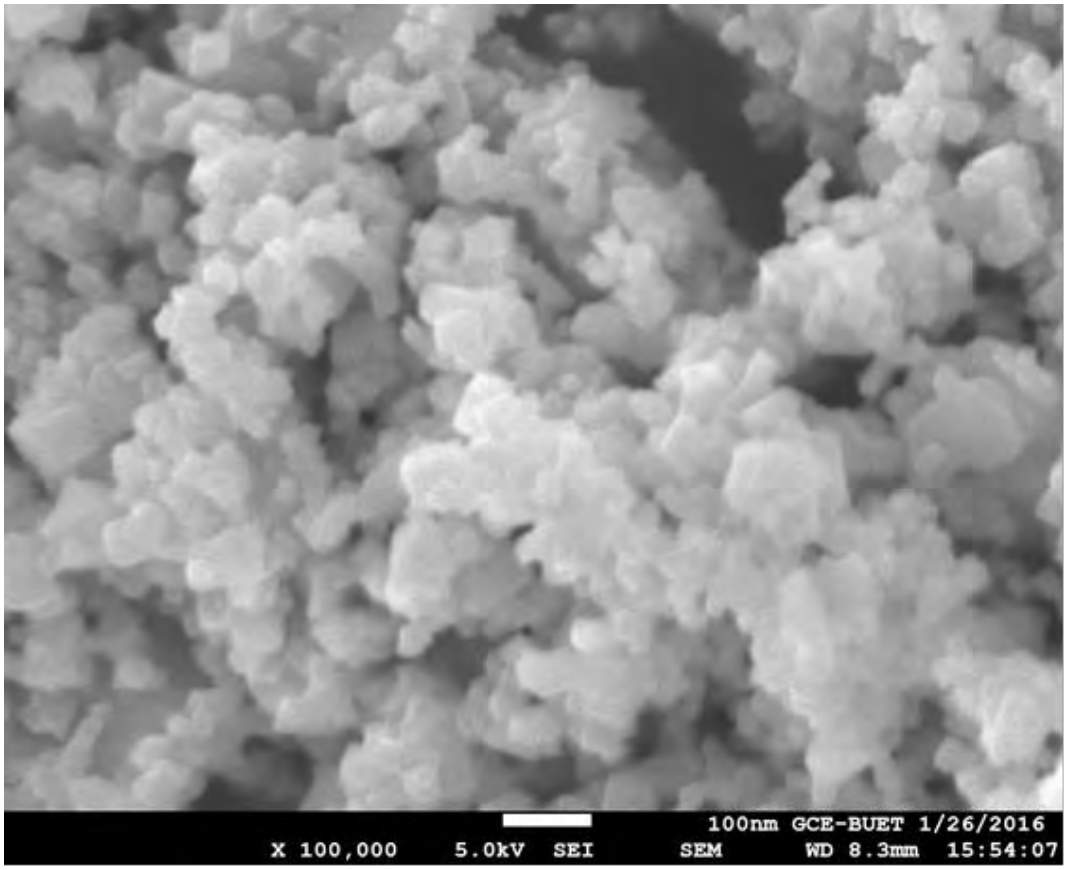

Fig. 5.16: FESEM image of Fe-Mn binary oxides nanoparticles obtained from 1:1.28 Fe-Mn molar ratio.

From Fig. 5.17, it can be seen that the product particles are uniformly distributed and the products are mainly composed of cubic-like particles with 23-40 nm of average grain size.

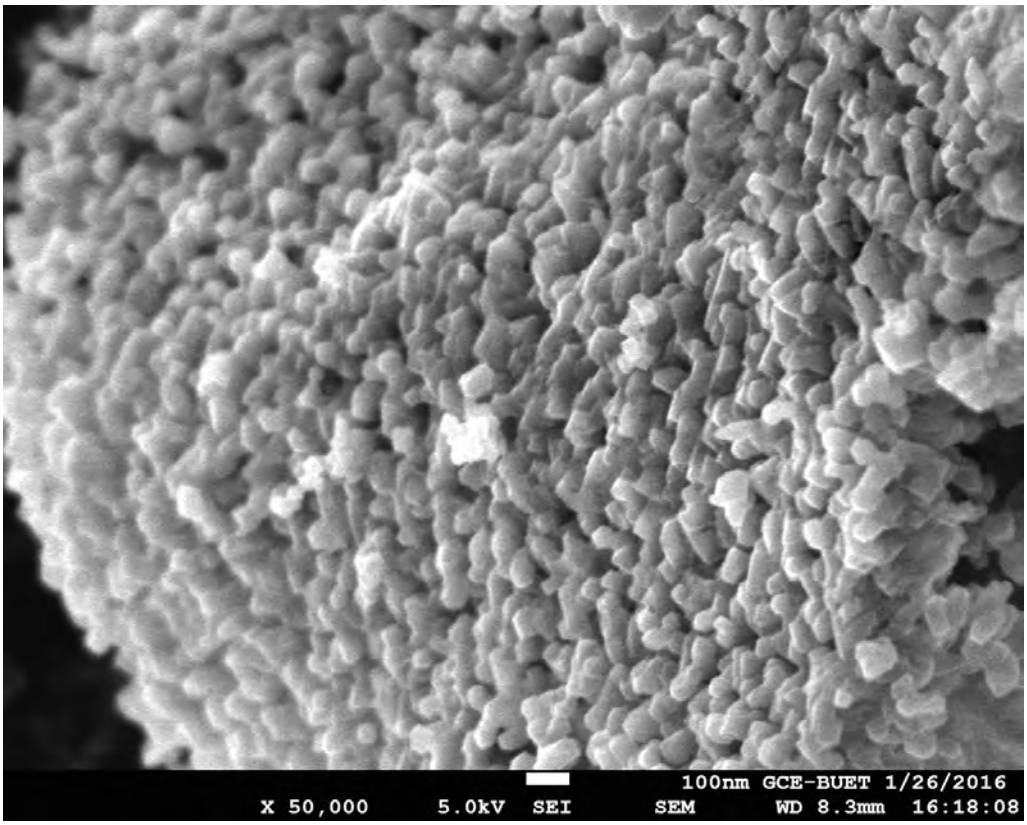

Fig. 5.17: SEM image of Fe-Mn binary oxides nanoparticles obtained from 1:0.64 Fe-Mn molar ratio.

It seems from the image that the material was arranged in highly order looks as like as a wall made of rock.

From the above data, of FESEM it can be concluded that the mixing ratio of Fe: Mn has a profound effect on the shape and size of the so prepared nanoparticles.

5.4 Thermogravimetric analysis (TGA)

The phase formation and decomposition which occurs during heat treatment of precursor compound was confirmed by TGA results. The thermal analysis was carried out from room temperature to 800°C. Thermogravimetric analysis (TGA) of as-prepared compounds were performed by heating in air atmosphere at 10°C/min in alumina crucible. Figure 5.18 shows the thermal analysis (TGA) of precursor compounds obtained from gel process by using starch solution. It is clear that there are three distinct mass loss steps in the figure 5.18(a) for Starch-Fe oxides. Temperature ranges 23.76°C–83.76°C, 229.70°C–295.11°C and 338.08°C-384.53°C, respectively, in TGA curve 5.19(a).In the curve 5.18(a) The first mass loss step was gradually around 23.76°C– 83.76°C. The mass loss was 7.39%, and this loss of mass is ascribed to the removal of surface adsorbed water of precursor (starch-Fe oxides). The second mass loss was at 229.70°C–295.11°C, and the mass loss was 37.47% which is due to the dehydration reaction of –OH groups in starch molecules present in as prepared sample. The third step mass loss was occurring in the range of 338.08°C–384.53°C, and this mass loss was 26.6 %, which might due to the decomposition of starch of the samples releasing CO_2 gas. After 384.53°C the curve illustrates the parallel line with the temperature axis representing high stability of α-Fe_2O_3 nanoparticles. There is no associated signal with these latter thermal events in the TGA curve confirming the crystallization and phase transition events of α-Fe_2O_3 nanoparticles.

Table 5.8: TGA analysis of Starch-Fe_2O_3 nanoparticles.

Temperature range	Mass loss	Explanation
23.76°C–83.76°C	7.39%	Surface absorbed H_2O
229.70°C–295°C	37.47%	Dehydration reaction of –OH groups in starch
338.08°C–384.53°C	26.6%	Decomposition of starch releasing CO_2
384.54°C–800°C	Not remarkable	No farther decomposition or oxidation occurs.

In the curve 5.18(b) for Starch-Fe-Mn binary oxides there are also three distinct mass loss steps as similar to starch-Fe oxides sample. Temperature ranges 31.11°C–105.12°C, 218.61°C–307.19°C and 448.68°C–528.82°C, respectively, in TGA curve 5.19(b). The first mass loss was 6.755%, primarily attributed to the evaporation of surface adsorbed water and the second mass loss was 39.92% might be the result of dehydration reaction of –OH groups in starch molecules present in as prepared sample. The third stage for weight loss started from 448.68°C up to 528.82 °C and it is 25.56% again this weight loss refers to the decomposition of starch of the samples releasing CO_2 gas. After 528.82°C the TGA curve for starch Fe_3O_4 & Mn_3O_4 nanoparticles sample became steady with stable weight percentage up to 800°C which indicates that the remaining of Fe_3O_4 only and it is representing about 6.77% of the sample weight.

It is noticed that the rate of weight loss for Starch-Fe-Mn binary oxide nanoparticles sample is slower than that of Starch-Fe oxides sample. This indicated that the more thermal stability for Starch-Fe-Mn binary oxide nanoparticles sample that may be due

to the coordination bond between iron and starch molecules which is strengthened by the presence of Mn-oxides.

Table 5.9: TGA analysis of Starch-Fe–Mn binary oxides nanoparticles.

Temperature range	Mass loss	Explanation
31.11°C–105.12°C	6.75%	Surface absorbed H_2O
218.61°C–307.19°C	39.92%	Dehydration reaction of –OH groups in starch
448.68°C–528.82°C	25.56%	Decomposition of starch releasing CO_2
528.83°C–800°C	Not remarkable	No farther decomposition or oxidation occurs.

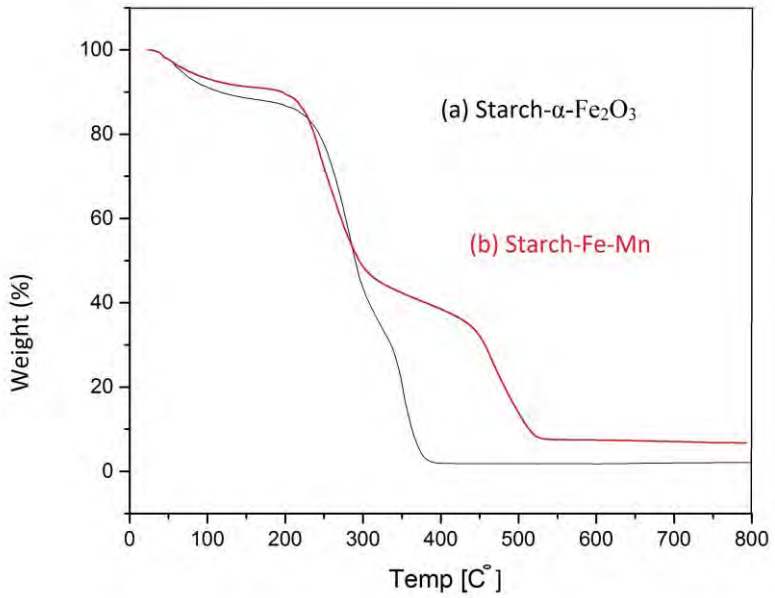

Fig. 5.18: TGA plot of (a) Starch–α-Fe_2O_3 nanoparticles and (b) Starch–Fe–Mn binary oxides.

5.5 Arsenic sorption

5.5.1 Arsenic sorption by iron oxide

To analyse arsenic sorption capacity of iron oxide, iron oxide nanoparticles were added with As(V), As(III) and the solution containing both the arsenic species [As(V) and As(III)]. Then analyzed with the help of atomic adsorption spectroscopy (AAS). The analysis result showed that iron-oxides can effectively remove As(V) which was 5mg/g (sorption capacity) and for As(III) it removal capacity was zero. Again for total arsenic [As(V) and As(III)] removal capacity was 2.5 mg/g. the following graph shows the removal of arsenic by iron–oxide nanoparticles.

Table 5.10: Removal of arsenic by Fe–oxide.

Fe-oxide (Fe_2O_3)			
	As(V)	As(III)	Total arsenic As(III) and As(V)
Sorption capacity	5.00	0.00	2.50
Sorption efficiency	4.00	0.00	2.00

5.5.2 Arsenic sorption by Mn–oxide

Arsenic sorption study was also done by the same process as for the iron oxides. From the atomic adsorption spectroscopy (AAS) it was found that MnO_2 has no sorption capacity for any kind of arsenic species and it was remain zero for both species of arsenic.

5.5.3 Effect of Fe:Mn molar ratio on arsenic sorption

To determine the optimal Fe:Mn molar ratio, a series of Fe–Mn binary oxide adsorbents with different Fe:Mn molar ratios from 1;0.64 to 1:2.55, were synthesized and tested for arsenic sorption. The results are shown in Fig. 5.19(a) As(V) sorption

by the Fe–Mn binary oxide increases through peaks and valleys with an increase in Fe:Mn molar ratio and reaches a maximum of 53.325 mg/g when the ratio is 1:2.55. Then, As(V) sorption decreases significantly when the molar ratio of Fe:Mn is 0:1 that is MnO_2. The As(V) sorption capacity decreases to 0 mg/g at a Fe:Mn molar ratio of 0:1 that is MnO_2. This value is very close to that of pure iron oxide (5mg/g at Fe:Mn molar ratio of 1:0). Theoretically, if no synergy effect occurred between iron oxide and manganese oxide, the As(V) sorption capacity of 1:2.55 Fe–Mn binary oxide should be 5–0 mg/g, which is far less than real value of 53.325 mg/g.

For As(III), similar phenomena were observed shown in Fig. 5.20(a), maximal As(III) sorption occurred at 1:2.55 Fe:Mn molar ratio which is 15.825 mg/g. Again As(III) sorption is 0 mg/g both 1:0 (Fe_2O_3) and 0:1 (MnO_2) Fe:Mn molar ratio.

For Arsenic solution containing both As(III) and As(V) species, similar pattern of peaks and valleys are observed as for As(V) sorption but the values of sorption capacity is different shown in Fig. 5.21(a). Maximal Arsenic sorption occurred at 1:2.55 Fe:Mn molar ratio which is 79.675 mg/g.

Table 5.11: Removal of As(V) by a series of Fe–Mn binary oxides,

Name of the sorbent	Sorption capacity	Sorption efficiency
Fe_2O_3	5.000	4.000
1:0.64 (Fe–Mn binary oxide)	25.000	20.000
1:1.28 (Fe–Mn binary oxide)	12.500	10.000
1:2.55 (Fe–Mn binary oxide)	53.325	42.660
MnO_2 (Fe–Mn binary oxide)	0.000	0.000

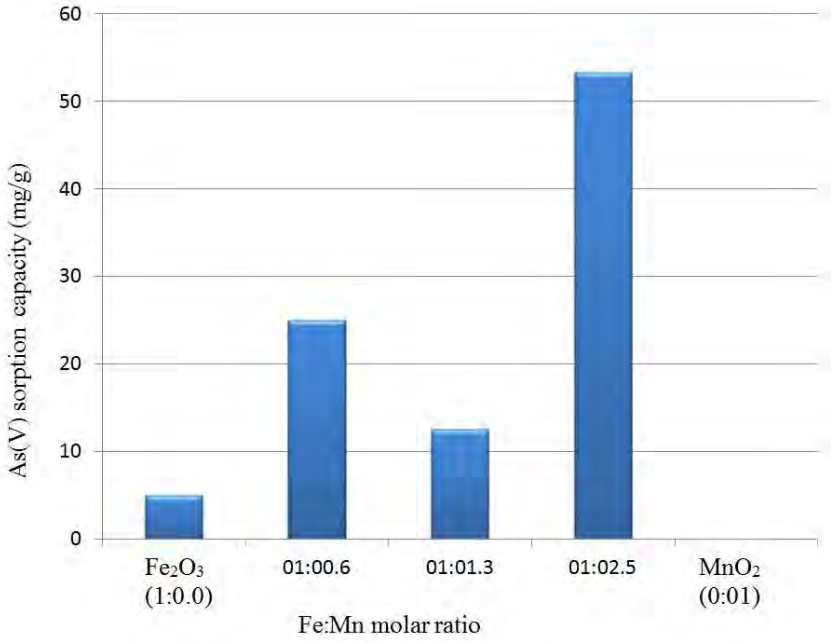

Fig. 5.19: Effect of Fe:Mn molar ratio on As(V) sorption capacity by Fe–Mn binary oxide. Arsenic initial concentration = 50mg/L, Sorbent dose = 400 mg/L, pH = 7.0 ±0.1, T = 25 ±1°C.

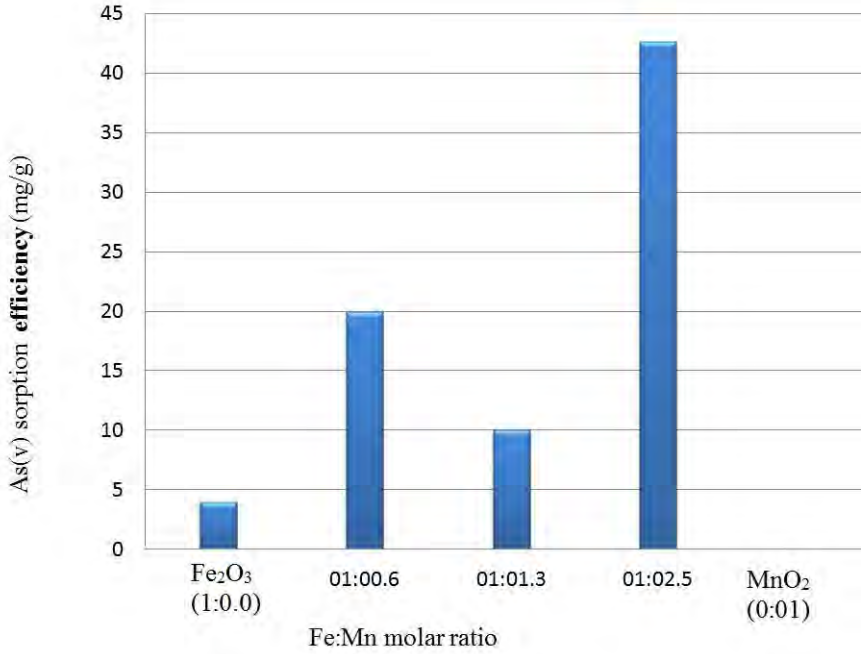

Fig. 5.20: Effect of Fe:Mn molar ratio on As(V) sorption efficiency by Fe–Mn binary oxide. Arsenic initial concentration = 50mg/L, Sorbent dose = 400 mg/L, pH = 7.0 ±0.1, T = 25 ±1°C.

Table 5.12. Removal of As(III) by a series of Fe–Mn binary oxides.

Name of the sorbent	Sorption capacity	sorption efficiency
Fe_2O_3	0.00	0.00
1:0.64 (Fe–Mn binary oxide)	12.50	10.00
1:1.28 (Fe–Mn binary oxide)	7.50	6.00
1:2.55 (Fe–Mn binary oxide)	15.83	12.66
MnO_2 (Fe–Mn binary oxide)	0.00	0.00

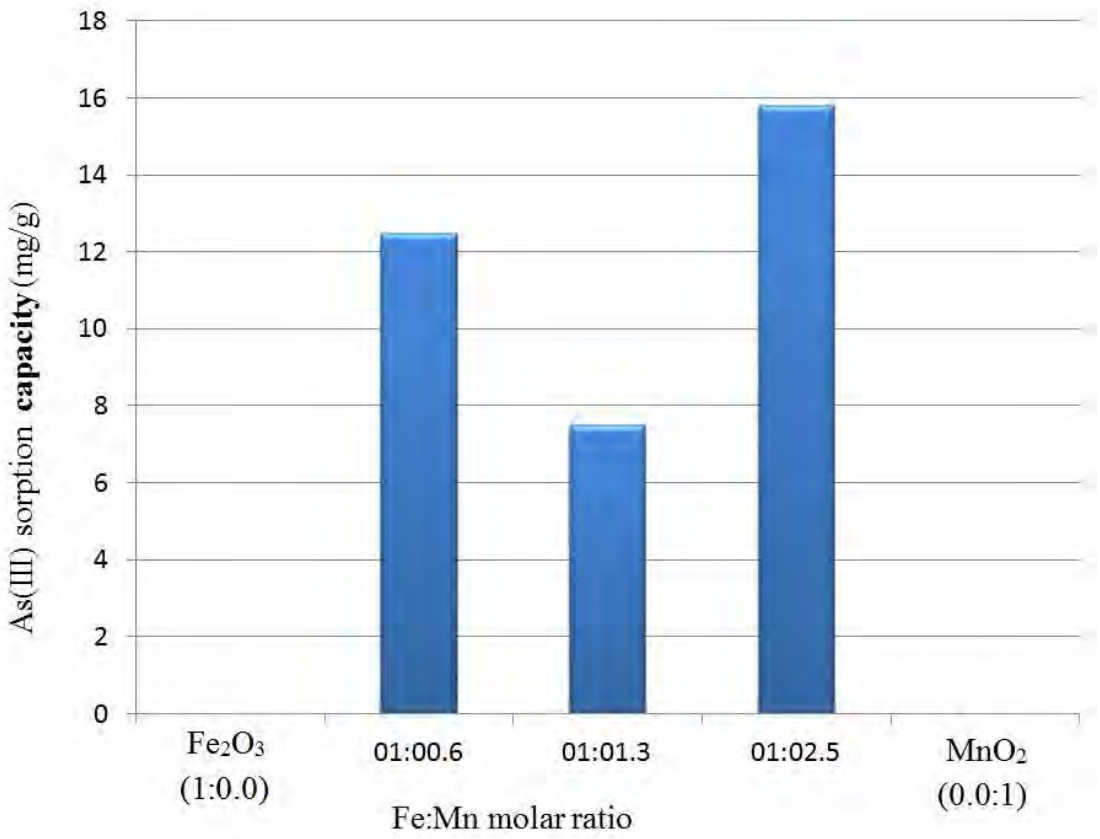

Fig. 5.21: Effect of Fe:Mn molar ratio on As(III) sorption capacity by Fe–Mn binary oxide. Arsenic initial concentration = 50mg/L, Sorbent dose = 400 mg/L, pH = 7.0 ±0.1, T = 25 ±1°C.

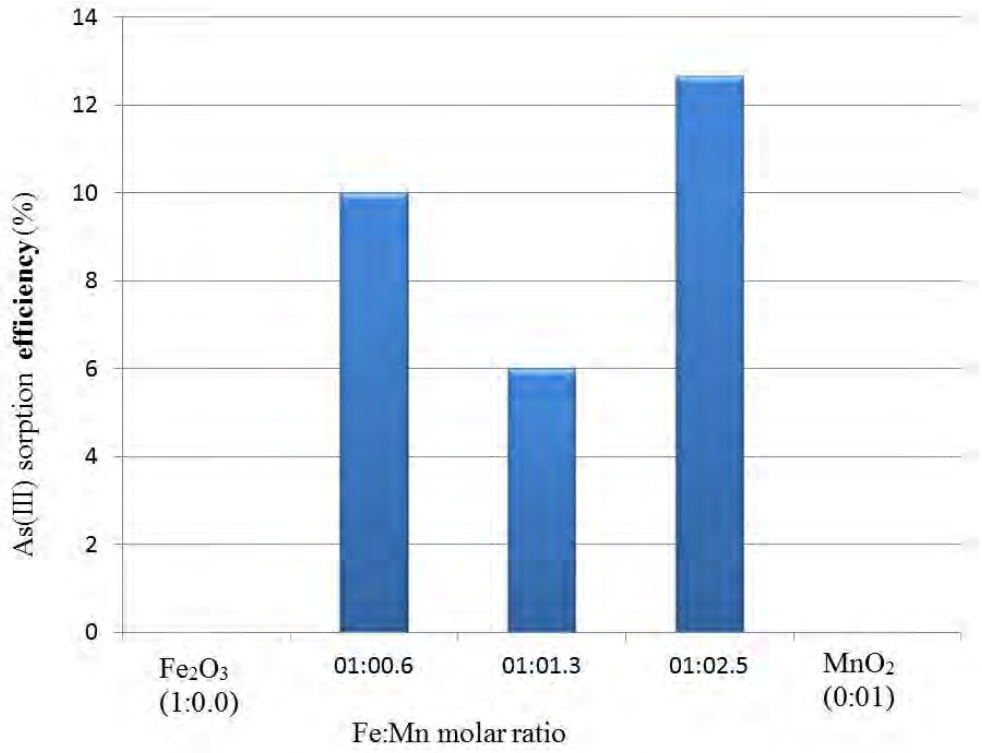

Fig. 5.22: Effect of Fe:Mn molar ratio on As(III) sorption As(III) sorption efficiency by Fe–Mn binary oxide. Arsenic initial concentration = 50mg/L, Sorbent dose = 400 mg/L, pH = 7.0 ±0.1, T = 25 ±1°C.

Table 5.13: Removal of As(III) and As(V) by a series of Fe–Mn binary oxides.

Name of the sorbent	Sorption capacity	sorption efficiency
Fe_2O_3	2.500	2.000
1:0.64 (Fe–Mn binary oxide)	30.000	24.000
1:1.28 (Fe–Mn binary oxide)	17.500	14.000
1:2.55 (Fe–Mn binary oxide)	79.675	63.740
MnO_2 (Fe–Mn binary oxide)	0.000	0.000

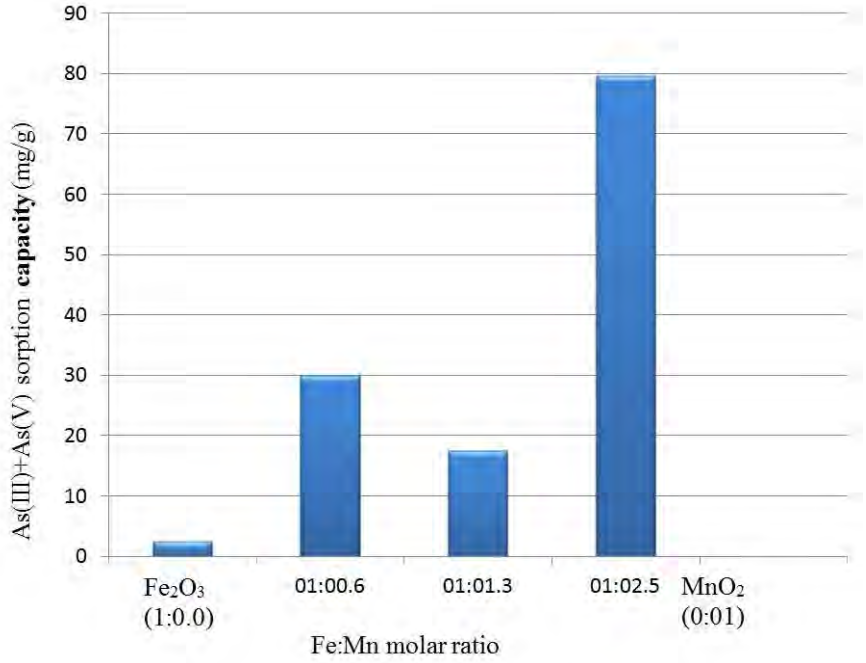

Fig. 5.23: Effect of Fe:Mn molar ratio on arsenic As(III) and As(V) sorption capacity by Fe–Mn binary oxide. Arsenic initial concentration = 50 mg/L, Sorbent dose = 400 mg/L, pH = 7.0 ±0.1, T = 25 ±1°C.

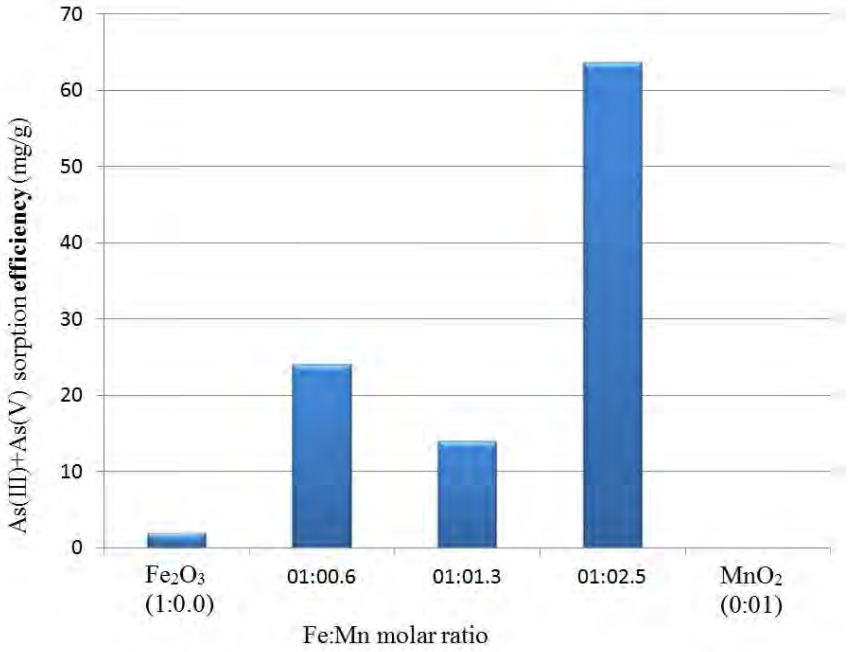

Fig. 5.24: Effect of Fe:Mn molar ratio on arsenic As(III) and As(V) sorption efficiency by Fe–Mn binary oxide. Arsenic initial concentration = 50 mg/L, Sorbent dose = 400 mg/L, pH = 7.0 ±0.1, T = 25 ±1°C.

It is noticed that Mn–oxide cannot sorbed arsenic species but in the presence of Mn-oxide the sorption properties of iron-oxides tremendously increase. Here Mn species oxidizes the As(III) into As(V). The As(V) very much like to sorbed on Fe–oxides as a result Fe–Mn binary oxide has high sorption capacity of arsenic, which is as much higher as 79.675 mg/g at a certain Fe:Mn molar ratio (1:2.55). A comparison has been made between the prepared Fe-Mn binary oxide and previously reported sorbents for arsenic sorption (Table 5.14) the analytical result of comparison shows that the removal capacity is moderately high and to the best of our knowledge it is the second highest among the reported. These results suggest that, combination of manganese oxide with iron oxide results in a significant improvement in arsenic sorption. And the Fe:Mn molar ratio is a key factor influencing the sorption capacity of the Fe–Mn binary oxide.

Table 5.14: Comparison of maximum arsenic sorption capacities for different sorbents

Sorbent	As con. range (mg/L)	Max. As(III) & As(V) adsorption capacity (mg/g)	Ref.
CuO nanoparticles	0–100	49.5 (pH 8.0)	Martinson and Reddy, 2009, [29]
Doughnut-like CuO	0–90	4.7 (4.0)	Cao et al., 2007, [30]
$Al_2O_3/Fe(OH)_3$	7.5–135 mmol	45.7 (pH 6.6)	Hlavay and Polya´ k, 2005, [31]
Fe–Mn binary oxide	0–40	120.9(pH6.9)	Zhang et al. 2007, [32]
Fe–Mn binary oxide	50	79.68(pH 7.0)	Present study

5.5.4 Arsenic sorption mechanism

From the AAS analysis, it was notice that total As removal capacity of Fe_2O_3 was very low. But in the presence of Mn–oxides the removal capacity of Fe-Mn mixed binary oxide was moderately high. From this observation it can be conclude that

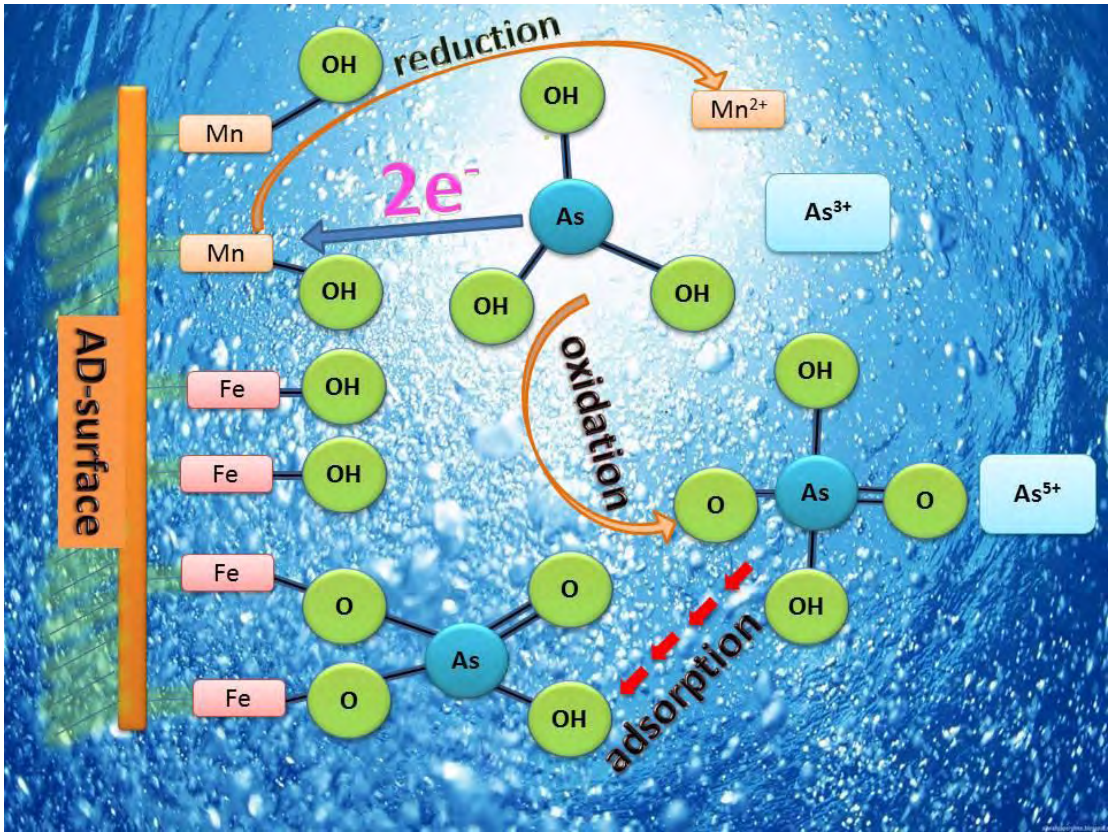

Fig.5.25. Proposed As removal mechanism from aqueous solution by using Fe–Mn binary oxides.

Mn–oxides can oxides As(III) to As(V) but cannot adsorbed any kind of As species [As(III) and As(V)]. Thus from the above observation the following As removal mechanism from aqueous solution by the prepared Fe-Mn binary oxide can be proposed. The As removal mechanism from aqueous solution shown in the Fig.5.22. The above mechanism supported by the work of G. S. Zhang et al. [33].

5.6 Conclusion

A starch assisted gel formation method has been develop for the preparation of iron oxide, manganese oxide and iron-manganese binary oxide in nanodimension as an effective sorbent for the removal of total arsenic [As(III) and As(V)] from ground water by starch assisted gel formation route. From the experimental observation it can be concluded as:

1. The synthesized iron oxide is α─Fe_2O_3 with an average particle diameter of 10 nm according to FESEM image. The crystals are found as Rhombohedral with uniform sphere having the particle diameter of 21 nm from XRD analysis. From the arsenic removal experiments it was found that it has the good removal capacity of As (V) but not promising in removal of As(III).

2. The prepared manganese oxide by the reaction of $KMnO_4$ and starch were found to be MnO_2 with Body-centered tetragonal crystal geometry. The morphology of the oxides is found to be mixed of rod and cube with a diameter in the range of 10-50 nm. From the arsenic removal experiments it was found that it is a good oxidant for the oxidation of As (III) to As (V) but incapable of removal.

3. The Fe-Mn ratio in the binary oxides have a profound effect in size, shape, crystallites and removal capacity of total arsenic (As(III) and As(V)). when the mixing ratio was 1:2.55, spherical particles with diameter of 6-10nm were obtained. A ordered structure with a diameter of 30-50 nm obtained when the mixing ratio was 1:0.64 (Fe:Mn). The surface of the ordered structure looks as like as a wall made of rock. The maximum total arsenic removal capacity was found to be around 79 mg/g in case of Fe-Mn binary oxide with mixing ratio of 1:2.55. The highest removal capacity of the matrix can be explained from the smallest size of the particles among the prepared binary oxides. The analytical result of comparison shows that the removal capacity is moderately high and to the best of our knowledge it is the second highest among the reported. The simultaneous removal capacity of As(III) and As (V) can be explained from the oxidation by Mn-oxide and sorption by Fe-oxide.

Due to its excellent arsenic removal performance, simple and low-cost synthesis process the Fe–Mn binary oxide could be a promising sorbent for As(III) and As(V) removal from aqueous solution.

References

1) Visinescu, D., Tirsoaga, A., Patrinoiu, G., Tudose, M., Paraschiv, C., Ianculescud, A., and Carp, O., "Green synthetic strategies of oxide materials: Polysaccharides-assisted synthesis," *Rev. Roum. Chim.,* Vol. 55, pp. 1017–1026 (2010).

2) Samira, B., Chandrappa, K., and Sharifah, B., "Generation of Hematite Nanoparticles via Sol-Gel Method," *J. Chem. Sci.,* Vol. 3, pp. 62−68 (2013).

3) Ndifon, P. T., Agwara, M. O., Paboudam, A. G., Yufanyi, J., Ngoune, Galindo, A., Álvarez, E., and Mohamadou, A., "Synthesis, characterization and crystal structure of a cobalt(II)-hexamethylenetetramine coordination polymer," *Transition Met. Chem.,* Vol. 34, pp. 745-750 (2009).

4) Ng, C. H., Teoh, S. G., Moris, N., and Yap, S. Y., "Structural, infrared spectral and thermogravimetric analysis of a hydrogen-bonded assembly of cobalt(II) and nickel(II) mixed complex cations with hexamethylenetetr-amine and aqua ligands: $\{[M(hmt)_2(H_2O)_4][M(H_2O)_6]\}(SO_4)_2 \cdot 6H_2O$," *J. Coord. Chem.,* Vol. 57, pp. 1037-1046 (2004).

5) Jensen, J. O., "Vibrational frequencies and structural determinations of hexamethylenetetramine, Spectrochimica Acta Part A," *Mol. Bio. Spec.,* Vol. 58, pp. 1347-1364 (2002).

6) Ling, W., Ming, Z., and Simon, A., "Infrared study of CO_2 incorporation into pyrophyllite $[Al_2Si_4O_{10}(OH)_2]$ during dehydroxylation," *Clays Clay Miner.,* Vol. 51, pp. 439–444 (2003).

7) Coronado, E., Galán-Mascarós, J. R., and Martí-Gastaldo, C., "Design of bimetallic magnetic chains based on oxalate complexes: towards single chain magnets," *Cryst. Eng. Comm.,* Vol. 11, pp. 143-2153 (2009).

8) Mohamed, G. F., Safaa, M. S. S., Hussein, A. M. S., and Kamil, M. M., "Application of FT-IR Spectroscopy for Rapid and Simultaneous Quality Determination of Some," *Nat. Sci.,* Vol. 9, pp. 11 (2011).

9) Zhao, B., Wang, Y., Guo, H., Wang, J., He, Y., Jiao, Z., and Wu M., "Iron oxide(III) nanoparticles fabricated by electron beam irradiation method," *Mater. Sci. Poland.,* Vol. 25, pp. 1143-1148 (2007).

10) Sarbas, B., and Topper, W.,(1991) *Gmelin handbook of inorganic & organometallic chemistry.* Springer-Verlag Berlin Heidelberg GmbH., USA.

11) Gillot, B., Guendouzi, M. E., Laarj, M., "Particle size effects on the oxidation–reduction behavior of Mn_3O_4 hausmannite," *Mater. Chem. Phys.,* Vol. 70, pp. 54–60 (2001).

12) Zhang, Y. C., Qiao, T., Hu, X. Y., & Zhou, W. D., "Simple hydrothermal preparation of γ-MnOOH nanowires and their low-temperature thermal conversion to β-MnO_2 nanowires," *J. Cryst. Growth.,* Vol. 280 pp. 652-657 (2005).

13) Naohiro, K., Kazuhisa, H., and Yoshinobu, N., "A novel synthesis of chiral rotaxanes via covalent bond formation," *Chem. Commun.,* Vol. 4 pp. 466-467 (2004).

14) Joseph, Hornback, M., (2005) *Organic Chemistry.* Cengage Learning, USA.

15) Jolanta, K., Małgorzata, C., Zbigniew, K., Anna, B., Krzysztof, B., Jorg, T., and Piotr, S., "Application of Spectroscopic Methods for Structural Analysis of Chitin and Chitosan," *Mar Drugs.,* Vol. 8, pp. 1567–1636 (2010).

16) Lee, W. E., Gadow, R., (2016) *Proceedings of the III Advanced Ceramics and Applications Conference.* Atlantis press, USA.

17) Jing, X., Ya-Qing, D., Xiao-Man, X., Yan, L., Pengfei, T., and Yi-Fan, H., "Preparation, Characterization, and Kinetic study of a core-shell Mn_3O_4@SiO_2 Nanostructure Catalyst for CO oxidation," *ACS Catal.,* Vol. 11, pp. 4106-4115 (2014).

18) Mira, R., Svetozar, M., Stanko, P., Dur-dica, D., Marijan, M., Mile, I., "Synthesis and long-term phase stability of Mn_3O_4 nanoparticles," *J. Mol. Struct.,* Vol. 1044, pp. 255–261, (2013).

19) Wang, H. E., Qian, D., "Synthesis and electrochemical properties of α-MnO_2 microspheres." *Mater. Chem. Phys.,* Vol. 109, pp. 399–403, (2008).

20) Ruipeng, F., Ronggjiang, H., Kezheng,C.,"Preparation and characterization of γ-Fe_2O_3/ZnO composite particles," *Mater. Lett.,* Vol. 62, 4066-4068 (2008).

21) Kyungsun, S., Sujeong, L., Chang-Yul, S., Wonbaek, K., Kyung-Seok, K., and Dongbok, S., "Synthesis and Characterization of Iron Oxide Nanoparticles Prepared by Electrical Explosion of Fe Wire in Ar-O_2 Gas Mixtures," *Mater. Trans.,* Vol. 53, pp. 2056-2059, (2012).

22) Takanari, T., Takashi, N., Shunsuke, A., Koichi, S., Seiichi, T., and Tadafumi, A., "Surfactant Assisted One-pot Synthesis of Superparamagnetic Magnetite Nanoparticle Clusters with a Tunable Cluster Size and Sensitivity for Magnetic Field." *Dalton Trans.,* Vol. 40, pp. 1073-1078, (2011).

23) Rahman, M. M., (2011) *Nanotechnology and Nanomaterials.* Tech., Croatia – European Union.

24) Ishii, Nakahira, and Yamanaka, "Infrared absorption spectra and cation distributions in $(Mn,Fe)_3O_4$," *Solid State Commun.,* Vol. 11, pp. 209–212, 1972.

25) Wang, W. Z., Xu, C. K., Wang, G. H., Liu, Y. K., and Zheng, C. L., "Preparation of smooth single-crystal Mn_3O_4 nanowires," *Adv. Mater.,* Vol. 14, pp. 837–840, (2002).

26) Gupta, N., Verma, A., Kashyap, S. C., and Dube, D. C., "Microstructural, Dielectric and magnetic behavior of spindeposited nanocrystalline nickel-zinc ferrite thin films for microwave applications." *J. Magn. Magn. Mater.* Vol. 308, pp. 137–142, (2007).

27) Lanfredi, S., Saia, P. S., Lebullenger, R., and Hernandes, A. C., "Electric conductivity and relaxation in fluoride, fluorophosphate and phosphate glasses: analysis by impedance spectroscopy," *Solid State Ionics*., Vol. 146, pp. 329–339, (2002).

28) Julien, C. M., Massot, M., Poinsignon, C., "Lattice vibrations of manganese oxides - part 1. Periodic structures," *Spectrochim. Acta,* Vol. 60, pp. 689–700, (2004).

29) Martinson, C.A., and Reddy, K.J., "Adsorption of arsenic(III) and arsenic(V) by cupric oxide nanoparticles," *J. Colloid Interface Sci.,* Vol. 336, pp. 406–411, (2009).

30) Cao, A.M., Monnell, J.D., Matranga, C., Wu, J.M., Cao, L.L., and Gao, D., "Hierachical nanostructured copper oxide and its application in arsenic removal," *J. Phys. Chem. C*, Vol. 111, pp. 18624–18628, (2007).

31) Hlavay, J., Polya´ k, K., "Determination of surface properties of iron hydroxide-coated alumina adsorbent prepared for removal of arsenic from drinking water." *J. Colloid Interface Sci.,* Vol. 284, pp. 71–77, (2005).

32) Zhang, G.S., Qu, J.H., Liu, H.J., Liu, R.P., Li, G.T., 2007b. Removal mechanism of As(III) by a Novel Fe-Mn binary oxide adsorbent: oxidation and sorption. *Environ. Sci. Technol.,* 41, 4613e4619.

33) Zhang, G. S., Huiqu, J., Liu, H. J., Liu, R. P., and Li, G. T., "Removal Mechanism of As(III) by a Novel Fe-Mn Binary Oxide Adsorbent: Oxidation and Sorption" *Environ. Sci. Technol.* Vol. 41, pp. 4613–4619, (2007).